Chromatic Aberrations in Optical Systems: Prediction and Correction

by Mehdi Bahrami

Supervisor: Dr. Alexander V. Goncharov

A thesis submitted in partial fulfilment of the requirements for the degree of Doctor of Philosophy,

School of Physics, Science Faculty,
National University of Ireland, Galway

December 2012

Abstract

The variation of refractive index with wavelength, known as dispersion, was what redirected Isaac Newton from refractive telescope designs toward a reflective one, since he found the chromatic effect incurable. Later it was shown that different materials demonstrate different chromatic characteristics and refractive optical elements can compensate each other's chromatic contributions. This promoted the simple dispersion effect to the field of formulizing and categorizing chromatic aberrations and their corrections. In this study an introduction to this process is provided, where the historical aspects are followed by the mathematical derivation and description of different kinds of chromatic aberrations accompanied with a variety of approaches to correct the chromatic effects in different levels. The provided mathematical basis is employed in studying three distinctive topics. In the first one the flexibility of refractive elements is used to provide a middle-sized catadioptric telescope design with all-spherical surfaces. Employing a new combination of chromatic lens correctors, the image quality can be improved so that it becomes comparable to an equivalent aspheric Ritchey-Chrétien telescope design. As the second topic the atmospheric dispersion and its effect in extremely large telescopes are discussed, where a new atmospheric dispersion corrector design is proposed. In the third task the chromatic behavior in an inhomogeneous medium is considered. A new gradient refractive index lens model for the crystalline lens of the eye is established and a different approach in characterizing its chromatic effects is developed. These three research topics are underpinning the main goal of the theses, that is the role of chromatic aberration in image formation in various optical systems.

List of publications

Paper I: Mehdi Bahrami and Alexander V. Goncharov:
All-spherical catadioptric telescope design for wide-field imaging
Applied Optics, Vol. 49, Issue 30, pp. 5705-5712
(2010)

Paper II: Mehdi Bahrami and Alexander V. Goncharov:
The achromatic design of an atmospheric dispersion corrector for extremely large telescopes
Optics Express, Vol. 19, Issue 18, pp. 17099-17113
(2011)

Paper III: Mehdi Bahrami and Alexander V. Goncharov:
Geometry-invariant gradient refractive index lens: analytical ray tracing
Journal of Biomedical Optics, Vol. 17, Issue 5, pp. 55001-55009
(2012)

Paper IV: Mehdi Bahrami and Alexander V. Goncharov:
Geometry-invariant GRIN lens: iso-dispersive contours
Biomedical Optics Express, Vol. 3, Issue 7, pp. 1684-1700
(2012)

Acknowledgements

This research was supported by Science Foundation Ireland under grant number 07/IN.1/1906.

I express my sincerest gratitude to my supervisor, Dr. Alexander Goncharov, who has supported me throughout my research with his kindness, patience and knowledge whilst allowing me the freedom to work in my own way.

I would like to thank Prof. Chris Dainty for providing a marvelous atmosphere and environment in the Applied Optics Group and for his valuable comments and advices.

The greatest appreciations to Dr. Hamid Fallah, who I am indebted to forever, who was the most help in the worst days.

Thanks to my best friends Meisam, Javad, Hamed, Vahid, Maysam, Hossein, Reza, Vahid, and Marwan.

Most of all, thanks to my parents, my brother, my sister, and my supportive wife for everything they have done for me. I will not forget all the love and the support that you have given me throughout my life and education. Thank you all.

Acronyms

ADC	Atmospheric Dispersion Corrector
AO	Adaptive Optics
ELT	Extremely Large Telescope
E-ELT	The European Extremely Large Telescope
GIGL	Geometry-Invariant Gradient Refractive Index Lens
GMT	Giant Magellan Telescope
GRIN	Gradient Refractive Index
LADC	Linear Atmospheric Dispersion Corrector
LGS	Laser Guide Star
OPD	Optical Path Difference
OPL	Optical Path Length
OT	Optical Transmittance
OT*	Normalized Optical Transmittance
RADC	Rotating Atmospheric Dispersion Corrector
RC	Ritchey-Chrétien
TMT	Thirty Meter Telescope

Contents

Chromatic Aberrations

1.1 Historical aspects

The refractive index of any medium (other than vacuum) varies with wavelength. This means that all the optical properties of a medium are functions of wavelength. Traditionally, chromatic variations of paraxial properties such as image position and magnification have been considered as chromatic aberrations as well as variations of classical aberrations. These chromatic effects are usually the main problem in refractive systems. A well corrected refractive monochromatic imaging system could easily lose its acceptable optical performance even in a small range of wavelengths. Isaac Newton considered this problem intrinsically intractable and turned to reflective systems. In fact, he thought that the chromatic aberrations of all lenses were proportional to their powers, with the same constant of proportionality even for different glasses. Newton was the first to discuss chromatic aberrations in detail in his book, *OPTICKS* [1], which was released to the public in 1704.

Newton's conclusion was not the final word on this topic. Before Newton, it was a common belief that the human eye, because of containing different refractive media, is optically corrected for chromatic aberration. James Gregory, the designer of the Gregorian telescope, had the same opinion in the 1660s. In addition to this, Christian Huygens had shown, in correspondence with Sir Christopher Wren in the 1660s, that a positive and a negative lens more or less in contact could correct spherical aberration [2]. In 1729 Chester Moore Hall, a lawyer, followed on these two and could find a combination of positive and negative lenses made from different glasses, which provided achromatic correction. He had such objectives made by opticians, and proved Newton wrong. In 1858 John Dollond, who expanded Hall's work by experimenting with prisms, patented an achromatic lens [3].

From a technical point of view, manufacturing an acceptable reflective surface is much harder than a refractive element. The first practical reflective telescope was

built by Newton in 1668, 58 years after manufacturing the Galilean telescope (Although Zucchi made his reflective telescope in 1616, its image quality was not comparable to the refractive ones [4].) As manufactures approached 1 m objective doublets, in addition to being limited by mechanical difficulties of building large lenses, they faced another limitation related to difference in dispersion of the glasses used. In fact by, making larger and larger telescope doublet objectives they found that an *achromatic* doublet was not quite free of chromatic aberration, and a residual error, known as *secondary spectrum* appeared. This led to the re-introduction of reflective objectives which are now universally used for apertures exceeding 1 m.

From an optical designer's point of view, the natural reaction to this new problem is adding one more lens to the doublet, thus making it an *Apochromatic triplet*. Implementing this solution was not simple because of the complexity of physics laws in dispersion and the number of constraints which should be satisfied. On the other hand, the variety of glass combinations which can remove the residual chromatic aberrations is limited and sometimes expensive. Nevertheless this solution is implemented nowadays, and achromatic and apochromatic elements are used widely in optical systems (e.g. small size telescope objectives, telescope correctors, photographic lenses, etc.).

Before finishing this brief historical review, it is worth mentioning that a chromaticly aberrated optical system or element is sometimes desired. For instance, when we need to compensate the chromatic aberration arising from the prior optical elements or media, for example the Earth's atmosphere or human eye.

1.2 Axial color and achromats

In the design and analysis of visual systems, it is common to choose F (blue, $\lambda = 486$ nm), d (yellow, $\lambda = 588$ nm), and C (red, $\lambda = 656$ nm) spectral lines for the calculations. Fig. 1.1 shows that in a positive singlet, focus for F light is inside the paraxial focus for d light, while the C one lies on the outside. In fact, primary axial color is defined as the distance between the foci for F and C. To formulize this as a function of lens parameters one can start from a thin lens power equation [5],

$$\phi = (n-1)(C_1 - C_2), \tag{1.1}$$

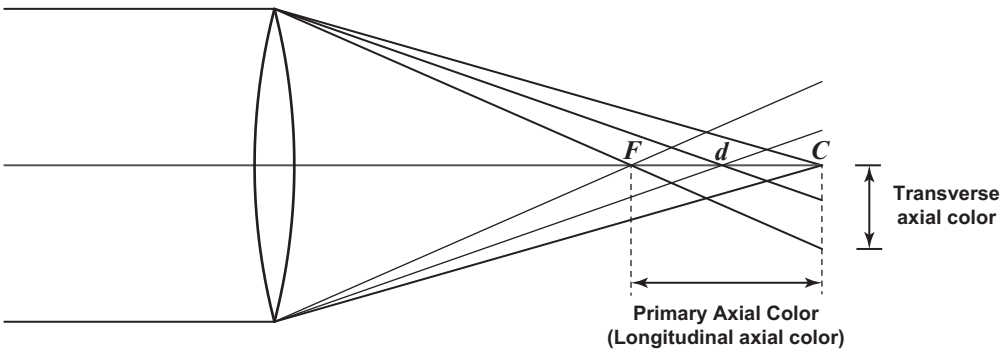

Figure 1.1: F (blue), d (yellow), and C (red) spectral lines and their different foci. Primary axial color is the distance between the foci for F and C.

where n is the refractive index of the lens, and C_1 and C_2 are the curvature of its surfaces. The change in power could be achieved by taking the derivative of Eq. 1.1,

$$d\phi = (C_1 - C_2)dn. \tag{1.2}$$

If we let $dn = n_F - n_C$ in Eq. 1.2,

$$d\phi = (C_1 - C_2)(n_F - n_C), \tag{1.3}$$

by multiplying Eq. 1.3 by $(n_d - 1)/(n_d - 1)$ and rearranging it, we get:

$$d\phi = [(C_1 - C_2)(n_d - 1)] \left(\frac{n_F - n_C}{n_d - 1} \right). \tag{1.4}$$

In optics the term $(n_d - 1)/(n_F - n_C)$ is defined as Abbe V_d number. Eq. 1.4 means that the power difference is equal to the power in d-light divided by the Abbe number,

$$d\phi = (\phi_F - \phi_C) = \frac{\phi_d}{V_d}. \tag{1.5}$$

The smaller Abbe number or the focal length ($f = 1/\phi$), the more axial color we get in the system. This is the reason why first refractors had such objectives with very long focal length $D/f = 50...100$, where D is a telescope objective diameter.

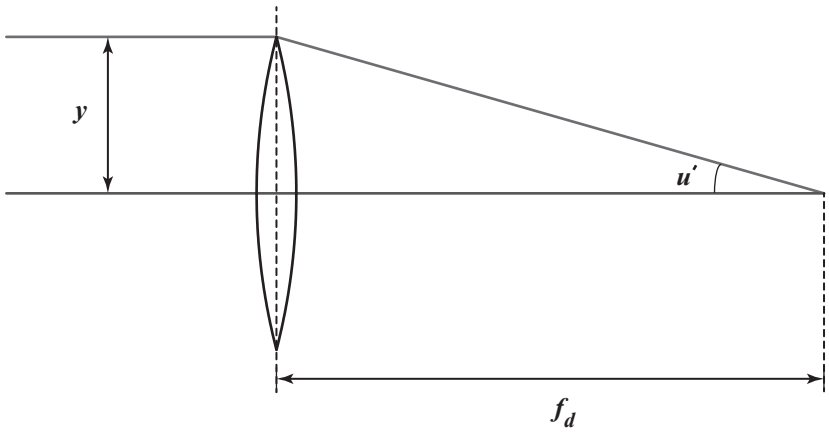

Figure 1.2: Ray-tracing of the marginal ray (the focal length f_d and the angle u' of the ray at the image plane are shown).

1.2.1 Axial chromatic aberration coefficients

One can rewrite Eq. 1.5 in terms of focal length ($\phi_d = 1/f_d$),

$$df = -\frac{f_d}{V_d}. \tag{1.6}$$

As mentioned above, df is the primary axial color. In optical design this difference in focal lengths is known as **longitudinal axial chromatic aberration**, δ_{AX},

$$\delta_{AX} = df = -\frac{f_d}{V_d}. \tag{1.7}$$

By multiplying the left side of Eq. 1.6 by $f_d y^2 / f_d y^2$,

$$df = \left(\frac{f_d^2}{y^2}\right)\left(-\frac{y^2}{f_d V_d}\right), \tag{1.8}$$

where, as Fig. 1.2 shows, y is the height of the marginal ray. On the other hand, (f_d/y) is the angle of the incident ray at the image plane, u', and

$$df = \left(\frac{1}{u'}\right)^2 C_L, \tag{1.9}$$

where C_L, **Seidel axial color coefficient**, is defined by

$$C_L = -\frac{y^2}{f_d V_d}. \tag{1.10}$$

As Fig. 1.1 indicates, axial chromatic aberration could be described in terms of the vertical expansion of the spot too. By the help of Fig. 1.1 and Fig. 1.2, and assuming $f_d \gg \delta_{AX}$, **transverse axial chromatic aberration**, δ_{TAX}, could be defined as

$$\delta_{TAX} = \frac{y\,\delta_{AX}}{2f_d}, \tag{1.11}$$

then by substituting Eq. 1.8 in Eq. 1.11

$$\delta_{TAX} = \frac{y}{2V_d}. \tag{1.12}$$

In some cases describing the chromatic aberration as coefficients connected to optical path difference (OPD) and wavefront is useful. The OPD in the sags of two spherical wavefronts, W, at the exit pupil is a function of the difference in their foci, δ, and the f-number of the system [6],

$$W = -\frac{\delta}{8(f/\#)^2}. \tag{1.13}$$

Then, since it is shown in Eq. 1.9 that

$$\delta_{AX} = \left(\frac{1}{u'}\right)^2 C_L, \tag{1.14}$$

Equation 1.13 could be written as

$$W_{AX} = -\frac{\delta_{AX}}{8(f/\#)^2} \tag{1.15}$$

$$= \frac{1}{8}\left(\frac{1}{u'}\right)^2 \left(\frac{1}{f/\#}\right)^2 C_L. \tag{1.16}$$

but:

$$f/\# = \frac{-1}{2u'} \tag{1.17}$$

And by using Eq. 1.10 **wavefront axial chromatic aberration**, W_{AX}, is obtained:

$$W_{AX} = \frac{1}{2}C_L = -\frac{y^2}{2f_d V_d}. \tag{1.18}$$

Now the meaning of C_L is clear, it indicates the amount of axial chromatic aberration in the wavefront.

1.2.2 Achromats

An achromat is a doublet consisting of two different types of glass to correct axial chromatic aberration by bringing blue and red images to a common focus. In the following the equations for achromatic doublets (assuming thin lenses) are discussed. Although these equations do not provide the exact prescriptions for real lenses, they give a good starting point for an optical design optimization program.

An achromatic doublet should satisfy two constraints:

- the total optical power of the doublet should match the desired value ϕ, and

- the lens should be free from axial color.

These two conditions could mathematically be described as

$$\phi = \phi_1 + \phi_2 \tag{1.19}$$

and

$$d\phi = d\phi_1 + d\phi_2 = 0, \tag{1.20}$$

or by Eq. 1.5

$$\begin{cases} \phi = \phi_1 + \phi_2; \\ \\ \dfrac{\phi_1}{V_{d1}} + \dfrac{\phi_2}{V_{d2}} = 0. \end{cases} \tag{1.21}$$

Then by solving Eq. 1.21

$$\begin{cases} \phi_1 = \dfrac{V_{d1}}{V_{d1} - V_{d2}}\,\phi; \\ \\ \phi_2 = -\dfrac{V_{d2}}{V_{d1} - V_{d2}}\,\phi. \end{cases} \tag{1.22}$$

Figure 1.3 (left-hand side) presents a typical example of an achromatic doublet with optical powers ϕ_1 and ϕ_2 given by Eq. 1.22. The doublet consists of a positive biconvex BK7 lens and a SF1 negative meniscus. As is expected F and C images coincide at the same focus (see chromatic focal shift diagram, Fig. 1.3 (right-hand side)). In comparison to Fig. 1.1, we have removed the primary axial color, but the lens is still suffering from chromatic aberration arising from the distance between the focus for d and the common focus for F and C light, which is known as *Secondary Spectrum*. The equations related to secondary spectrum and its correction will be discussed in Section 1.3. Now we consider more examples of achromatic lenses.

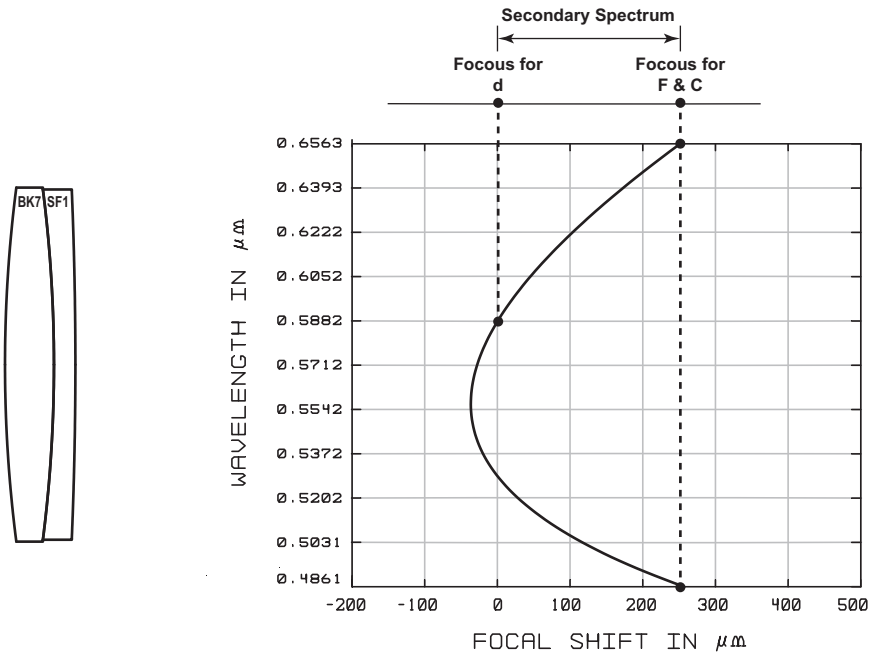

Figure 1.3: A cemented achromatic doublet consisting of a positive biconvex BK7 lens and a SF1 negative meniscus (left-hand side). The relevant chromatic focal shift diagram and the secondary spectrum (right-hand side).

Dialyte

In addition to the cemented achromat, axial chromatic aberration could be also corrected by two widely spaced lenses, a *dialyte*. The power of such a lens assuming the thin lens approximation would be obtained by [5],

$$\phi = \phi_1 + \phi_2 - t\phi_1\phi_2, \tag{1.23}$$

where t is the distance between the two lenses. For a required power, ϕ, Eq. 1.23 presents a constraint on the system. Another constraint is to make the total primary axial color equal to zero. The latter is achieved by Eq. 1.9,

$$C_{L1} + C_{L2} = 0, \tag{1.24}$$

or by Eq. 1.10,

$$\frac{y_1^2\phi_1}{V_{d1}} + \frac{y_2^2\phi_2}{V_{d2}} = 0. \tag{1.25}$$

The marginal ray height on the second lens, y_b, is given as a function of y_1 by paraxial optics equations [5]:

$$y_2 = (1 - t\phi_1)y_1. \tag{1.26}$$

Then to find the powers of the lenses in a dialyte one should solve the system of two equations below:

$$\begin{cases} \phi_1 + \phi_2 - t\phi_1\phi_2 = \phi; \\ \\ \dfrac{\phi_1}{V_{d1}} + \dfrac{(t\phi_1 - 1)^2\phi_2}{V_{d2}} = 0. \end{cases} \tag{1.27}$$

Equation 1.27 is nonlinear and most optical design books have preferred to present approximate, but more practical solutions rather than the exact solutions with square root originating from quadratic equations. We follow this practical method, and Eq. 1.28 shows the form given in *Kingslake*'s famous lens design book, [7],

$$\begin{cases} \phi_1 = \left\{ \dfrac{(t\phi_1 - 1)\dfrac{V_{d1}}{V_{d2}}}{1 + (t\phi_1 - 1)\dfrac{V_{d1}}{V_{d2}}} \right\} \phi; \\ \\ \phi_2 = -\left\{ \dfrac{1}{(t\phi_1 - 1)\left[1 + (t\phi_1 - 1)\dfrac{V_{d1}}{V_{d2}}\right]} \right\} \phi. \end{cases} \tag{1.28}$$

As an example of using these pre-design equations, let $t\phi_1 = 0.3$ and $\phi = 0.002\,\mathrm{mm}^{-1}$. Then using Eq. 1.28 we find for BK7 and SF1 glasses $\phi_1 = 5.83 \times 10^{-3}\,\mathrm{mm}^{-1}$, $\phi_2 = -5.47 \times 10^{-3}\,\mathrm{mm}^{-1}$, and $t = 51.4\,\mathrm{mm}$. Figure 1.4 shows the layout of this lens and the corresponding chromatic focal shift diagram. In the early 1800s, manufacturing a large disc of flint glass was so difficult and a dialyte in comparison to an achromatic cemented doublet had a smaller flint lens. Nowadays manufacturing flint glass is a well-established process. Nevertheless, dialyte is still a powerful implementation in some designs.

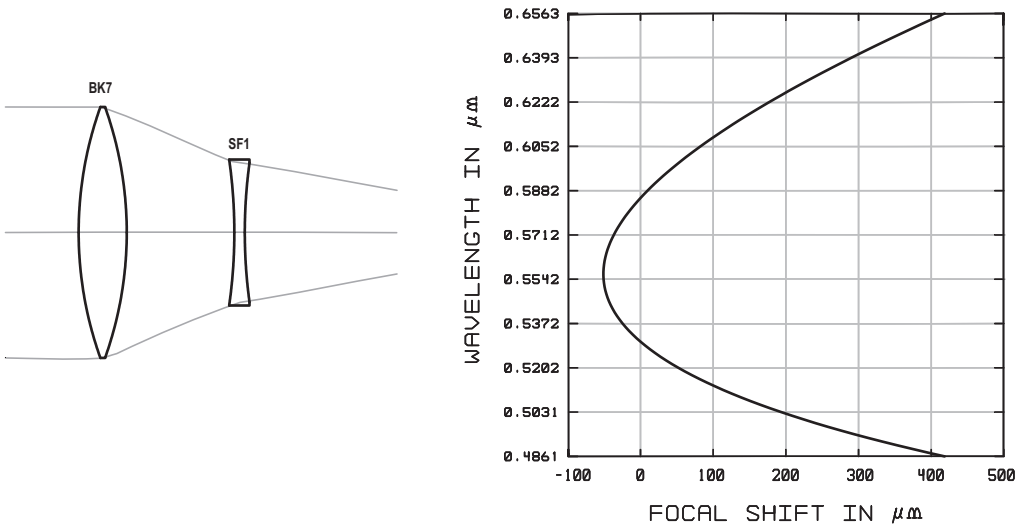

Figure 1.4: A dialyte consisting of a positive biconvex BK7 and a negative biconcave SF1 lenses (left-hand side). The corresponding chromatic focal shift diagram (right-hand side).

One-glass achromats

One can let $V_{d1} = V_{d2}$ (using the same glass for both lenses) in Eq. 1.28, then

$$\begin{cases} \phi_1 = \left[\dfrac{t\phi_1 - 1}{t\phi_1}\right]\phi; \\ \\ \phi_2 = -\left[\dfrac{1}{t\phi_1(t\phi_1 - 1)}\right]\phi. \end{cases} \tag{1.29}$$

The lens designed by Eqs. 1.29 is called one-glass achromat. Although having an achromat lens made just from one kind of glass is economic, one-glass achromats have their own limitations. By solving the first line of Eqs. 1.29 for ϕ,

$$\phi = \frac{t\phi_1^2}{t\phi_1 - 1}. \tag{1.30}$$

In Eq. 1.30, ϕ is positive if $t\phi_1 > 1$. To get a feeling about the numbers, say $t\phi_1 = 1.1$ then for $t\phi = 0.01$, t would be 400 mm. On the other hand for a typical one-glass achromat of focal length equal to 100 mm the distance between the lenses would be 400 mm. The ratio of focal length to the distance between lenses gets worse for greater amounts of $t\phi_1$, which is not practical. Therefore the use of one-glass achromats is limited to small amounts of $t\phi_1$ and negative total powers, which produce virtual images of far objects. As an example of negative powers, let $t\phi_1 = 0.3$ and $\phi = -0.002\,\mathrm{mm}^{-1}$.

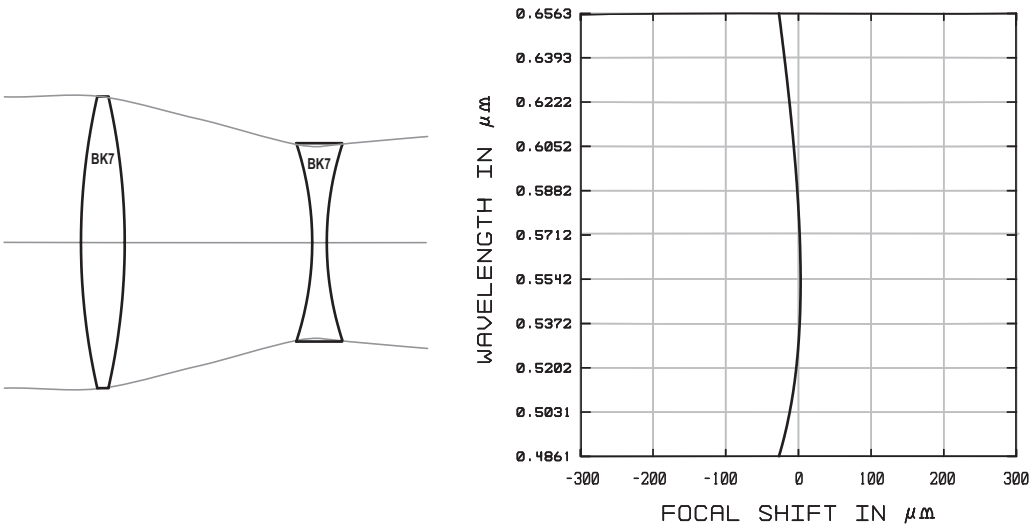

Figure 1.5: A one-glass achromat consisting of a positive biconvex and a negative biconcave BK7 lenses (left-hand side). The relevant chromatic focal shift diagram (right-hand side).

Then by Eq. 1.30, $\phi_1 = 4.67 \times 10^{-3}\,\mathrm{mm}^{-1}$, $\phi_2 = -9.52 \times 10^{-3}\,\mathrm{mm}^{-1}$, and $t = 64.3\,\mathrm{mm}$. Figure 1.5 represents a lens based on these pre-design data and its relevant focal shift diagram.

Figure 1.5 indicates that in comparison to other achromats, because of using the same type of glass for both of the lenses, one-glass achromat shows much less secondary spectrum. Secondary spectrum is discussed in detail in Section 1.3.

The configuration of the system discussed above is so similar to a Galilean telescope and one can consider a possibility of designing a one-glass achromat Galilean telescope. Unfortunately, the constraints of afocal systems and one-glass achromats cannot be satisfied simultaneously, and an afocal one-glass achromat is not possible. Then the usage of this kind of achromats is limited to taking a part in more complicated systems.

Although a one-glass achromat consisting of an-spaced doublet is not so practical, Wynne introduced a successful triple one as an paraboloidal mirror main focus corrector [8]. Figure 1.6 represents the layout of this triplet and the relevant chromatic focal shift diagram. The logic of this design and its equations could be considered as the same way as a one glass achromat but of course the relations would be more complicated. In spite of an achromatic one-glass spaced doublet, Wynne's triplet has positive power. As can be seen in Fig. 1.5 the Wynne triplet shows much less sec-

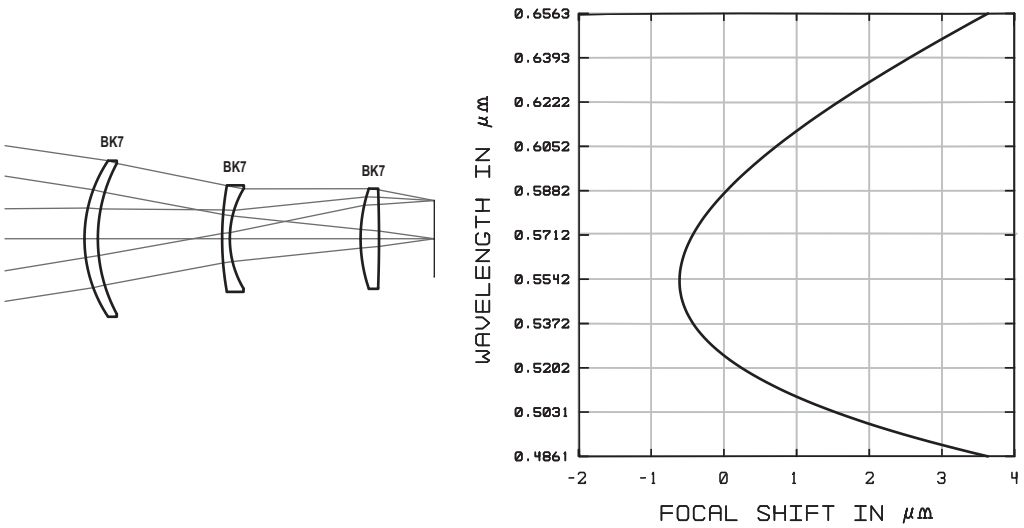

Figure 1.6: Achromatic one-glass Wynne triplet consisting of a positive meniscus, a negative meniscus, and a positive planoconvex BK7 lenses (left-hand side). The relevant chromatic focal shift diagram (right-hand side).

ondary spectrum (the scale of the diagram is 100 times less). Later, in Section 1.3.2 the Wynne triplet and its limitations will be discussed more.

1.3 Secondary spectrum and apochromats

In Section 1.2.2, Fig. 1.3 introduced secondary spectrum in achromats qualitatively. In this section, the relevant mathematical equations are discussed, and apochromats are presented as the solution of this problem.

1.3.1 Secondary spectrum

In Section 1.2, primary axial color as a function of the distance between the foci for the two extreme wavelengths has been discussed. Another useful quantity is partial primary axial color, which is defined as the distance between the foci for two arbitrary wavelengths in the spectrum range. Obviously, in the case of secondary spectrum these arbitrary wavelengths are d and C light. By starting again from a singlet paraxial power equation, Eq. 1.1,

$$\phi = (n-1)(C_1 - C_2), \tag{1.31}$$

and by taking the derivative,

$$d\phi = (C_1 - C_2)dn. \tag{1.32}$$

This prepares an equation which can be used for different intervals of spectrum. Considering $dn = (n_d - n_C)$

$$d\phi = (C_1 - C_2)(n_d - n_C). \tag{1.33}$$

Multiplying the right hand side of Eq. 1.33 by $(n_F - n_C)/(n_F - n_C)$ and rearranging it,

$$d\phi = (C_1 - C_2)(n_F - n_C)\left[\frac{(n_d - n_C)}{(n_F - n_C)}\right]. \tag{1.34}$$

We now define another quantity in optical design, **partial dispersion** P_{dc} as

$$p_{dC} = \frac{n_d - n_C}{n_F - n_C}. \tag{1.35}$$

On the other hand the Abbe V_d number is defined as

$$V_d = \frac{n_d - 1}{n_F - n_C}, \tag{1.36}$$

then Eq. 1.34 could be rewritten as

$$d\phi = (C_1 - C_2)(n_d - 1)\left(\frac{P_{dC}}{V_d}\right), \tag{1.37}$$

and finally by using Eq. 1.31

$$d\phi = \left(\frac{P_{dC}}{V_d}\right)\phi. \tag{1.38}$$

Equation 1.38 could also be considered in terms of focal length, f,

$$df = -\left(\frac{P_{dC}}{V_d}\right)f, \tag{1.39}$$

where df is **partial primary axial color**. One could notice that by the definition of Eq. 1.35, $P_{FC} = 1$. Which in this case Eq. 1.39 reduces to Eq. 1.6.

As we saw in Eq. 1.19 for a thin lens doublet system, power is given by

$$\phi = \phi_1 + \phi_2. \tag{1.40}$$

So the differential partial power is

$$d\phi_{dC} = d\phi_{dC1} + d\phi_{dC2} \tag{1.41}$$

and by Eq. 1.38:

$$d\phi_{dC} = \left[\frac{P_{dC}}{V_d}\right]_1 \phi_1 + \left[\frac{P_{dC}}{V_d}\right]_2 \phi_2. \tag{1.42}$$

By using Eq. 1.22

$$d\phi_{dC} = \frac{P_{dC1} - P_{dC2}}{V_{d1} - V_{d2}}\ \phi, \tag{1.43}$$

then in terms of focal length, f,

$$df_{dC} = -\frac{P_{dC1} - P_{dC2}}{V_{d1} - V_{d2}}\ f, \tag{1.44}$$

where df_{dC} is the **secondary spectrum of a doublet**.

The procedure used for achromatic doublets could also be implemented for other kinds of lenses. The difficulty in using this approach for dialytes and one-glass achromats is that ϕ_a and ϕ_b are functions of ϕ_a which makes the differential so complicated and impractical. Nevertheless as a qualitative assessment by Eq. 1.44 one could conclude that taking the lenses made of the same glass would vanish some terms in secondary spectrum equations. This can explain less secondary spectrum in a one-glass achromats in comparison to a dialyte or an achromatic doublet.

1.3.2 Apochromats

The aim of an apochromtic lens is bringing the foci for F, d, and C light to the same point. This implies three constraints; producing the desired total power, making primary axial color equal to zero, and correcting the secondary spectrum. To achieve those three conditions a triplet is needed, where

$$\begin{cases} \phi_1 + \phi_2 + \phi_3 = \phi; \\ \\ \dfrac{\phi_1}{V_{d1}} + \dfrac{\phi_2}{V_{d2}} + \dfrac{\phi_2}{V_{d3}} = 0; \\ \\ \left[\dfrac{P_{dC}}{V_d}\right]_1 \phi_1 + \left[\dfrac{P_{dC}}{V_d}\right]_2 \phi_2 + \left[\dfrac{P_{dC}}{V_d}\right]_3 \phi_3 = 0. \end{cases} \tag{1.45}$$

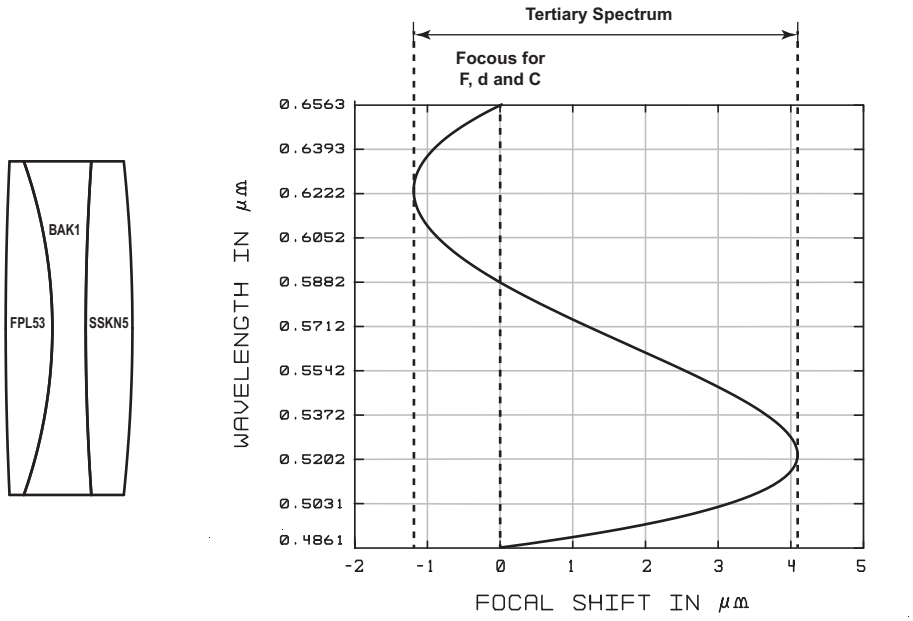

Figure 1.7: An apochromatic triplet consisting of a positive FPL53 lens, a negative BAK1 lens, and a positive SSKN5 lens (left-hand side). The relevant chromatic focal shift diagram and the tertiary spectrum (right-hand side).

By solving Eq. 1.45

$$\begin{cases} \phi_1 = \dfrac{V_{d1}(P_{dC3} - P_{dC2})}{V_{d1}(P_{dC3} - P_{dC2}) + V_{d2}(P_{dC1} - P_{dC3}) + V_{d3}(P_{dC2} - P_{dC1})}\ \phi; \\ \phi_2 = \dfrac{V_{d2}(P_{dC1} - P_{dC3})}{V_{d1}(P_{dC3} - P_{dC2}) + V_{d2}(P_{dC1} - P_{dC3}) + V_{d3}(P_{dC2} - P_{dC1})}\ \phi; \\ \phi_3 = \dfrac{V_{d3}(P_{dC2} - P_{dC1})}{V_{d1}(P_{dC3} - P_{dC2}) + V_{d2}(P_{dC1} - P_{dC3}) + V_{d3}(P_{dC2} - P_{dC1})}\ \phi. \end{cases} \tag{1.46}$$

Figure 1.7 (left-hand side) depicts a typical apochromatic triplet pre-designed by paraxial Eq. 1.46. The triplet consists of a positive FPL53 lens, a negative BAK1 lens, and a positive SSKN5 lens. The relevant chromatic focal shift diagram, Fig. 1.7 (right-hand side), shows the foci for F, d, and C light brought in the same plane. The residual chromatic aberration in this case is known as tertiary spectrum, which in comparison to the scale of Fig. 1.3 is 100 times less than the secondary spectrum.

In section 1.2.2 the Wynne triplet as an example of one-glass achromats presented. As one can see in Fig. 1.6 the secondary spectrum of this lens is so small and practically can be used as an apochromatic corrector. In comparison to apochromats, the

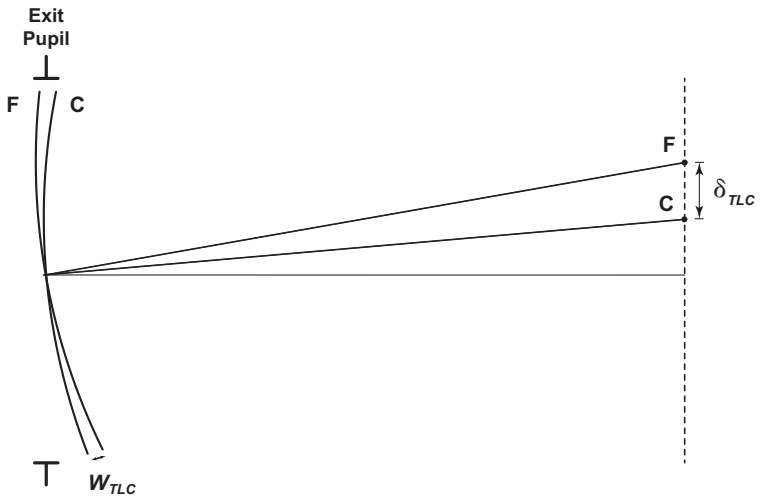

Figure 1.8: Wavefronts of a system suffering of lateral color for F and C light. W_{TLC} indicates transverse wavefront lateral chromatic aberration and δ_{TLC} indicates the relevant transverse lateral chromatic aberration.

Wynne lens is not so common. The spaces between the lenses in the Wynne triplet are necessary which make it longer than equivalent apochromat lens. On the other hand correcting a lens for chromatic aberrations is just one part of a design. Correctors should have a good flexibility to compensate all kind of aberrations and this will be so limited in one-glass lenses where the degrees of freedom do not include the materials.

1.4 Lateral color

Another kind of chromatic aberration arises when the chief rays of different wavelengths strike the image plan in different heights. This effect is known as *lateral color*. In simple systems, where we have just one element, the stop is usually located at this element. In this case, the chief ray strikes the lens at the center and assuming a thin lens, the system does not show lateral color. But when the stop is far from the lens and the chief ray sees the lens as a prism this chromatic problem will be magnified. Fig. 1.8 depicts schematic wavefronts of a system suffering from lateral color. Similar to the formulation of axial color, the extreme wavelengths here are F and C light and equivalent coefficients are defined as follows [6]:

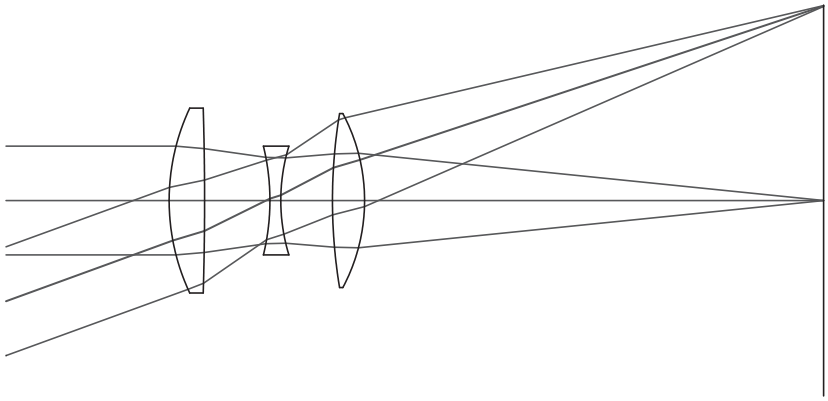

Figure 1.9: Cooke triplet corrected for lateral color; All of the lenses are made from the same kind of glass (here BK7).

Seidel lateral color coefficient, C_T,

$$C_T = \frac{y\bar{y}}{f_d V_d}, \tag{1.47}$$

where $\bar{y}$ is the height of the chief ray, and y the height of the marginal ray.

Transverse wavefront lateral chromatic aberration, W_{TLC},

$$W_{TLC} = C_T = \frac{y\bar{y}}{f_d V_d}, \tag{1.48}$$

and, **Transverse lateral chromatic aberration**, δ_{TLC},

$$\delta_{TLC} = 2(f/\#)W_{TLC} = \frac{\bar{y}}{V_d}. \tag{1.49}$$

Cooke triplet

As Eq. 1.47 shows lateral color would be corrected in symmetric systems, where y, f_d, and V_d have almost the same values at both sides of the stop, but the sign of $\bar{y}$ differs. A practical and simple system using these characteristics is the *Cooke triplet*. It consists of two positive lenses with a negative lens between them. All the lenses are made of the same glass, and the stop is located at the negative lens. Fig. 1.9 shows a typical design of this lens. In this design, lateral color caused by the front positive lens is canceled by the rear one. Since the stop is located at the negative lens, it does not add lateral color to the system.The reason for adding the negative element is to correct field curvature of the system.

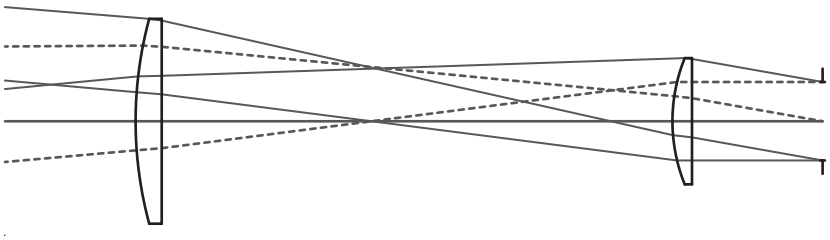

Figure 1.10: Huygens eyepiece corrected for lateral color; All of the lenses are made from the same kind of glass (here BK7).

Huygens eyepiece

Another simple system potentially corrected for lateral color is the *Huygens eyepiece*. This eyepiece consists of two planoconvex lenses made of the same kind of glass. As Fig. 1.10 depicts the Huygens design needs a virtual object and the stop is located at the eye pupil. The distance between the two lenses is the main characteristic of this design [9]. By starting from Eq. 1.23 for a spaced doublet and taking the derivative

$$d\phi = d\phi_1 + d\phi_2 - t(d\phi_1\phi_2 + \phi_1 d\phi_2). \tag{1.50}$$

Huygens assumed that the height of the rays at the lenses are almost the same. In this case according to Eq. 1.5, $d\phi = \phi_d / V_d$. Since the lenses have the same kind of glass, V_d is identical for whole of the equation. Then by equating Eq. 1.50 to zero:

$$\phi_1 + \phi_2 - 2t(\phi_1\phi_2) = 0, \tag{1.51}$$

and by rearranging Eq. 1.51:

$$2t = \frac{1}{\phi_1} + \frac{1}{\phi_1}. \tag{1.52}$$

But $1/\phi = f$, so:

$$t = \frac{f_1 + f_2}{2}, \tag{1.53}$$

which means the distance between lenses should equates the average of the focal lengths.

Although the Huygens approximation is not acceptable here, the system is surprisingly close to the optimum point where lateral color is zero. By Eq. 1.48 lateral color in this system is corrected if $C_{T1} = -C_{T2}$. Qualitatively, Fig. 1.10 shows that this condition is established here. The term $y\bar{y}$ is negative for the first lens and positive for the second one while both of them have positive powers.

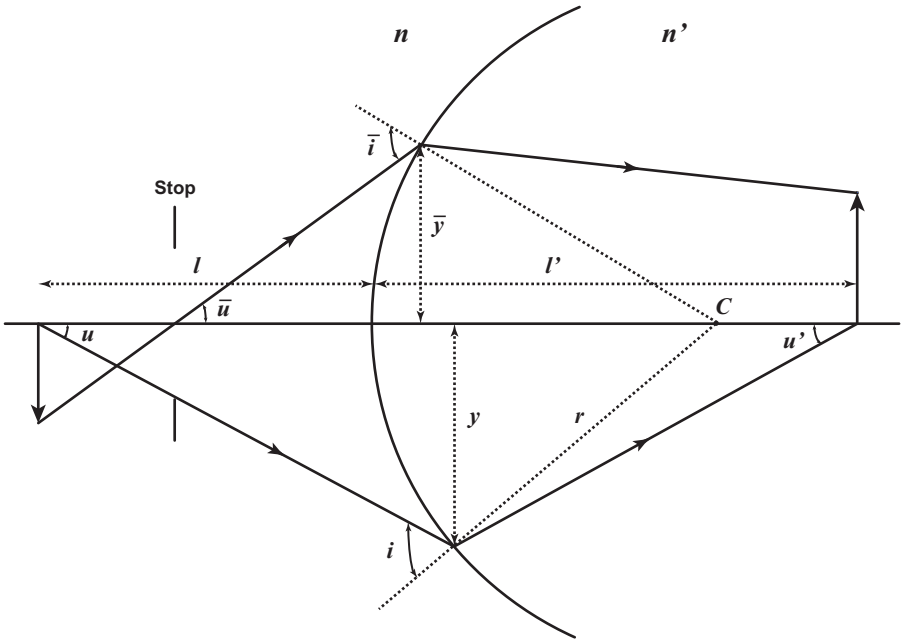

Figure 1.11: The schematic ray-tracing of the marginal and chief rays for a single surface.

1.5 Chromatic aberrations of a single surface

In Section 1.2.1 and 1.4 the contribution of a thin lens to the chromatic aberrations and the corresponding coefficients are discussed. Practically, these coefficients are very useful to pre-design an optical system. In addition to this, sometimes for special designs a closer look at the chromatic aberrations of lens surfaces is needed. In the following, imaging by a refractive surface and its effect on the chromatic aberrations are studied. Figure 1.11 depicts the schematic ray-tracing of the marginal and chief rays at the spherical interface of two different materials with refractive indices n and n'. Starting from paraxial ray-tracing, [7],

$$\frac{n'}{l'} - \frac{n}{l} = \frac{n' - n}{r}, \tag{1.54}$$

where l and l' are, respectively, the distances of the object and its image from the interface, and r is the surface radius. Writing Eq. 1.54 in F and C light and subtracting F from C gives

$$\frac{n'_C}{l'_C} - \frac{n'_F}{l'_F} - \frac{n_C}{l_C} + \frac{n_F}{l_F} = \frac{(n'_C - n'_F) - (n_C - n_F)}{r}. \tag{1.55}$$

By replacing $V_d = (n_d - 1)/(n_F - n_C)$ and approximating $l_C^2 \simeq l_F^2 \simeq l_d^2$ for the first order changes of chromatic effect we obtain

$$\frac{n'_d}{l'^2_d}(l'_F - l'_C) = \frac{n_d - 1}{V_d}\left(\frac{1}{r} - \frac{1}{l_d}\right) - \frac{n'_d - 1}{V'_d}\left(\frac{1}{r} - \frac{1}{l'_d}\right). \tag{1.56}$$

In Eq. 1.56, $(l'_F - l'_C)$ is representing **longitudinal axial chromatic aberration**, δ_{AX}. According to Fig. 1.11 for paraxial rays $l_d = -(y/u)$ and $(1/r - 1/l) = i/y$, where i is the angle of incidence with respect to the surface normal and y is the ray height at the surface. Then

$$\frac{n'_d u'^2}{y^2}\,\delta_{AX} = \frac{1}{y}\left(i\,\frac{n_d - 1}{V_d} - i\,\frac{n_d}{n'_d}\,\frac{n'_d - 1}{V'_d}\right), \tag{1.57}$$

or after rearrangement

$$\delta_{AX} = \frac{n_d y i}{n'_d u'^2}\left(\frac{n_d - 1}{n_d V_d} - \frac{n'_d - 1}{n'_d V'_d}\right). \tag{1.58}$$

And finally, Eq. 1.58 could be rewritten as

$$\delta_{AX} = \left(\frac{1}{n'_d u'^2}\right) C_L\,, \tag{1.59}$$

where the **Seidel axial color coefficient**, C_L, is defined as

$$C_L = n_d y\left(\frac{y}{r} + u\right)\left(\frac{n_d - 1}{n_d V_d} - \frac{n'_d - 1}{n'_d V'_d}\right). \tag{1.60}$$

Transverse lateral chromatic aberration, δ_{TLC}, for a single surface is achievable by a similar ray-tracing for the chief ray [10,11],

$$\delta_{TLC} = \left(\frac{1}{n'_d u'}\right) C_T. \tag{1.61}$$

C_T is **Seidel lateral color coefficient**,

$$C_T = n_d y\left(\frac{\bar{y}}{r} + \bar{u}\right)\left(\frac{n_d - 1}{n_d V_d} - \frac{n'_d - 1}{n'_d V'_d}\right), \tag{1.62}$$

where $\bar{u}$ is the angle of the chief ray and $\bar{y}$ the ray height at the surface.

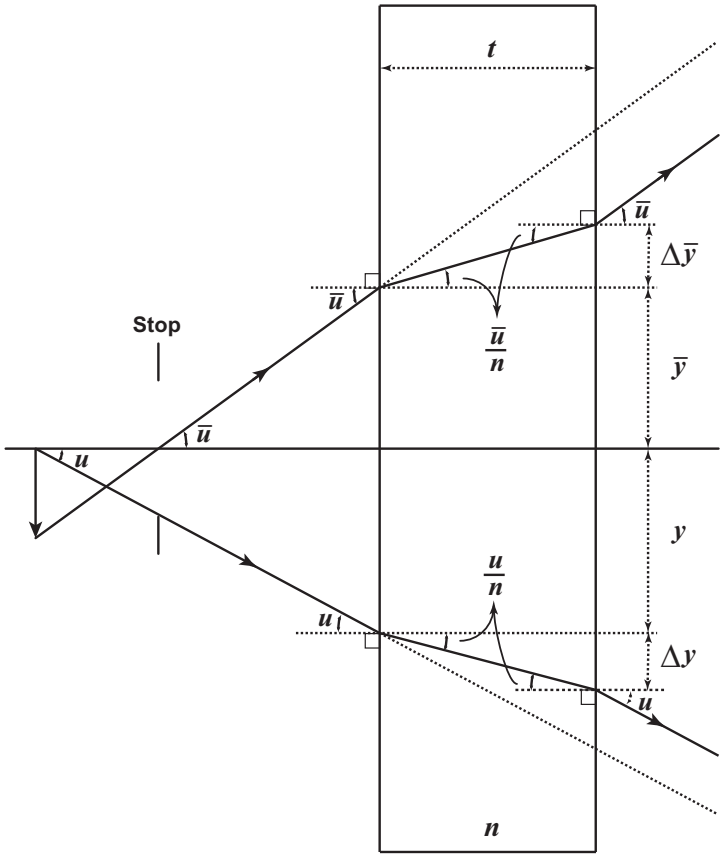

Figure 1.12: The schematic ray-tracing of the marginal and chief rays for a splane parallel plate.

1.6 Chromatic aberrations of a plane parallel plate

A plane parallel plate is the simplest element in optical design but still shows both primary chromatic aberrations. Glass plates are widely used as windows in front of the main part of the design. Also, in symmetric prismatic systems (e.g. atmospheric dispersion correctors) the design acts like a plate. These all make it worthwhile to derive the particular chromatic coefficients of such an element.

Studying Eq. 1.62 indicates that for a flat surface (where $r \to \infty$)

$$C_L = n_d y u \left(\frac{n_d - 1}{n_d V_d} - \frac{n'_d - 1}{n'_d V'_d} \right). \tag{1.63}$$

Figure 1.12 depicts a plane parallel plate with the thickness of t and the ray-tracing of the incident marginal and chief rays. It is obvious that for the first surface $n_{d1} = 1$,

$n'_{d1} = n$, $u_1 = u$, $y_1 = y$ and for the second surface $n_{d2} = n$, $n'_{d2} = 1$, $V_{d2} = V$, $u_2 = u/n$, $y_2 = y + \Delta y$, where $\Delta y = tu/n$. By using these data in Eq. 1.63 for the two surfaces of the plate in Fig. 1.12

$$C_L = C_{L1} + C_{L2} = yu\left(-\frac{n-1}{nV}\right) + n\left(y + \frac{tu}{n}\right)\left(\frac{u}{n}\right)\left(\frac{n-1}{nV}\right),$$

then

$$C_L = tu^2\left(\frac{n-1}{n^2V}\right), \tag{1.64}$$

where C_{L1}, C_{L2}, and C_L are, respectively, Seidel axial color coefficients of the surface 1, the surface 2, and the plate. And finally, according to Eq. 1.59 and by noticing that here $n'_d = 1$ and $u' = u$, a plate applies

$$\delta_{AX} = \frac{t(n-1)}{n^2V}, \tag{1.65}$$

which is independent form the object position and characteristics.

With a similar approach, by starting from Eq. 1.62 we can derive the relations for lateral color likewise.

$$C_T = C_{T1} + C_{T2} = y\bar{u}\left(-\frac{n-1}{nV}\right) + n\left(y + \frac{tu}{n}\right)\left(\frac{\bar{u}}{n}\right)\left(\frac{n-1}{nV}\right),$$

then

$$C_T = tu\bar{u}\left(\frac{n-1}{n^2V}\right), \tag{1.66}$$

where $\bar{u}$ is the angle of the chief ray and C_{T1}, C_{T2}, and C_T are, respectively, Seidel lateral color coefficients of the surface 1, the surface 2, and the plate. By using Eq. 1.67 the transverse lateral chromatic aberration of a plate is achieved as

$$\delta_{TLC} = \frac{t\bar{u}(n-1)}{n^2V}. \tag{1.67}$$

1.7 Chromatic variations of Seidel aberrations

Because of the dependence of Seidel aberrations on the refractive index of the materials they will show a variation in their wavefront for different wavelengths. Spherical aberration, coma, and astigmatism are the most important Seidel aberrations in this case. Very similar to what we did in Section 1.5, the chromatic variations of these three could be achieved by Eqs. 1.68 to 1.70, [12];

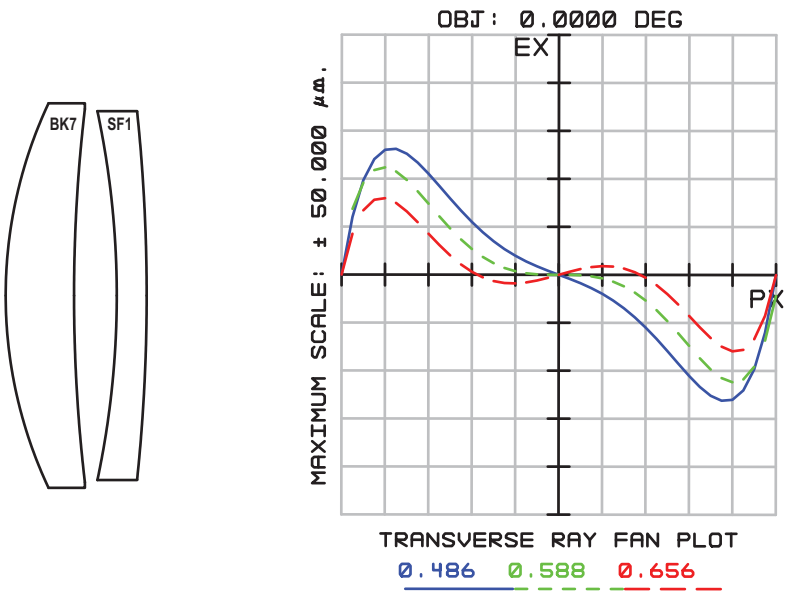

Figure 1.13: Spaced achromatic doublet corrected for sherochromatism (left-hand side). The relevant transverse ray fan plot (right-hand side).

Wavefront variations of chromatic Spherical aberration, W_{040C},

$$W_{040C} = -\frac{yn_d^2}{8}\left(\frac{y}{r}+u\right)^2\left[\frac{u'(n'_d-1)}{n'^2_d V_d}-\frac{u(n_d-1)}{n_d^2 V_d}\right], \tag{1.68}$$

Wavefront variations of chromatic coma aberration, W_{131C},

$$W_{131C} = -\frac{yn_d^2}{2}\left(\frac{y}{r}+u\right)\left(\frac{\bar{y}}{r}+\bar{u}\right)\left[\frac{u'(n'_d-1)}{n'^2_d V_d}-\frac{u(n_d-1)}{n_d^2 V_d}\right], \tag{1.69}$$

Wavefront variations of chromatic astigmatism aberration, W_{222C},

$$W_{222C} = -\frac{yn_d^2}{2}\left(\frac{\bar{y}}{r}+\bar{u}\right)^2\left[\frac{u'(n'_d-1)}{n'^2_d V_d}-\frac{u(n_d-1)}{n_d^2 V_d}\right]. \tag{1.70}$$

As a reminder, u is the incident angle of the marginal ray at the surface, y the height of that ray and r the radius of the surface. The coefficients of the chief ray are indicated by $\bar{u}$ and $\bar{y}$, and the factors for the refracted ray are distinguished by a prime sign.

Chromatic spherical aberration is the most important type amongst these aberrations. As Fig. 1.13 shows, a spaced achromatic doublet which has enough degrees of freedom to correct this aberration.

Publications overview

In this research three different problems regarding chromatic effects have been studied. The first research topic is investigating the role of chromatic lens correctors to improve imaging characteristics (*e.g.* resolution and the size of the field) in catoptric designs featuring spherical surfaces. This has been achieved by designing a new catadioptric middle-sized telescope. In the second research topic a different source of chromatic effects is taken into account: the Earth's atmosphere. The effect of atmospheric dispersion in extremely large telescopes (ELTs) can become problematic. In this part, studying the existing atmospheric dispersion corrector (ADC) designs and analyzing their drawbacks resulted in a new self-correcting ADC design. The third topic covered in this research is the chromatic effects originating from inhomogeneous refractive media. The subject of interest here is, the gradient refractive index (GRIN) lens of the eye. A new monochromatic model of the GRIN lens has been developed, which is used as the basis for a novel model of dispersive crystalline lens. These three studies and the significance of the results are discussed in depths in four separate papers published in Applied Optics, Optics Express, Journal of Biomedical Optics, and Biomedical Optics Express.

2.1 Paper I

Mehdi Bahrami and Alexander V. Goncharov:
All-spherical catadioptric telescope design for wide-field imaging
Applied Optics, **49**(30), 5705-5712 (2010)

Contributions

Before I started my Ph.D. my supervisor, Dr. Alexander Goncharov, had originally designed an $f/4.5$ Ritchey-Chrétien (RC) telescope with a $0.8m$ hyperbolic primary

mirror and a planoid secondary mirror. An achromatic two-lens field corrector was used to increase the field of view to 1.5°. To avoid the asphericity of the hyperbolic primary mirror and plano-aspheric secondary mirror, my supervisor suggested that I should start my research on finding an equivalent all-spherical catadioptric telescope design with a comparable image quality.

I designed two all-spherical catadioptric telescopes with a better image quality than the RC telescope. There was a problem in comparing my designs to the original RC design. The RC design had a two-lens field corrector, but the all-spherical systems had three-lens focus correctors. To make the comparison fair, I redesign the RC telescope with a similar three-lens corrector. This improved the performance of the RC design, but the image quality of the all-spherical designs was still comparable with the new RC design. With my supervisor's help on the structure of the manuscript I wrote Paper I, in which I had made direct comparison of the new RC telescope with the catadioptric systems. My supervisor assisted me with polishing the technical English in the manuscript, which helped me to improve my writing skills.

Catadioptric telescopes

Employing aspheric mirrors in the design of telescopes is one of the most common approaches to improve the image quality and to widen the field of view since the first reflective telescopes have been introduced. The classical RC system with a concave hyperbolic primary mirror and a convex hyperbolic mirror can provide aplantic aberration correction and is widely used in astronomical telescope design. The uncorrected astigmatism in the RC system as well as its curved image surface limits the field of view of this telescope. Employing multi-lens field correctors near the focal surface of the telescope is a practical way to achieve a wider field [13–16].

Due to manufacturing difficulties and cost concerns, historically there have been continuous effort to reduce the number of aspheric elements in optical designs. For instance, the aspheric primary mirror of telescopes can be replaced by a spherical mirror followed by catadioptric [17, 18] and catoptric [19–22] correctors. In two-mirror telescopes, a spherical primary may be followed by a spherical secondary mirror and a meniscus lens next to the secondary. The meniscus can can be made with negligible optical power, which decreases the chromatic aberrations of the lens. Any residual chromatic and monochromatic aberration can be compensated by a focus corrector. This design is known as Popov telescope. In a similar approach introduced by Klevtsov the secondary mirror can be replaced by a Mangin mirror. Although adding

a lens to a mirror increases the degrees of freedom for aberration correction, the secondary mirror here is an optically powerful component and the attached refractive surface adds a large amount of chromatic aberration to the image. Based on the design of achromatic doublets explained in Sec. 1.2.2 a well-matched meniscus lens next to the Mangin mirror can correct the chromatic aberrations and improve the image . Again, a focus corrector may be used to improve the telescope performance even further.

In Paper I, the Klevtsov and Popov systems inspired the two all-spherical catadioptric telescope designs. Despite the design of Klevtsov and Popov systems, these new all-spherical designs replace the secondary mirror of the telescope by optically powerless catadioptric groups, while an optically powerful three-lens corrector compensates the residual aberrations and provides a well-corrected image.

2.2 Paper II

Mehdi Bahrami and Alexander V. Goncharov:
The achromatic design of an atmospheric dispersion corrector for extremely large telescopes
Optics Express, **19**(18), 17099-17113 (2011)

Contributions

After publishing the first paper, my supervisor introduced me to another interesting chromatic problem, investigating the atmospheric dispersion corrector designs. Because of his previous studies on linear ADCs (LADCs), my supervisor knew that despite a common trend in using this type of ADC in ELTs, the aberrations added by the LADC wedges to the system are not negligible in fast foci. He asked me to find the problematic factors in LADCs and try to modify or redesign these ADCs in a way that they can be used in the intermediate focus of an ELT similar to the European ELT (E-ELT). In such an intermediate focus, not only the very large aperture and fast, aberrated focus may affect the performance of the ADC, but also an optically powerful mirror introduced after the intermediate focus will magnify intermediate image defects. In other words, we were looking for an ADC design, which could provide the best performance in the most restricted situation (when the original telescope design cannot be modified).

Since I did not have any background on the atmospheric dispersion effect then, my supervisor helped me to get familiar with the topic and directed me to the key papers about ADC designs. I started my work by placing an LADC in the E-ELT design. I found out that the main problem with the LADC is its axial chromatic aberration. Only the monochromatic defocus of this type of ADC can be corrected in the adaptive optics (AO) system of the telescope, but even this correction is an extra burden for the AO system. After studying other available ADC designs and examining their imaging quality in the E-ELT design I was convenced that the rotating ADCs (RADCs) have the potential to help us in this problem. The successful three-lens focus corrector in Paper I encouraged me to design a complicated three-lens RADC. Yet, finding the right glass combination for the wedges was the main challenge. Eventually, I found an optimal glass pair, completed the optimization of the design and wrote a manuscript on this study. My supervisor gave me several helpful suggestions on word selection to be more accurate in my technical writing. After submitting the manuscript, on of the reviewers asked for more analysis regarding the field dependence of the ADC optical transmittance. My supervisor helped me throughout the calculations and after the revision process, Paper II was published.

Atmospheric dispersion correction

The atmosphere can be seen as a GRIN structure with higher refractive index near the Earth's surface and a gradual decrease toward higher altitudes. In comparison to typical optical materials, the air has negligible dispersive characterstics due to its small Abbe number. Yet, for off Zenith angles, the path of the rays traveling a long distance in the atmosphere become different for different colors. This effect, known as atmospheric dispersion, adds different vertical displacements to the image of a star at different wavelengths [23], thus elongating the star image into a vertical spectrum.

The atmospheric dispersion effect is noticeable in ELTs, when the large diameter of the telescope reduces the Airy disk size and adaptive optics system provides diffraction-limited monochromatic correction [24–26]. One elegant solution to this problem is an ADC design introducing exactly the same amount of chromatic dispersion as the atmosphere but with the opposite sign. Near Zenith, astronomical observations on the ELTs do not require any atmospheric dispersion correction and the ADCs will be removed from the telescope ray-path. This means that the ADC should not change the aberration balance in the telescope design or its ray-path geometry, which imposes additional constraints on the ADC design.

A linear ADC (LADC) consisting of two simple wedges has been a practical solution to this problem [27, 28]. The two wedges can move toward each other along the optical axis to tune their accumulative dispersion to the required atmospheric dispersion correction. Although the LADC has only flat surfaces, this does not mean that this type of ADC is aberration-free. Even this simple and optically powerless design can introduce monochromatic [29] and chromatic (Sec. 1.6) aberrations when operating in converging beam. The monochromatic aberrations of an LADC can be corrected by the AO system of the telescope [30–32]. If the LADC is located close to a slow focus (*e.g.* $f/15$), the amount of chromatic aberration might be acceptable, but for LADCs located close to a fast focus (*e.g.* $f/5$) the chromatic effects can be the dominant aberration. This gets more problematic if the fast focus is followed by optically powerful mirrors, where any small aberration at the intermediate focus may be magnified by the successive optical elements of the system. In Sec. 1.2.2 it is indicated that the optical power of the surfaces is an important factor in designing achromatic optical systems. Adding optical power to the LADC surfaces will change the telescope's ray-path significantly. On the other hand, an LADC with optically powered elements acts similar to a zoom lens. One might think of adding a separate lens corrector to an LADC to compensate its chromatic aberration. It can be shown that such a lens corrector should have the optical power, which would affect the telescopes ray-path geometry.

One other type of ADCs is RADC with two identical counter-rotating Amici prisms [33], which show different vertical dispersion in their different configurations [34]. Since the distance between two Amici prisms does not change, the RADC has the potential to become achromatic by adjusting the optical power of its surfaces, where the prisms are made of suitable glasses. As mentioned before, providing an achromatic ADC is not an enough solution for this problem. There are very demanding constraint, which should be met. Spending days on finding the right glass combination for the ADC, I have eventually designed a new three-lens RADC, which can satisfy the constraints imposed at the intermediate focus of the E-ELT. This study is covered in detail in Paper II.

2.3 Paper III

Mehdi Bahrami and Alexander V. Goncharov:
Geometry-invariant gradient refractive index lens:
analytical ray tracing
Journal of Biomedical Optics, **17**(5), 55001-55009 (2012)

Contributions

People have been trying to introduce different monochromatic and chromatic models of the GRIN lens of the eye. As the third topic of research in my Ph.D., my supervisor advised me to review current monochromatic models of the eye GRIN lens and develop one of them to a chromatic model. In this process I have identified a monochromatic GRIN lens, which is based on a new approach, ideal as an starting point. I have reviewed relevant literature, in particular the materials on this innovative monochromatic model, which used a remarkable idea. This inspired me to think more about this model, and I felt that the output could be more powerful. I discussed this with my supervisor and showed my interest in developing a new monochromatic model of the eye GRIN lens. Although my supervisor found this too ambitious, he encouraged me to spend some time on the idea.

The first step was deriving a simple yet flexible mathematical expression for the surface of the lens. My supervisor introduced me to a very different expression for the shape of optical surfaces. We both agreed that this expression is a great help to this problem, but we had some discussions about the number of the terms required for a realistic lens geometry and the way that the anterior and posterior surface expressions should be connected. Although I could not completely convince my supervisor that my approach is the best way of modeling the surface of the lens, he let me continue my work as one of the acceptable approaches.

The next step was defining the interior structure of the lens. I chose a straight forward change for the lens interior shells, so that the interior structure is a scaled geometry of the outer lens surface. This optically well-defined structure encouraged me to attempt deriving paraxial ray-tracing within the lens. I derived a second-order deferential equation, which to my surprise had an analytical solution. This was a great achievement and I used it to derive analytical expressions for the optical power and other optical characteristics of the lens. To use the analytical ray-tracing in finding

the third-order aberrations of the lens, my supervisor helped me with a very useful expression for the aberrations originating from a singe surface. I derived differential equations for the third-order aberrations, which led to closed-form expressions for the total aberrations in the lens, again this is a very important result.

The main theme of my Ph.D thesis is chromatic aberration, and I wanted to focus on the chromatic effects in the crystalline lens, but since I have developed successfully the new monochromatic model for the GRIN lens, it has been decided to write a separate research article on the work. I wrote a manuscript and my supervisor checked the technical language and grammar. Paper III was published after a long reviewing process, which did not change much the material presented in the original manuscript.

Modeling the GRIN lens of the eye

The eye is a compact optical zoom system with a great performance. The optical elements in this optical system are limited to the surfaces of the cornea, the iris, and the lens of the eye. In fact, the image quality of the eye is due to the complexity of its optical elements, especially the lens structure. The crystalline lens of the eye is not homogeneous and its refractive index changes gradually from a higher index at the center to a lower index at the cortex of the lens. This GRIN structure has an important role in the eye aberration correction.

During the last century there have been many studies on the structure of the human eye GRIN lens and modeling its optical characteristics [35–39]. For years direct measurement has been the main tool in the GRIN lens experimental studies, but using recent advances in ocular aberration measurements [40], magnetic resonance imaging [41,42], optical tomography [43], optical coherence tomography imaging [44], and X-ray Talbot interferometry [45] improved our understanding of the GRIN lens structure and performance. This supported new attempts on modeling the GRIN lens.

Describing the GRIN profile by a polynomial has been the accepted approach in modeling the crystalline lens for a long time. To improve this approach, Díaz *et al.* [46] combined polynomials and trigonometric functions to achieve a more accurate representation for the crystalline lens refractive index profile. The refractive index profile of this model is parabolic, which is applicable only for very young eyes. Measurements show that the refractive index profile of the GRIN lens becomes flatter by aging [41]. The model also provides a simple paraxial ray tracing. Goncharov and Dainty [47] developed another eye model with two polynomials indicating the refractive index

profiles of the lens at the anterior and posterior hemispheres. The model supports an approximate third-order aberration calculation based on a parabolic ray-path approximation [48] and an aberration description derived for inhomogeneous media [49]. Although this model only supports fourth-order GRIN profiles, the refractive index profile of this lens model and its standard conic surfaces can be directly imported to ZEMAX optical design software, which is a great advantage.

In a very different approach, Navarro *et al.* [50] used an empirical refractive index description for the age-dependent changes at the paraxial regions of the lens, known as *power law* [51]. They defined the distribution of the GRIN lens iso-indicial contours based on this paraxial empirical formula and then derived the equivalent refractive index expression throughout the lens from this structure. The iso-indicial contours here are standard conic surfaces intersecting at steep angles resulting in sharp tips. These iso-indicial conic surfaces are concentric to the external surface of the lens. Considering the measurements on the eye, this might not be a realistic assumption [41].

Using Navarro's approach, we decided to develop a new GRIN lens model by introducing a different geometry for the iso-indicial contours and a new assumption for their spatial change. The external geometry of this new lens model can replicate the geometry of the crystalline lens with a practically simple mathematical description. The connection of the anterior and posterior surfaces is smooth and does not show any sharp tip effect. The internal structure of this GRIN lens model is a scaled representation of its external shape, where the model can be seen as a geometry-invariant GRIN lens (GIGL) model. This symmetry leads to an analytical paraxial ray tracing equation throughout the lens as well as closed-form expressions for the lens third-order aberrations. To show that the derived expressions are practically useful in the eye calculations and studies, a computational code including all optical characteristics and aberrations of the lens is developed [52]. The model can be also used in studying animal eyes and designing bio-inspired GRIN lenses. Our research is explained in detail in Paper III.

2.4 Paper IV

Mehdi Bahrami and Alexander V. Goncharov:
Geometry-invariant GRIN lens: iso-dispersive contours
Biomedical Optics Express, **3**(7), 1684-1700 (2012)

Contributions

Continuing our study on modeling the eye GRIN lens explained in Paper III, I started working on developing the GIGL model to a dispersive model. The idea was to modify the current model in a way that all the calculations and expressions stay valid for a main wavelength. I based the model on two experimental measurements of the dispersion of the center and the surface of the lens and predicted the total dispersion profile throughout the lens using the *power law*. In other words, I assumed that all chromatic refractive index profiles behave the same as the main wavelength profile but with modified coefficients characterizing the GRIN profile.

Similar to the approach used in GIGL model monochromatic aberrations derivation I derived the chromatic coefficient of the lens. These coefficients were in agreement with the experimental measurements on the chromatic aberrations of the lens and the model was successful. I wrote a manuscript on this study and my supervisor helped me with some valuable comments. Paper IV was published after a short revision process.

Iso-dispersive contours

Although there are many studies on the total chromatic aberrations of the eye, only two dispersive eye GRIN lens models have been introduced, [39] and [46]. The main problem with these two models is that they are not in agreement with the experimental data considering the dispersive structure of the lens. There are two studies with direct measurements of the dispersion of the center and the surface of the human eye lens [53, 54]. These studies depict different dispersion curves for the center and the surface of the lens, which is not taken into account in the current dispersive GRIN lens models.

Despite the limited experimental chromatic measurements currently available, the monochromatic behavior of the refractive index profile of the lens is discussed in various studies and the *power law* is an accepted expression for the GRIN lens pro-

file [41, 42, 50, 51, 55, 56]. Since the monochromatic wavelengths used in these measurements are not biologically special, we think it is a reasonable assumption that all other chromatic refractive index profiles adhere to this behavior. This is the basis for our new dispersive GRIN lens model.

In a GRIN lens structure iso-indicial contours are defined as infinitely thin layers showing the same refractive index. This concept is very useful for ray-tracing through the lens, since the refraction happens where the iso-indicial contours change. In our model we define the dispersion of the lens for its different parts and derive a coordinate dependent Abbe number for the GRIN structure. Here, the lens GRIN structure can be seen as layers with constant Abbe numbers. The chromatic effects inside the lens happen when the Abbe number is changed. Because of the analytical ray-tracing ability of this model, the contribution of each layer in chromatic aberrations can be calculated and accumulating the coefficients from each layer gives us the total chromatic aberration coefficients for the lens. It is worth mentioning that since the refractive profiles of different colors show different rates of change for their variation across the lens, the change in iso-indicial and iso-dispersive contours does not coincide.

This is the first model of a dispersive GRIN lens that is based on the expression of *power law*, which takes into account age-related variations. The chromatic aberration predicted by the model is in the range of reported experimental data in the literature [57] and it can explain different age-related chromatic behaviors observed in different studies [58–62]. This modeling and its results are the subject of Paper IV.

Conclusions, future work

Although chromatic aberration has been a subject of study for a long time, this research shows that there is much potential in this field to improve dispersive optical systems. Three different examples of optical design chromatic problems including chromatic correction in catadioptric designs, atmospheric dispersion correction in extremely large telescopes, and modeling the dispersive gradient refractive index lens of the eye are studied. These studies and our solutions to the problems are published as four separate research articles in Applied Optics, Optics Express, Journal of Biomedical Optics, and Biomedical Optics Express. The achieved designs and approaches explained in this thesis can be applied to many different problems.

This thesis covers various contributions of refractive elements in chromatic effects, but it is worth mentioning that the world of chromatic aberration is not limited to refractive elements and their dispersion. There is a growing trend in employing diffractive elements in chromatic lens correctors. Due to high Abbe number and high optical power of these diffractive elements, they can reduce the weight and the number of elements used in a refractive designs. Studying the advantages and the draw backs of such hybrid designs and exploring their possible contribution in improving different optical systems can be an attractive subject of research for future work.

Chromatic correction in catadioptric designs

The work on the middle-sized telescopes in Paper I explores undiscovered combination of lens correctors for all-spherical telescope designs. The main purpose of designing these well-matched lens correctors is improving imaging quality of an all-spherical telescope compared to an RC telescope for seeing-limited observations. Our all-spherical catadioptric telescope designs can be widely used in sky survey and wide-field imaging. The telescopes are designed for $f/4.5$ speed and 0.8 m aperture diameter, but they can be scaled to larger apertures (up to $1-2$ m), where the

limiting factor is the size of the refractive elements.

Our designs can be modified and probably improved in some aspects. It is shown in this paper that a meniscus next to the secondary mirror of a telescope can compensate the positive spherical aberration originated in the spherical primary mirror, whilst the chromatic aberration in the meniscus is balanced by a three-lens focus corrector. To modify our design, one can turn the spherical primary mirror to a paraboloidal mirror, which in terms of manufacturing is still cost effective. In this case, the primary mirror will not show any spherical aberration and the meniscus aberration correction potential can be used in correcting other aberrations. Reoptimizing such a system may provide a better image quality for short exposure imaging, where the blurring effects due to seeing can be avoided and the image quality would be limited by diffraction.

Atmospheric dispersion correction in ELTs

The study of atmospheric dispersion correction presented in Paper II aims at the complex problem of uncorrected chromatic aberration in LADCs, and as an alternative, an achromatic ADC system is designed. This ADC is a three-lens corrector, so that the first two lenses act like an RADCs design, and the third lens compensates the residual aberrations. RADCs consist of two counter-rotating Amici prisms, which their proportional rotation angle changes their total vertical dispersion.

The ADC design is examined in the intermediate focus of the E-ELT. This ADC does not change the chief ray path of the telescope at different wavelengths, and it does not add any noticeable monochromatic or chromatic aberrations to the image or the adaptive optics (AO) system, while delivering an acceptable laser guide star spot to the AO system, providing practical transmittance through the lens materials, and working close to an aberrated intermediate focus. Each of these characteristics can be employed in different problems.

The glasses coupled in this design are practically manufacturable in large blocks and because of their well-tuned dispersion can be used in a vast variety of optical designs. This can be very useful in ELT instrumentation. The presented ADC is designed to operate at R, I, and J bands, but the same approach used for this design can be employed in designing a similar ADC operating at farther infrared wavelengths like H and K bands. The design of ADCs performing near the intermediate focus of a telescope can be also extended to symmetric designs. In this case the opposite sign of the chief ray height before and after the focus can be used in compensating field

aberrations and leaves more degrees of freedom for improving image quality.

Modeling the dispersive GRIN lens of the eye

The monochromatic GIGL model introduced in Paper III, by itself, is a breakthrough. The model supports analytical ray tracing and provides analytical equations for the optical characteristics of the lens as well as closed-form expressions for its third-order aberrations. These analytical expressions are a great merit in the lens reconstruction algorithms. This model, for the first time, introduces a practically simple mathematical description for the external surface of the eye GRIN lens. This makes analyzing the accommodation of the eye more achievable.

The refractive index profile of the GIGL model is based on the well-accepted *power law* distribution. Future measurements may show small deviations from this profile, but the GIGL geometrical description can be connected to any new distribution of the refractive index profile. In addition to this, by redefining the mathematical connection between the lens internal geometry and the refractive index profile, fluctuations in the refractive index can be modeled as well as discontinuities in the lens.

The GIGL internal GRIN structure is in agreement with aged eyes more than young ones. This model can be seen as a powerful basis for some other models aiming at young eyes. In this case, we have to break the symmetry in the internal lens geometry leading to difficulties in analytical ray tracing, yet all optical characteristics of the lens model can be derived numerically using the innovative approach introduced in our third paper.

Modeling the dispersive GRIN lens of the eye in Paper IV is valuable for understanding the lens structure as well as studying its chromatic compensation. Our new dispersive GRIN lens model introduces age-related calculations for the chromatic aberrations of the lens for the first time.

Retinal imaging is a growing field nowadays and the wavelengths difference in AO laser spot and the imaging light requires a chromatic eye model to calibrate the measurements. The chromatic GIGL model explains clearly chromatic behavior for the GRIN lens of the eye. Thanks to the flexibility of the model, it can be also used in modeling the future accurate measurements of the dispersive lens. Both monochromatic and chromatic GIGL models can be also employed in animal eyes studies as well as designing bio-inspired GRIN lenses.

After the submission of Paper IV we have been continuing our work on the GIGL model. We have derived a coordinate dependent expression for the refractive index of the lens, which can be used for numerical ray tracing. Using this algorithm, we can import the lens to optical design software to widen the capability of the model in optimization processes and complete eye modeling. I have been writing a manuscript on this study for our future publication.

Appendix

In Fig. 7 of Paper I, the spot diagrams for an $f/4.5$ RC system and $f/4.5$ all-spherical catadioptric system are compared. One other way of diagnosing image defects in an optical system is studying the ray fan plots. Figure A.1 depicts the ray fan plots of the RC system and the all-spherical catadioptric system. The horizontal axis indicates the normalized pupil coordinate and the vertical axis shows the coordinate (sagittal or tangential) of the ray intercept with the image surface. The maximum height of the curves in Figure A.1 indicates the geometrical height of the spots in sagittal and tangential directions, which can be also seen in the equivalent spot diagrams in Fig. 7 of Paper I. In general, because of preserving the information about the pupil coordinate of the rays, the ray fan curves are more representative than spot diagrams in distinguishing the aberrations of the system.

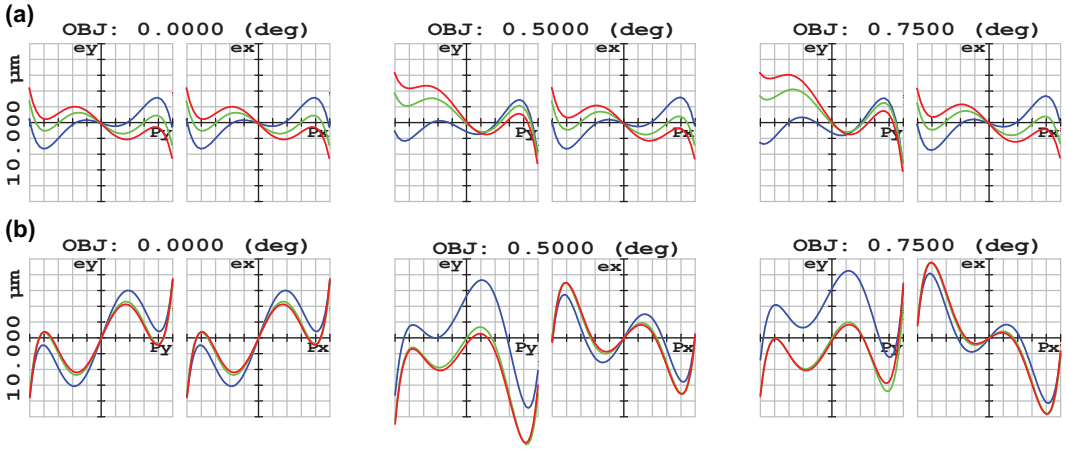

Figure A.1: Sagittal and tangential ray fan diagrams for (a) $f/4.5$ RC system and (b) $f/4.5$ all-spherical catadioptric system. The blue, green, and red lines are indicating the wavelengths of 486 nm, 588 nm, and 656 nm, respectively.

Bibliography

[1] Sir Isaac Newton, *Opticks: or, A treatise of the reflections, refractions, inflections and colours of light.* (Printed for Sam. Smith, and Benj. Walford, 1704).

[2] D. Graham Burnett, *Descartes and the Hyperbolic Quest: Lens Making Machines and Their Significance in the Seventeenth Century* (American Philosophical Society, 2005).

[3] L. Bell, *The Telescope* (Dover Publications, 1981).

[4] H. C. King, *The History of the Telescope* (Courier Dover Publications, 2003).

[5] W. J. Smith, *Modern optical engineering: the design of optical systems* (McGraw-Hill Professional, 2008).

[6] J. M. Geary, *Introduction to lens design: with practical ZEMAX examples* (Willmann-Bell, 2002).

[7] R. Kingslake and R. B. Johnson, *Lens Design Fundamentals* (Academic Press, 2010).

[8] C. G. Wynne, "A new wide-field triple lens paraboloid field corrector," Mon. Not. R. Astron. Soc. **167,** 189–98 (1974).

[9] H. Gross, F. Blechinger, and B. Achtner, *Handbook of Optical Systems, Survey of Optical Instruments* (Wiley-VCH, 2008).

[10] A. E. Conrady, *Applied Optics and Optical Design* (Oxford University Press, 1943).

[11] V. N. Mahajan, *Optical Imaging and Aberrations* (SPIE press, 1998).

[12] R. N. Wilson, *Reflecting Telescope Optics I* (Springer, 2004).

[13] R. N. Wilson, "Corrector systems for Cassegrain telescope," Appl. Opt. **7,** 253–264 (1968).

[14] C. F. W. Harmer and C. G. Wynne, "A simple wide-field Cassegrain telescope," Mon. Not. R. Astron. Soc. **177,** 25–30 (1976).

[15] C. G. Wynne, "Field correction of a Ritchey-Chrétien telescope at several focal ratios," Mon. Not. R. Astron. Soc. **193,** 7–13 (1980).

[16] C. G. Wynne, "A four-lens combined field and dispersion corrector giving telecentric imagery over a field diameter of 1.5°," Mon. Not. R. Astron. Soc. **265,** 747–754 (1993).

[17] F. Gallert, "Design examples of diffraction-limited catadioptric objective," Proc. SPIE **2774,** 143–153 (1996).

[18] D. Beach, "Ultra-high-speed wide-angle catadioptric corrector system for medium-scale spherical mirror telescopes," Opt. Eng. **42,** 405–415 (2003).

[19] L. Mertz, "Aspheric potpourri," Appl. Opt. **20,** 1127–1131 (1981).

[20] D. T. Puryayev and A. V. Goncharov, "Aplanatic four-mirror system for optical telescopes with a spherical primary mirror," Opt. Eng. **37,** 2334–2342 (1998).

[21] G. Moretto, T. A. Sebring, F. B. Ray, and L. W. Ramsey, "Aplanatic corrector designs for the extremely large telescope," Appl. Opt. **39,** 2805–2812 (2000).

[22] A. V. Goncharov, M. Owner-Petersen, and D. T. Puryayev, "Intrinsic apodization effect in a compact two-mirror system with a spherical primary mirror," Opt. Eng. **41,** 3111–3115 (2002).

[23] N. Devaney, A. V. Goncharov, and C. Dainty, "Chromatic effects of the atmosphere on astronomical adaptive optics," Appl. Opt. **47,** 1072–1081 (2008).

[24] J. Nelson and G. H. Sanders, "The status of the Thirty Meter Telescope project," in *Ground-based and Airborne Telescopes II*, L. M. Stepp and R. Gilmozzi, eds., Proc. SPIE **7012,** 70121A-1–70121A-18 (2008).

[25] S. Shectman and M. Johns, "GMT overview," in *Ground-based and Airborne Telescopes III*, L. M. Stepp, R. Gilmozzi, and H. J. Hall, eds., Proc. SPIE **7733,** 77331Y-1–77331Y-11 (2010).

[26] R. Gilmozzi and J. Spyromilio, "The 42 m European ELT: status," in *Ground-based and Airborne Telescopes II*, L. M. Stepp and R. Gilmozzi, eds., Proc. SPIE **7012,** 701219-1–701219-10 (2008).

[27] G. Avila, G. Rupprecht, and J. M. Beckers, "Atmospheric dispersion correction for the FORS Focal Reducers at the ESO VLT," in *Optical Telescopes of Today and Tomorrow*, A. L. Ardeberg, ed., Proc. SPIE **2871,** 1135–1143 (1997).

[28] A C. Phillips, J. Miller, D. Cowley, and V. Wallace, "The Keck-I Cassegrain atmospheric dispersion corrector," in *Ground-based and Airborne Instrumentation for Astronomy*, I. S. McLean and M. Iye, eds., Proc. SPIE **6269,** 62691O-1–62691O-9 (2006).

[29] C. G. Wynne and S. P. Worswick, "Atmospheric dispersion correctors at the Cassegrain focus," Mon. Not. R. Astron. Soc. **220,** 657–670 (1986).

[30] A. V. Goncharov, N. Devaney, and C. Dainty, "Atmospheric dispersion compensation for extremely large telescopes," Opt.Express **15,** 1534–1542 (2007).

[31] N. Devaney, "Review of astronomical adaptive optics systems and plans," in *Adaptive Optics for Laser Systems and Other Applications*, G. Cheriaux, C. J. Hooker, and M. Stupka, eds., Proc. SPIE **6584,** 658407-1–658407-12 (2007).

[32] M. Hart, "Recent advances in astronomical adaptive optics," Appl. Opt. **49,** D17–D29 (2010).

[33] C. G. Wynne, "Atmospheric dispersion in very large telescopes with adaptive optics," Mon. Not. R. Astron. Soc. **285,** 130–134 (1999).

[34] C. G. Wynne, "Correction of atmospheric dispersion in the infrared," Mon. Not. R. Astron. Soc. **282,** 863–867 (1996).

[35] A. Gullstrand, "Appendix II," in *Handbuch der Physiologischen Optik, 3rd ed. 1909,* J. P. Southall trans., ed. (Optical Society of America, 1924), Vol. 1, pp. 351–352.

[36] J. W. Blaker, "Toward an adaptive model of the human eye," J. Opt. Soc. Am. A **70,** 220–223 (1980).

[37] D Y. C. Chan, J. P. Ennis, B. K. Pierscionek, and G. Smith, "Determination and modeling of the 3-D gradient refractive indices in crystalline lenses," Appl. Opt. **27,** 926-931 (1988).

[38] G. Smith, B. K. Pierscionek, and D. A. Atchison, "The optical modelling of the human lens," Ophthalmic Physiol. Opt. **11,** 359–369 (1991).

[39] H. L. Liou and N. A. Brennan, "Anatomically accurate, finite model eye for optical modeling," J. Opt. Soc. Am. A **14,** 1684–1695 (1997).

[40] J. Liang, B. Grimm, S. Goelz, and J. F. Bille, "Objective measurement of wave aberrations of the human eye with the use of a Hartmann-Shack wave-front sensor," J. Opt. Soc. Am. A **11,** 1949–1957 (1994).

[41] C. E. Jones, D. A. Atchison, R. Meder, and J. M. Pope, "Refractive index distribution and optical properties of the isolated human lens measured using magnetic resonance imaging (MRI)," Vision Res. **45,** 2352–2366 (2005).

[42] S. Kasthurirangan, E. L. Markwell, D. A. Atchison, and J. M. Pope, "In vivo study of changes in refractive index distribution in the human crystalline lens with age and accommodation," Invest. Ophthalmol. Vis. Sci. **49,** 2531–2540 (2008).

[43] D. Vazquez, E. Acosta, G. Smith, and L. Garner, "Tomographic method for measurement of the gradient refractive index of the crystalline lens. II. The rotationally symmetrical lens," J. Opt. Soc. Am. A **23,** 2551–2565 (2006).

[44] A. de Castro, S. Ortiz, E. Gambra, D. Siedlecki, and S. Marcos, "Three-dimensional reconstruction of the crystalline lens gradient index distribution from OCT imaging," Opt. Express **18,** 21905–21917 (2010).

[45] M. Hoshino, K. Uesugi, N. Yagi, S. Mohri, J. Regini, and B. Pierscionek, "Optical Properties of In Situ Eye Lenses Measured with X-Ray Talbot Interferometry: A Novel Measure of Growth Processes," PLoS ONE **6,** e25140 (2011).

[46] J. A. Díaz, C. Pizarro, and J. Arasa, "Single dispersive gradient-index profile for the aging human lens," J. Opt. Soc. Am. A **25,** 250–261 (2008).

[47] A. V. Goncharov and C. Dainty, "Wide-field schematic eye models with gradient-index lens," J. Opt. Soc. Am. A **24,** 2157–2174 (2007).

[48] G. Smith and D. Atchison, "Equivalent power of the crystalline lens of the human eye: comparison of methods of calculation," J. Opt. Soc. Am. A **14,** 2537–2546 (1997).

[49] P. J. Sands, "Third-order aberrations of inhomogeneous lens," J. Opt. Soc. Am. A **60,** 1436–1443 (1970).

[50] R. Navarro, F. Palos, and L. González, "Adaptive model of the gradient index of the human lens. I. Formulation and model of aging ex vivo lenses," J. Opt. Soc. Am. A **24,** 2175–2185 (2007).

[51] G. Smith, D. A. Atchison, and B. K. Pierscionek, "Modeling the power of the aging human eye," J. Opt. Soc. Am. A **9,** 2111–2117 (1992).

[52] The geometry-Invariant lens computational code. This is a computable document format (CDF) and our source code can be accessed via Mathematica, the computational software developed by Wolfram Research (Oct. 2011), *http://optics.nuigalway.ie/people/mehdiB/CDF.html*.

[53] D. A. Palmer and J. Sivak, "Crystalline lens dispersion," J. Opt. Soc. Am. A **71,** 780–782 (1981).

[54] J. G. Sivak and T. Mandelman, "Chromatic dispersion of the ocular media," Vision Res. **22,** 997–1003 (1982).

[55] B. K. Pierscionek, "Presbyopia - effect of refractive index," Clin. Exp. Optom. **73,** 23–30 (1990).

[56] G. Smith and B. K. Pierscionek, "The optical structure of the lens and its contribution to the refractive status of the eye," Ophthalmic Physiol. Opt. **18,** 21–29 (1998).

[57] B. Gilmartin and R. E. Hogan, "The magnitude of longitudinal chromatic aberration of the human eye between 458 and 633 nm," Vision Res. **25,** 1747–1755 (1985).

[58] C. Ware, "Human axial chromatic aberration found not to decline with age," A. Graefes Arch. Klin. Exp. Ophthalmol. **218,** 39–41 (1982).

[59] P. A. Howarth, X. X. Zhang, D. L. Still, and L. N. Thibos, "Does the chromatic aberration of the eye vary with age?," J. Opt. Soc. Am. A **5,** 2087–2096 (1988).

[60] M. Millodot, "The influence of age on the chromatic aberration of the eye," A. Graefes Arch. Klin. Exp. Ophthalmol. **198,** 235–243 (1976).

[61] J. A. Mordi and W. K. Adrian, "Influence of age on chromatic aberration of the human eye," A. Graefes Arch. Klin. Exp. Ophthalmol. **198,** 235–243 (1976).

[62] N. Brown, "The change in lens curvature with age," Exp. Eye Res. **19,** 175–183 (1974).

Paper I

All-spherical catadioptric telescope design for wide-field imaging

Mehdi Bahrami* and Alexander V. Goncharov

Applied Optics Group, School of Physics, National University of Ireland Galway, Galway, Ireland

*Corresponding author: m.bahrami1@nuigalway.ie

Received 28 July 2010; revised 8 September 2010; accepted 8 September 2010;
posted 10 September 2010 (Doc. ID 132265); published 12 October 2010

The current trend in building medium-size telescopes for wide-field imaging is to use a Ritchey–Chrétien (RC) design with a multilens corrector near the focus. Our goal is to find a cost-effective alternative design to the RC system for seeing-limited observations. We present an $f/4.5$ all-spherical catadioptric system with a 1.5° field of view. The system consists of a 0.8 m spherical primary and 0.4 m flat secondary mirror combined with a meniscus lens and followed by a three-lens field corrector. The optical performance is comparable to an equivalent $f/4.5$ RC system. We conclude that, for telescopes with apertures up to 2 m, the catadioptric design is a good alternative to the RC system.

OCIS codes: 110.6770, 350.1260, 110.0110.

1. Introduction

The classical Ritchey–Chrétien (RC) system employs two hyperboloidal mirrors providing full correction of spherical aberration and coma. Because of aplanatic correction and two-mirror simplicity, the RC design has been an attractive solution for many observatories. However, the RC focal surface is curved—mimicking the shape of the secondary mirror—and astigmatism limits the field of view. These drawbacks become critical for imaging over fields wider than 15–20 arcmin.

Telescopes dedicated for wide-field imaging, such as sky survey systems, usually require fields extending over a few degrees. In addition, field curvature must be corrected to match the flat surface of modern detectors. Both conditions can be fulfilled in the RC system by introducing a multilens corrector near the Cassegrain focus [1–4]. In most designs described in the literature, the field corrector is not part of the original telescope design and is added to the telescope system for a wider field. In contrast to this *ad hoc* strategy, the lens corrector can be incorporated into telescope design from the very beginning. An example of an RC telescope with a three-lens field corrector designed this way is presented and compared to an all-spherical catadioptric system in Section 3.

0003-6935/10/305705-08$15.00/0

2. Historical Overview of Popov and Klevtsov Telescope Systems

In spite of diffraction-limited image quality achievable within a 1°–2° field, a major concern is the high cost of manufacturing and testing large aspheric mirrors. In light of this, there have been various attempts at using a spherical primary mirror to achieve a cost-effective solution for astronomical telescopes with catadioptric [5,6] and catoptric correctors [7–10]. Two examples of such systems are shown in Figs. 1(a) and 1(b). They are based on the two configurations inspired by Klevtsov [Fig. 1(a)] and Popov [Fig. 1(b)] telescope systems. Both systems use a 0.8 m spherical primary mirror M1 and a three-lens field corrector, which provides a typical f number for Cassegrain telescopes of $f/9.5$. For such an f number, the secondary group has a noticeable optical power; hence, it is easy to show the advantage of using a Mangin mirror in the Klevtsov system. The secondary group consists of a secondary mirror M2 and a meniscus lens MC. The first design shown in Fig. 1(a), features a Mangin mirror M2 as origin-

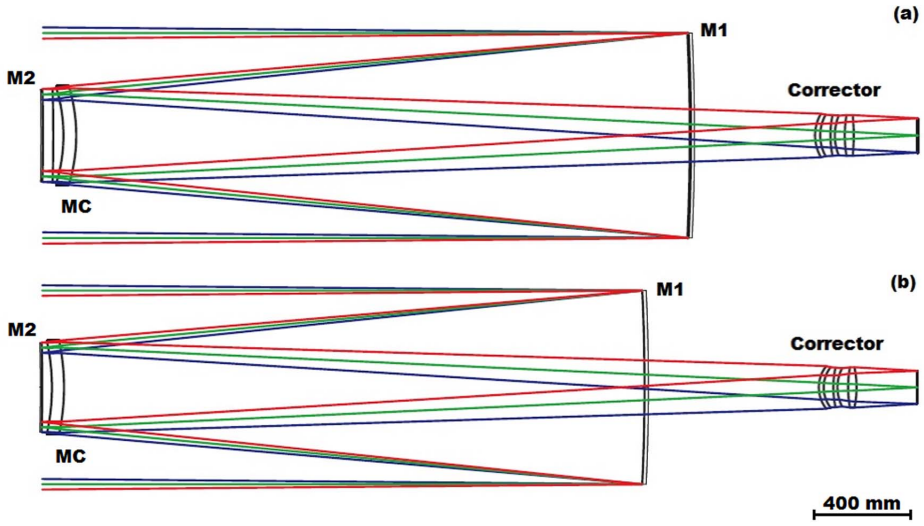

Fig. 1. (Color online) All-spherical catadioptric $f/9.5$ telescopes with a three-lens corrector, using meniscus MC and Mangin mirror M2 (a) or a convex secondary M2 (b) .

ally proposed by Klevtsov [11], while the other system uses a convex spherical secondary M2; see Fig. 1(b). The latter configuration has been proposed by Popov [12]. In its original form, the Popov system [13] did not feature any field corrector and was primarily designed to achieve aplanatic correction by optimizing the curvature and central thickness of the meniscus. The longitudinal chromatic aberration could be corrected by modifying the secondary into a Mangin mirror. As a result, we get a "quasi RC", the Klevtsov system [11], which is not so well known outside Russia. Klevtsov and Popov systems have some residual field curvature and astigmatism, limiting the field of view to 15–20 arcmin. For a wider field,

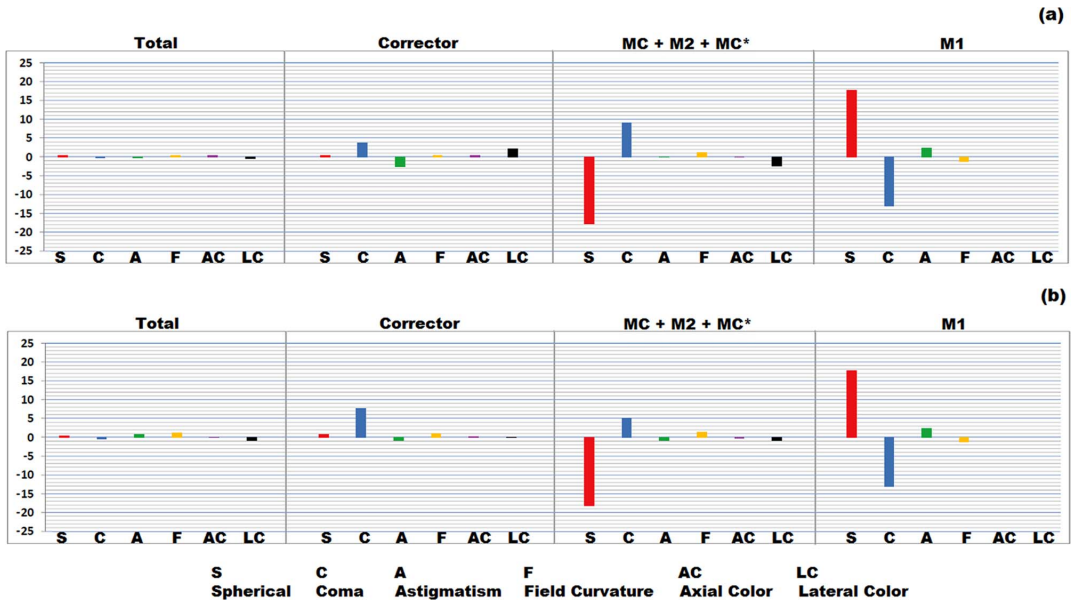

Fig. 2. (Color online) Aberration diagrams for an all-spherical catadioptric $f/9.5$ telescope with a (a) Mangin mirror and (b) secondary mirror. The vertical axis represents wave aberrations in waves ($\lambda = 588$ nm). MC* stands for the second path through the meniscus corrector.

one needs a field corrector that is capable of removing astigmatism and flattening the field.

For both design examples presented here, the field corrector is a three-lens system optimized as an integral part of the telescope and not as an *ad hoc* focal reducer [14]. The field corrector is mainly required to keep astigmatism, field curvature, and lateral color to a minimum. The secondary group corrects most spherical aberration and a large fraction of field curvature of the primary mirror. Coma correction is shared between the field corrector and the secondary group, as can be seen from the diagrams in Fig. 2. Aberration balancing enables us to obtain near diffraction-limited image quality within a 1 deg field at visible wavelengths from 486 to 656 nm.

The system with a Mangin mirror provides better correction of astigmatism and field curvature, which leads to superior image quality; see Figs. 2(a) and 2(b). This is simply because the Mangin mirror offers additional degrees of freedom (compared to the single reflective surface), namely, the glass thickness and shape factor that allow us to adjust intrinsic coma and field curvature. The Mangin mirror is commonly used as a powerful element in catadioptic designs [15,16].

The flat-field condition can be met by a particular geometry of the three-lens corrector for which its intrinsic field curvature is nearly zero. This is because the secondary group compensates for most field curvature of the primary. The Mangin mirror reduces the overall field curvature in the telescope, while the field corrector eliminates lateral color of the Mangin mirror; see Fig. 2.

In the design featuring only the secondary mirror and meniscus lens, fine-tuning of coma and field curvature is much more difficult. This rules out the flat-field solution, since the field corrector is not capable of removing field curvature and coma without the Mangin mirror. However, by leaving some small amount of residual astigmatism (undercorrecting astigmatism of the primary mirror), one can flatten the focal surface [17]. As a result, we achieve near diffraction-limited image quality within a 1° field, as shown in Fig. 3(b). The choice of a 0.8 m aperture is consistent with the pixel size available (8–10 μm) that gives an optimal sampling (2 pixels per width of the point-spread function containing 80% of encircled energy). Aberration balancing is discussed in detail in Section 4.

3. All-Spherical Catadioptric Design Versus Ritchey–Chrétien System

Rapid advances in manufacturing large-size megapixel detectors make it possible to image wider areas of the sky without compromising the telescope angular resolution. For sky survey systems with the field of view over several degrees, one has to use telescopes with a relatively fast focal ratio to keep the detector size within reasonable limits (up to 100 mm). For a 0.8 m telescope to a fit 1.5° field onto a 100 mm × 100 mm detector, one needs to use a focal ratio not greater than 4.5. This is an important requirement that dictates our choice for the optical system configurations considered here.

Figure 4(a) shows an example of a modified RC telescope with a hyperboloidal primary mirror and a planoid aspheric secondary mirror. The necessity to operate at $f/4.5$ speed with reasonable central obscuration leads to the RC system configuration in which the secondary mirror has no optical power. A dedicated three-lens field corrector eliminates all

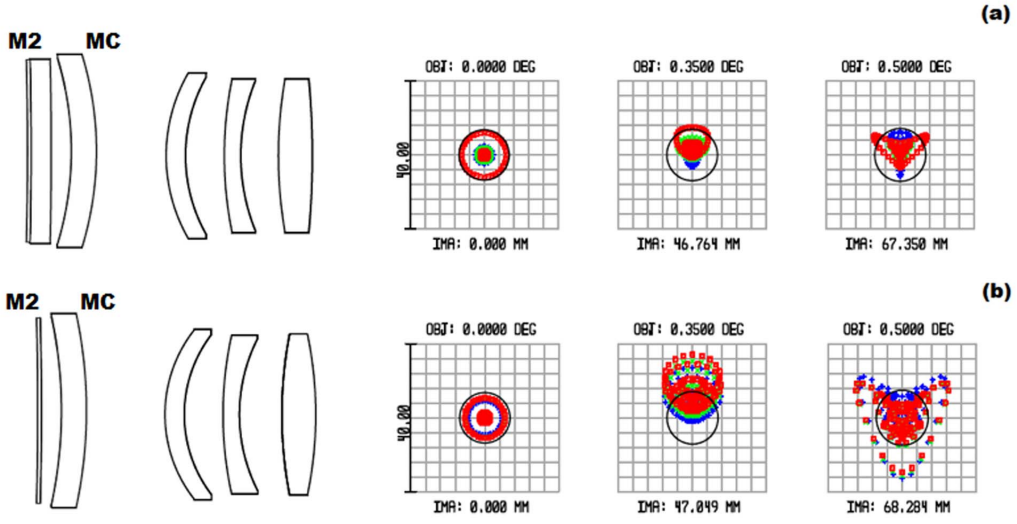

Fig. 3. (Color online) Secondary groups, field correctors, and spot diagrams for all-spherical catadioptric $f/9.5$ telescope with a (a) Mangin mirror and (b) convex secondary mirror M2.

residual aberrations of the two-mirror system, in particular astigmatism and field curvature.

The field corrector has significant intrinsic field curvature, which is matched to the field curvature of the primary mirror. By contrast, the field correctors for $f/9.5$ catadioptric systems considered in the introductory section have very little intrinsic field curvature. A more detailed coverage of aberration balancing by the three-lens field corrector is given in Section 4.

Figure 4(b) shows an $f/4.5$ all-spherical catadioptric design with a flat secondary mirror and an afocal meniscus lens followed by a three-lens field corrector. We also present an unfolded optical layout of the system in Fig. 5 to emphasize the afocal nature of the meniscus and point out the main source of filed curvature (the primary mirror). Note that MC* stands for the second path through the meniscus corrector. Similar to the RC system, the secondary group has no optical power, which is a necessary condition for achieving $f/4.5$ speed with tolerable central obscuration and an accessible focal plane position.

The lack of optical power negates the benefit of using a Mangin mirror in the secondary group because, without optical power, the Mangin mirror is unable to reduce coma and field curvature of the primary mirror [15]. However, despite a fewer degrees of freedom in the secondary group, an afocal meniscus is still the key element for compensating spherical aberration of the primary mirror and the three-lens corrector. The latter is responsible for removing overall coma, astigmatism, and field curvature, as well as reducing axial and lateral color of the meniscus lens; see Fig. 6(b).

Figure 7 depicts the spot diagrams for both designs. The modified RC system gives diffraction-limited image quality, while the all-spherical catadioptric system shows a tiny amount of lateral color and coma. In view of the wide field (1.5°) and simplicity of the secondary group (no Mangin mirror), we believe that the presented all-spherical catadioptric design is an attractive alternative to the RC system. The catadioptric design provides a cost-effective solution for sky survey telescopes that do not operate at their diffraction limit due to atmospheric seeing [18] or atmospheric dispersion [19].

The targeted group here is medium-size telescopes with apertures up to 1–2 m, which typically operate without adaptive optics (AO), unless particular attention is given to AO integration into telescope design [20–23]. Thus, the image quality of a typical medium-size telescope is limited by atmospheric seeing. The atmospheric turbulence reduces the sharpness of the image of a point source and blurs the image to the size of the seeing disk. For good seeing conditions, the radius of the seeing disk is about 0.5 arcsec, while the Airy disk radius for an 0.8 m telescope is only 0.15 arcsec.

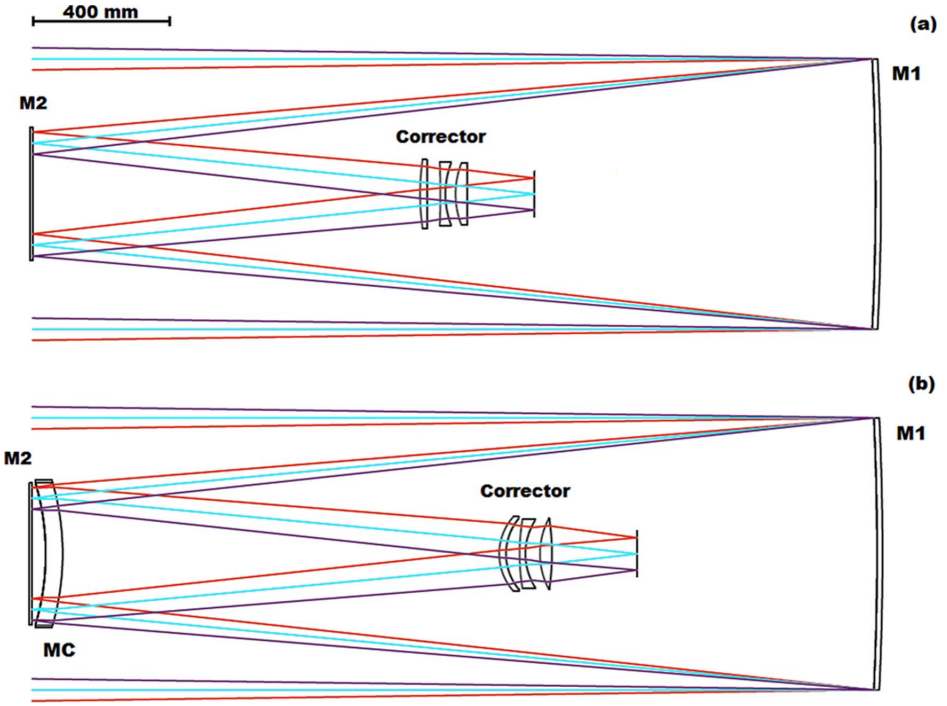

Fig. 4. (Color online) $f/4.5$ RC system with a planoid secondary and three-lens field corrector(a) and an $f/4.5$ all-spherical catadioptric system (b).

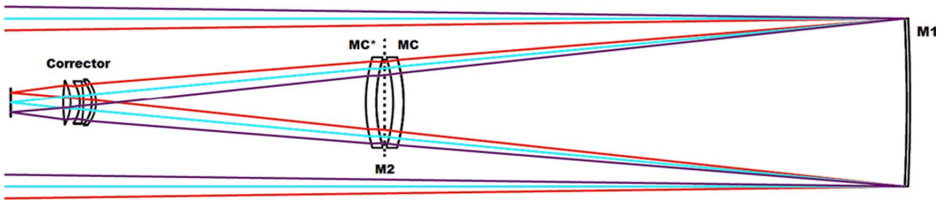

Fig. 5. (Color online) Unfolded optical layout for an $f/4.5$ all-spherical catadioptric telescope.

4. Balancing Aberrations with Three-Lens Correctors

It is well known that it is possible to correct spherical aberration, coma, and axial color in an air-spaced doublet, as well as in a cemented doublet with a special choice of a glass pair for positive and negative elements [24]. Adding a third lens makes it possible to correct for astigmatism and lateral color if the position of the aperture stop can be adjusted. A good example is a Cooke triplet [25]. In our modified $f/4.5$ RC telescope design with a three-lens corrector, the position of the aperture stop is given by the primary mirror, and thus the correction of lateral color by the symmetrical placement of lenses with respect to the aperture stop is not feasible [25]. It is necessary to introduce a third glass type in the corrector for lateral color elimination. As we showed in an earlier study, a modified RC system with a doublet field corrector suffers from lateral color [26]. Besides axial and lateral color, we also need to remove four types of monochromatic aberrations. This task is distributed between the two mirrors and the lens corrector.

Adjusting the asphericity of the primary and secondary mirrors, one could always compensate spherical aberration and coma in the field lens corrector. This helps to liberate at least two degrees of freedom in the field corrector for better elimination of other aberrations. In particular, correction of astigmatism and field curvature of the two-mirror system becomes very effective and, as a result, we get well-corrected flat field over nearly two degrees.

As an alternative configuration, one could use a spherical primary mirror followed by a secondary group combining a meniscus lens with a Mangin mirror. This combination also allows us to tune the overall amount of spherical aberration and coma in the telescope. However, in contrast to the modified RC system, the field lens corrector has to compensate a noticeable amount of lateral color originating from the secondary group; see Fig. 2(a). This condition slightly upsets the individual correction of astigmatism and field curvature in the telescope. As a result, these two aberrations have to balance one another,

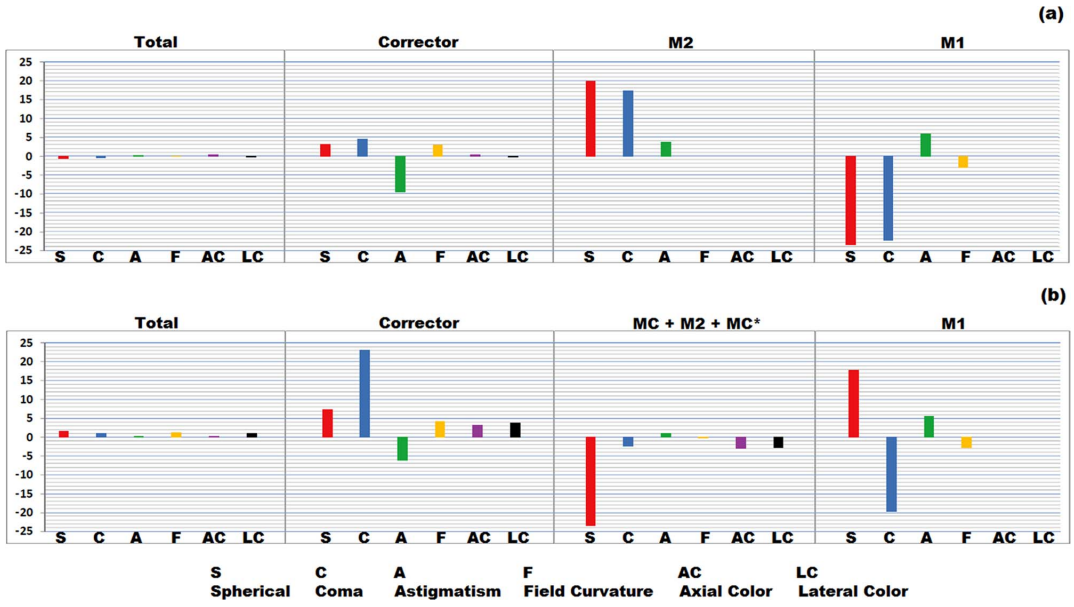

Fig. 6. (Color online) Aberration diagrams for an (a) $f/4.5$ RC system and (b) $f/4.5$ all-spherical catadioptric system, both featuring a three-lens field corrector. The vertical axis represents wave aberrations in waves ($\lambda = 588$ nm).

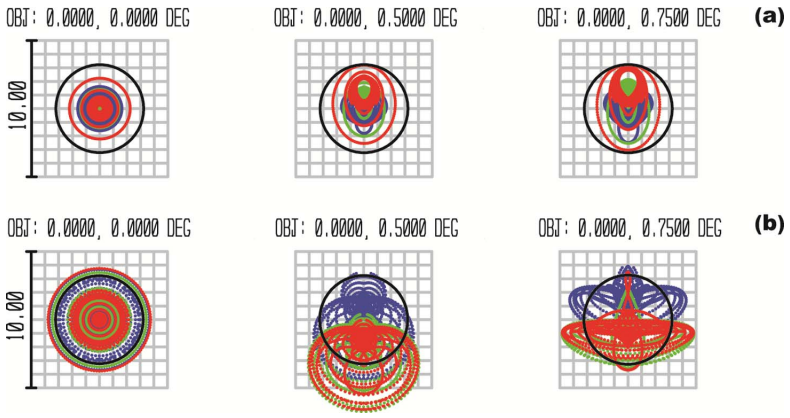

Fig. 7. (Color online) Spot diagrams for an (a) $f/4.5$ RC system and (b) $f/4.5$ all-spherical catadioptric system.

which is illustrated in Fig. 8 by vertical gray bars representing third- and fifth-order aberration coefficients [27].

It is worth noting that third-order aberration theory alone is not sufficient for finding the optimal configuration of the lens corrector. Using optimization based on real ray tracing together with basic understanding of aberration balancing in the proposed catadioptric systems proves to be more effective.

For a simplified system in which the Mangin mirror is replaced by the flat secondary, the task of coma elimination is passed on to the lens corrector. This puts an additional constraint on the lens corrector and, therefore, leads to even more pronounced residual astigmatism than is necessary to flatten the field; see the black vertical bars in Fig. 8. The choice of glass type for the meniscus lens becomes critical because it helps to reduce the lateral color in the whole system. We have considered N-SF1, N-SF2, F1, and N-BK7 glass for the meniscus lens. The latter is selected as the optimal glass for lateral color correction. The blanks of N-BK7 glass are available in large diameters so, even for a 2 m telescope, manufacturing a 1 m meniscus lens should be feasible.

It is interesting to note that when going from an $f/9.5$ to $f/4.5$ system, presented in Figs. 1(b) and 4(b), respectively, the residual lateral color changes its direction as can be seen at the intermediate field points in Figs. 3(b) and 7(b). This indicates that a better choice of glasses might be found.

5. Technical Characteristics of the 0.8 m All-Spherical Catadioptric Telescope

The main optical parameters of for the 0.8 m $f/4.5$ catadioptric telescope system are given in Table 1. One could see the recommended glasses for the three-lens field corrector used in all systems presented here.

Because the secondary group is the most distant component from the primary mirror, it is important to check the tolerances on its position. Our analysis shows that the tilt of the secondary group within ± 1.6 arcmin will reduce the diffraction encircled energy by less than 20%. This is comparable with the

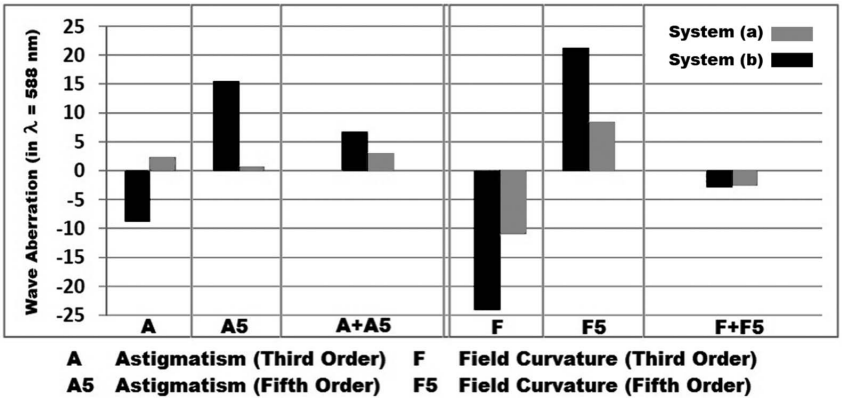

Fig. 8. Balancing field curvature against astigmatism for flat-field correction (third and fifth orders are shown) for systems presented in Fig. 1.

Table 1. Main Optical Parameters of an $f/4.5$ All-Spherical Catadioptric System for a 0.8 m Sky Survey Telescope[a]

Surface	Radius	Thickness	Glass Type	Clear Diameter
M1	−8500.00	−2400.00	MIRROR	800.25
MC	−758.30	−50.00	N-BK7	406.95
	−737.68	−40.00		392.58
M2	infinity	40.00	MIRROR	390.37
MC*	−737.68	50.00	N-BK7	388.06
	−758.30	1286.53		392.00
L1	164.50	20.00	SSKN5	178.49
	163.20	40.00		168.53
L2	616.01	17.00	BAK1	163.94
	180.36	43.90		157.15
L3	222.12	35.00	FPL53	165.00
	−711.33	250.00		163.36
Image	infinity			94.66

[a]Units are in millimeters.

tolerances of the $f/4.5$ RC system discussed in Section 3.

Figure 9 depicts the diffraction encircled energy for the central, intermediate, and edge point in the field. It is seen that 80% of encircled energy for the point on axis falls within a spot 12 μm in diameter, while the spot at the edge of the field (0.75°) is about 16 μm. The spot size is well matched to the pixel size of 8 μm commonly used for detectors in the visible region. The image scale is 0.057 arcsec/μm (one pixel covers 0.46 arcsec).

The orientation of the meniscus lens is not critical because it has no optical power; however, the suggested lens shape might help to reduce the length of the mounting assembly of the secondary group. The central obscuration due to the secondary group is less than 29% for all field points. The stray light is a notorious problem for astronomical telescopes. Three baffles are needed for our design: extended telescope tube (1.7 m); a flange at the secondary group (0.18 m long and 0.43 m in diameter); and a flange in front of the 3-lens corrector (0.2 m long). In some cases, one could use a folding flat mirror to bring the final focus outside the telescope for minimizing stray light and avoiding the unwanted central opening in the primary mirror [28].

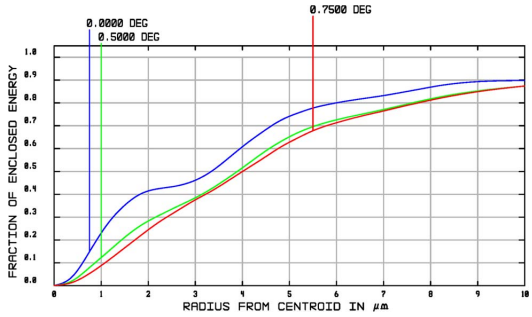

Fig. 9. (Color online) Diffraction encircled energy for the $f/4.5$ all-spherical catadioptric telescope (three field points are shown).

6. Conclusion

In this paper, we propose a simplified all-spherical catadioptric system for a sky survey telescope. Its optical performance is analyzed against a modified RC system. Both designs operate at $f/4.5$ speed and feature a three-lens field corrector optimized for 1.5° field at the visible wavelengths (from 486 to 656 nm). The basic principles of aberration balancing are discussed in detail. The primary mirror diameter is 0.8 m; however, the proposed system is intended for medium-size telescopes with an aperture up to 1–2 m, which typically operate without adaptive optics, thus being limited by atmospheric seeing. Taking into account the simplicity of the all-spherical catadioptric design and its near diffraction-limited image quality comparable to that of the RC system, we conclude that the catadioptric design provides a cost-effective solution for ground-based sky survey telescopes that do not operate at their diffraction limit due to atmospheric seeing.

This research was supported by Science Foundation Ireland under grant 07/IN.1/1906.

References

1. R. N. Wilson, "Corrector systems for Cassegrain telescope," Appl. Opt. **7**, 253–264 (1968).
2. C. F. W. Harmer and C. G. Wynne, "A simple wide-field Cassegrain telescope," Mon. Not. R. Astron. Soc. **177**, 25P–30P (1976).
3. C. G. Wynne, "Field correction of a Ritchey-Chrétien telescope at several focal ratios," Mon. Not. R. Astron. Soc. **193**, 7–13 (1980).
4. C. G. Wynne, "A four-lens combined field and dispersion corrector giving telecentric imagery over a field diameter of 1.5°," Mon. Not. R. Astron. Soc. **265**, 747–754 (1993).
5. F. Gallert, "Design examples of diffraction-limited catadioptric objective," Proc. SPIE **2774**, 143–153 (1996).
6. D. Beach, "Ultra-high-speed wide-angle catadioptric corrector system for medium-scale spherical mirror telescopes," Opt. Eng. **42**, 405–415 (2003).
7. L. Mertz, "Aspheric potpourri," Appl. Opt. **20**, 1127–1131 (1981).
8. D. T. Puryayev and A. V. Goncharov, "Aplanatic four-mirror system for optical telescopes with a spherical primary mirror," Opt. Eng. **37**, 2334–2342 (1998).

9. G. Moretto, T. A. Sebring, F. B. Ray, and L. W. Ramsey, "Aplanatic corrector designs for the extremely large telescope," Appl. Opt. **39**, 2805–2812 (2000).
10. A. V. Goncharov, M. Owner-Petersen, and D. T. Puryayev, "Intrinsic apodization effect in a compact two-mirror system with a spherical primary mirror," Opt. Eng. **41**, 3111–3115 (2002).
11. Yu. A. Klevtsov, "New optical systems for small-size telescopes," J. Opt. Technol. **67**, 176–180 (2000).
12. Yu. A. Klevtsov, "Prospects for developing Cassegrain telescopes with a corrector in convergent beams," J. Opt. Technol. **71**, 659–665 (2004).
13. G. M. Popov, *Modern Astronomical Optics* (Nauka, 1988).
14. Yu. A. Klevtsov, "Isoplanatic focal-length converter for a catadioptric telescope with a meniscus corrector," J. Opt. Technol. **73**, 535–538 (2006).
15. M. J. Riedl, "The Mangin mirror and its primary aberrations," Appl. Opt. **13**, 1690–1694 (1974).
16. A. Cifuentes, J. Arasa, and M. C. de la Fuente, "Use of Mangin and aspheric mirrors to increase the FOV in Schmidt-Cassegrain telescopes," Proc. SPIE **7100**, 71000M (2008).
17. M. J. Kidger, *Fundamental Optical Design* (SPIE, 2002).
18. P. Dierickx, "Optical performance of large ground-based telescopes," J. Mod. Opt. **39**, 569–588 (1992).
19. N. Devaney, A. V. Goncharov, and J. C. Dainty, "Chromatic effects of the atmosphere on astronomical adaptive optics," Appl. Opt. **47**, 1072–1081 (2008).
20. B. R. Brandl, R. Dekany, and R. Giovenelli, "An optimized wide-field survey telescope using adaptive optics," Proc. SPIE **4836**, 290–298 (2002).
21. A. V. Goncharov, E. Atad-Ettedgui, and J. C. Dainty, "Future giant telescopes: integration of MCAO into telescope design," Proc. SPIE **7100**, 71001I (2008).
22. A. Goncharov, M. Owner-Petersen, T. Andersen, J. Beckers, and N. Devaney, "Adaptive optics for the Euro50: design and performance," Proc. SPIE **4840**, 36–46 (2003).
23. A. Goncharov, M. Owner-Petersen, H. Riewaldt, R. Snel, and D. Walker, "The Euro50 extremely large telescope," Proc. SPIE **4840**, 214–225 (2003).
24. H. Gross, F. Blechinger, and B. Achtner, *Handbook of Optical Systems* (WILEY-VCH, 2008).
25. M. J. Kidger, *Intermediate Optical Design* (SPIE, 2004).
26. M. Bahrami, A. V. Goncharov, and C. Dainty, "All-spherical catadioptric system for 0.8 m $F/4.5$ astronomical telescope: can we compete with the Ritchey-Chrétien design?," in *International Optical Design Conference*, OSA Technical Digest (CD) (Optical Society of America, 2010), paper ITuA6.
27. H. A. Buchdahl, *Optical Aberrations Coefficients* (Dover, 1958).
28. J. Nomen, S. Sanchez, J. Guarro, J. Rodriguez, A. Garcia, and M. Blasco, "Building three compact-low cost 61 cm Klevtsov telescopes for NEO follow-up," presented at the Asteroids and Comets in Europe Conference, Višnjan, Croatia, 17–19 May 2002.

Paper II

The achromatic design of an atmospheric dispersion corrector for extremely large telescopes

Mehdi Bahrami* **and Alexander V. Goncharov**
Applied Optics Group, National University of Ireland, Galway
Galway, Ireland
*m.bahrami1@nuigalway.ie

Abstract: For off-zenith observations with ground-based astronomical telescopes, the effect of atmospheric dispersion relative to diffraction on image size increases with telescope diameter. Correction of atmospheric dispersion in extremely large telescopes (ELTs) might become critical. A common solution for ELTs is to use linear atmospheric dispersion correctors (ADCs). In spite of their simplicity, the intrinsic chromatic aberrations of linear ADCs could render diffraction-limited imaging impossible when used in a fast focus. The chromatic problems of the linear ADC in ELTs can be resolved by replacing the linear ADC by the achromatic ADC designs presented here, which provide diffraction-limited image quality and offer several opto-mechanical advantages over linear ADCs.

OCIS codes: (110.6770) Telescopes; (220.1000) Aberration compensation; (010.1300) Atmospheric propagation; (010.1080) Adaptive optics.

References and links

1. A. V. Goncharov, N. Devaney, and C. Dainty, "Atmospheric dispersion compensation for extremely large telescopes," Opt. Express **15,** 1534–1542 (2007).
2. N. Devaney, "Review of astronomical adaptive optics systems and plans," Proc. SPIE **6584,** 658407 (2007).
3. M. Hart, "Recent advances in astronomical adaptive optics," Appl. Opt. **49,** D17–D29 (2010).
4. J. Nelson and G. H. Sanders, "The status of the Thirty Meter Telescope project," Proc. SPIE **7012,** 70121A (2008).
5. S. Shectman and M. Johns, "GMT overview," Proc. SPIE **7733,** 77331Y (2010).
6. R. Gilmozzi and J. Spyromilio, "The 42 m European ELT: status," Proc. SPIE **7012,** 701219 (2008).
7. B. Delabre, "Optical design for an adaptive anastigmatic five-mirror extremely large telescope," Astron. Astrophys. **487,** 389–397 (2008).
8. E. Diolaiti, J. Conan, I. Foppiani, E. Marchetti, A. Baruffolo, M. Bellazzini, G. Bregoli, C. R. Butler, P. Ciliegi, G. Cosentino, B. Delabre, M. Lombini, C. Petit, C. Robert, P. Rossettini, L. Schreiber, R. Tomelleri, V. Biliotti, S. D'Odorico, T. Fusco, N. Hubin, and S. Meimon, "Conceptual design and performance of the multiconjugate adaptive optics module for the European Extremely Large Telescope," Proc. SPIE **7036,** 77360R (2010).
9. B. Ellerbroek, S. Adkins, D. Andersen, J. Atwood, S. Browne, C. Boyer, P. Byrnes, K. Caputa, R. Conan, R. Cousty, D. Erikson, J. Fitzsimmons, F. Gamache, L. Gilles, G. Herriot, P. Hickson, O. Lardier, P. Morin, J. Pazder, T. Pfrommer, D. Quinn, V. Reshetov, S. Roberts, J. Sinquin, M. Schoeck, M. Smith, G. Tyler, J. Vaughn, J. Veran, C. Vogel, L. Wang, and I. Wevers, "First light adaptive optics systems and components for the Thirty Meter Telescope," Proc. SPIE **7036,** 773604 (2010).
10. P. M. Hinz, A. Bouchez, M. Johns, S. Shectman, M. Hart, B. McLeod, and P. McGregor, "The GMT adaptive optics system," Proc. SPIE **7036,** 77360C (2010).
11. J. Atwood, P. Byrnes, and G. Herriot, "NFIRAOS: the optical design of an adaptive optics system for the Thirty Meter Telescope," Proc. SPIE **7439,** 74390G (2009).
12. N. Devaney, A. V. Goncharov, and C. Dainty, "Chromatic effects of the atmosphere on astronomical adaptive optics," Appl. Opt. **47,** 1072–1081 (2008).

#145240 - $15.00 USD Received 1 Apr 2011; revised 7 Jul 2011; accepted 8 Aug 2011; published 17 Aug 2011

13. G. Avila, G. Rupprecht, and J. M. Beckers, "Atmospheric dispersion correction for the FORS Focal Reducers at the ESO VLT," Proc. SPIE **2871,** 1135–1143 (1997).
14. A C. Phillips, J. Miller, D. Cowley, and V. Wallace, "The Keck-I Cassegrain atmospheric dispersion corrector," Proc. SPIE **6269,** 62691O (2006).
15. W. J. Smith, *Modern Optical Engineering* (McGraw-Hill, 2000).
16. C. G. Wynne and S. P. Worswick, "Atmospheric dispersion correctors at the Cassegrain focus," Mon. Not. R. Astron. Soc. **220,** 657–670 (1986).
17. E. Atad-Ettedgui, M. Owner-Petersen, and A. V. Goncharov, "Atmospheric dispersion effects in ELTs and their compensation," Proc. SPIE **7018,** 70181D (2008).
18. C. G. Wynne, "Atmospheric dispersion in very large telescopes with adaptive optics," Mon. Not. R. Astron. Soc. **285,** 130–134 (1999).
19. C. G. Wynne, "Correction of atmospheric dispersion in the infrared," Mon. Not. R. Astron. Soc. **282,** 863–867 (1996).
20. R. N. Wilson, *Reflecting Telescope Optics I* (Springer, 2007).
21. C. G. Wynne, "A new form of atmospheric dispersion corrector," Mon. Not. R. Astron. Soc. **262,** 741–748 (1993).
22. D. J. Jones, "Wide-field prime focus corrector for the Anglo-Australian telescope," Appl. Opt. **33,** 7362–7366 (1994).
23. L. Gilles, L. Wang, and B. L. Ellerbroek, "Impact of laser launch location on the performance of laser tomography and multiconjugate adaptive optics for extremely large telescopes," Appl. Opt. **49,** G114–G119 (2010).
24. C. Cesarsky, "The birth of the European ELT," ESO Messenger **127,** 2–3 (2007).
25. R. Gilmozzi and J. Spyromilio, "The European Extremely Large Telescope (E-ELT)," ESO Messenger **127,** 11–19 (2007).

1. Introduction

For off-zenith astronomical observations with ground-based optical telescopes, the atmospheric dispersion elongates star images to spectra with the blue end pointed toward the Zenith. This effect of the atmospheric dispersion on image size relative to the diffraction limit (Airy disk) increases with telescope diameter. Finding a suitable atmospheric dispersion corrector (ADC) for extremely large telescopes (ELTs) is a real challenge. One possible solution for atmospheric dispersion correction is to use a linear ADC (LADC) [1]. Despite the simplicity of LADCs, their intrinsic aberrations could make it difficult to achieve diffraction-limited imaging. The monochromatic aberrations are usually compensated by adaptive optics (AO) system [1–3]. In ELTs the intrinsic chromatic aberrations are not significant in slow beams (e.g. f/15), however their correction becomes critical in fast beams (faster than f/5). In ELTs, sometimes there is an intermediate fast focus, which helps to reduce the linear size of an ADC. The drawback of using a fast focus is that the chromatic aberrations of the ADC are magnified at the final slow focus. The chromatic aberrations in the final focus could prevent ELT from achieving its diffraction-limited image quality. We show an example of an ELT with an intermediate fast focus, which presents an opportunity to revisit traditional approach of atmospheric dispersion correction with new achromatic ADC design.

There are currently three ELT projects under development: Thirty Meter Telescope (TMT) [4] , Giant Magellan Telescope (GMT) [5] and the European ELT (E-ELT) [6]. In contrast to the TMT and GMT designs, which are classical aplanatic two-mirror systems, the baseline design of the European Extremely Large Telescope (E-ELT) is a 42-m five-mirror telescope with three powered aspheric mirrors. The ellipsoidal segmented primary mirror (M1) converges light toward the 6-m convex hyperboloidal secondary mirror (M2). These two mirrors make an image at the intermediate focus (F1) located 27 m after M2. The light is focused again by a 4-m concave aspheric tertiary mirror (M3) at the final focus (F2). To bring the final focus to a Nasmyth platform, the beam is folded by two flat mirrors (M4 and M5); the telescope optical layout is shown in Section 4. M4 is a 2.5-m deformable mirror designed to compensate the optical effects of atmospheric turbulence. M5 is intended for image stabilization (compensating for telescope vibrations) [7]. For a more detailed description of AO systems in the current ELT projects see Ref. [8–11].

#145240 - $15.00 USD Received 1 Apr 2011; revised 7 Jul 2011; accepted 8 Aug 2011; published 17 Aug 2011

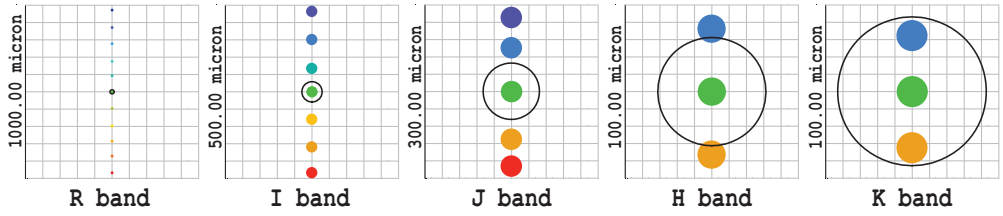

Fig. 1. Spot diagrams for the E-ELT operating at 45 deg off Zenith at different spectral bands. The black circle represents the Airy disk.

Atmospheric turbulence is not the only factor preventing diffraction-limited imaging in ELTs. Atmospheric dispersion in telescopes of such large aperture significantly elongates the image spots vertically. Figure 1 depicts the spot of the central field point of the E-ELT in the R band (0.59-0.81 μm), I band (0.78-1.02 μm), J band (1.06-1.44 μm), H band (1.5-1.7 μm), and K band (1.96-2.44 μm) at 45 degrees off Zenith. Although the spot size produced at each individual wavelength is smaller than the Airy disk (the black circle), the image of a star in the R band would appear elongated vertically by about 70 times of the Airy disk diameter. In this paper, the atmospheric dispersion effects are modeled by using ZEMAX optical design software. Various chromatic effects introduced by the atmosphere are described in more detail in Ref. [12].

To reduce the elongation of polychromatic point sources, it is essential to use an atmospheric dispersion corrector (ADC) in the telescope system. It is more practical to place an ADC at F1 rather than at the final focus F2. The linear size of the full field at F1 is about 0.6 m, whereas in the final focus F2 it is 1.95 m. Manufacturing lenses of this size is not possible and segmented lenses are not desirable in view of segmentation employed already for the primary mirror M1 and deformable mirror M4. In light of this, it has been suggested to use an LADC for the E-ELT close to F1, where the image scale is 3.5 times smaller than at F2 [7]. In spite of apparent simplicity of LADC it has some drawbacks, which are discussed in Section 2.

LADCs are not the only possibility for the E-ELT. In Section 3, we consider other types of ADC and in Section 4 we present our design of a rotating achromatic atmospheric dispersion corrector (RADC) for the intermediate focus (F1) of the E-ELT .

2. Limitations of LADC in fast focus

The linear ADC was originally proposed by Beckers in 1997 [13]. It contains two identical thin prisms (wedges) W1 and W2 with opposite orientation. The amount of longitudinal dispersion produced by the LADC is proportional to their axial separation. One of the wedges can move along the optical axis to adjust the amount of dispersion needed for different Zenith angles (Fig. 2). LADCs are commonly employed in large telescopes for compensating atmospheric dispersion [14]. LADCs work in a converging beam usually near the final focus. Both wedges are made of the same materials (usually silica because of its high optical transmittance).

The glass wedges in a converging polychromatic light produce monochromatic and chromatic aberrations [15, 16]. The amount of aberrations increases in fast foci. Linear ADCs also introduce a noticeable vertical displacement of the exit pupil and the focal surface. This unwanted displacement can be, in principle, compensated by decentering all optical elements that come after the ADC in the telescope system [1]. To reduce the required dynamic range of the deformable mirrors M4, it has been suggested to correct image motion by the tip-tilt movement of M5. A linear ADC introduces field aberrations such as coma and astigmatism, which could be corrected by AO system (using the deformable mirror M4) or by active optics using the secondary mirror M2. In principle correcting the intrinsic monochromatic aberrations of

#145240 - $15.00 USD Received 1 Apr 2011; revised 7 Jul 2011; accepted 8 Aug 2011; published 17 Aug 2011

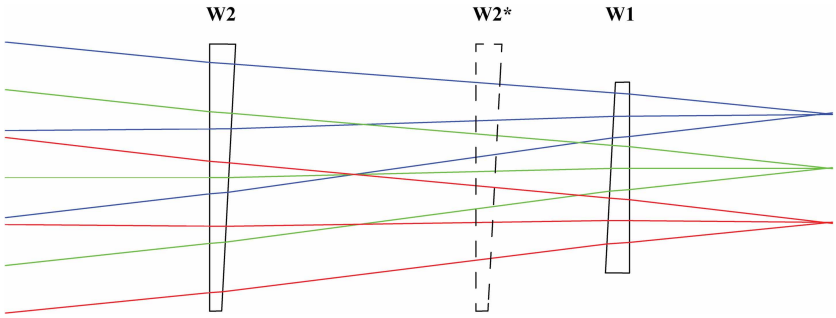

Fig. 2. A typical layout of LADC; W2 can move and tune the intrinsic dispersion of the system for different Zenith angles.

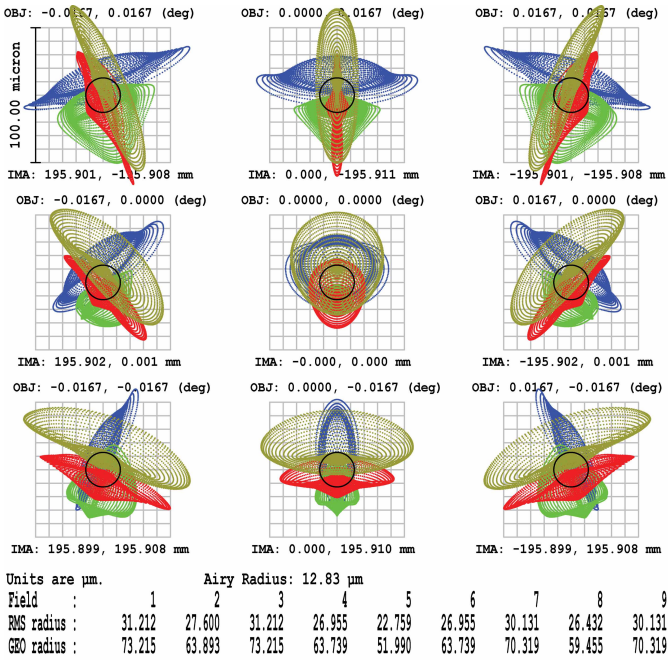

Fig. 3. The spot diagrams of a designed LADC for the E-ELT operating at 45 deg from Zenith over 2-arcmin full field.

LADC may be achieved by the combined deformation of M2 and M4, so that the demands on AO system are reduced. Since the LADCs typically operate in slow foci, chromatic aberrations are relatively small to be of any concern. However, there are two points, which make the chromatic effect of wedges critical for the E-ELT: the intermediate focus F1 is fast (f/4.6), and M3 re-images F1 to the final focus F2 (f/16), which magnifies the chromatic effects [17]. Figure 3 shows the spots of an LADC designed for 45 degrees from Zenith and 2 arcmin full field of view. The wedge angle is 1.5 deg, central thickness 40 mm, and the maximum axial separation 2 m.

The task of correcting these intrinsic chromatic aberrations of the LADC in the E-ELT is very challenging. Two wedges put together in contact form a thick glass plate. In term of chromatic effects, such a glass plate acts like a negative lens and shows positive axial color [15]:

$$\delta_{ax} = \frac{t(n-1)}{n^2 V}, \tag{1}$$

#145240 - $15.00 USD Received 1 Apr 2011; revised 7 Jul 2011; accepted 8 Aug 2011; published 17 Aug 2011

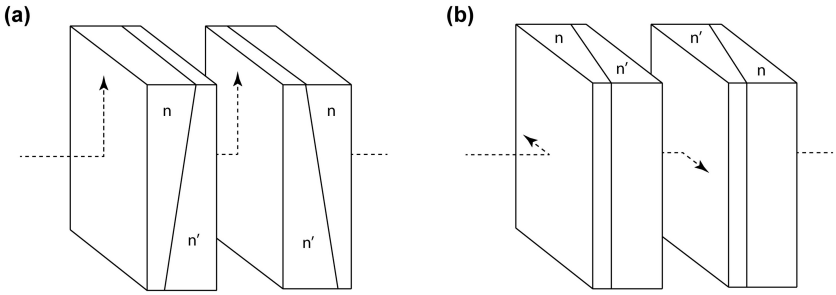

Fig. 4. A simple RADC: (a) maximum dispersion, (b) zero dispersion.

where δ_{ax} is the axial chromatic aberration of the plate, n the refractive index, t the thickness of the plate, and V the Abbe number. Correcting the axial color of such a plate requires a positive compensating lens. Because of the significant thickness of the plate ($t = 80mm$) the needed optical power of a single positive lens would make it the most powerful element in the telescope. This lens will affect the rest of the telescope system after F1 leading to a different geometry of the light path, pupil mis-conjugations in the AO system, and vignetting. One could avoid excessive optical power by using a two-lens corrector instead, however due to high level of aberrations at F1 (see Section 6) the two-lens corrector does not have sufficient number of degrees of freedom to keep the telescope achromatic. In this case only three-lens corrector is able to provide achromatic correction. Instead of using F1, one can think of adding a lens corrector close to the final focus F2, but the size of the usable image is limited by the diameter of the lens (which can be as large as 1 m at most). Alternative ADC designs are discussed in the following section.

3. Other types of ADCs

Before introduction of LADCs, rotating ADCs were the common solution for atmospheric dispersion. The simplest type of RADC contains two identical counter-rotating plates, so called Amici prisms [18]. Each plate is made of two cemented prisms. The ADC will show its maximum (zero) dispersion when the apex angles of the prisms are in the same (opposite) directions, see Fig. 4 and Ref. [19]. This simple RADC is used in collimated light (typically in the pupil plane).

An *ideal* ADC compensates for atmospheric dispersion and also provides zero-deviation for the chief rays at the reference wavelength to preserve the pupil position in the telescope. In LADCs there are two identical prisms and the tilt of the pupil plane introduced by the first prism is corrected by the second one. The rotation of prism pairs in an RADC is the basis for its function, however the angles between the two interfaces in prism pairs depends on the Zenith angle. This means that each plate should fulfill the zero-deviation condition individually. This can be achieved in two ways. The first method is to add appropriate tilts to the outer surfaces of the plates insuring that the outgoing ray will be parallel to the incoming ray. In this case, the vertical displacement like the one found in LADCs is applied to outgoing rays. The second method is to use two different types of glasses for the prisms, which show different dispersions, but the same refraction index at some prime wavelength. Such an ADC does not present any tilt or even vertical displacement in the image at this mean wavelength. Finding these two glasses is the main challenge. In addition to the requirement of having a certain common point in the dispersion curves, their differential dispersion should match the atmospheric dispersion as close as possible. In Section 7, we show that it is possible to find such glass pair.

The exit pupil of the E-ELT is located close to M4, where the diameter of the beam is even

#145240 - $15.00 USD Received 1 Apr 2011; revised 7 Jul 2011; accepted 8 Aug 2011; published 17 Aug 2011

larger than the field diameter at the final focus F2. Using an RADC in a convergent beam introduces noticeable amount of aberrations. To avoid this problem, optical designers usually introduce some curvature on the surfaces [20]. Although this can in principle improve monochromatic aberrations, chromatic aberrations might get worse. A surface with some optical power introduces more axial and lateral color than a flat surface. Correcting chromatic aberrations is related to the curvature of the surfaces as well as the material of the elements. This makes the design of such an ADC more complicated and the process of finding the suitable glasses difficult.

Historically optical designers have tried different ideas to improve the performance of RADCs in a converging beam. Wynne suggested making the surfaces of the wedges concentric to the focal plane [21]. This eliminates axial color and gives a better aberration correction. Since concentric lenses are powerful elements and they will drastically change the configuration of the telescope, this design is not helpful in the E-ELT. What is needed here is an *ad hoc* design, which solves the atmospheric dispersion problem and, at the same time, does not change anything else in the telescope system.

Apart from concentric ADCs, there have been some work on adding more lenses to RADC operating as a focal corrector [20, 22]. A new kind of an RADC for the E-ELT inspired by this work is presented in Section 4.

4. The achromatic design of ADC for the E-ELT

Figure 5 presents an optical layout of the E-ELT featuring the new achromatic design of the RADC. The ADC consists of three lenses and it is located near the intermediate focus F1. The first two lenses, L1 and L2, are the counter rotating elements, which tune the intrinsic dispersion of the ADC for different Zenith angles. The third lens L3 preserves the geometry of the beam at F1. Therefore, L3 makes the ADC an afocal system and it also corrects for the residual aberrations of L1 and L2. It is worth pointing out that in contrast to linear ADCs, the proposed ADC does not use any tilt or decentering of M3, M4 and M5. The diameter of the largest lens covering the 10-arcmin full technical field is less than 780 mm and the total length of the ADC is less than 850 mm. The range of rotation angles for L1 and L2 (0 deg to 90 deg) provides the atmospheric compensation up to 55 deg from Zenith. The glasses used are S-PHM52 and N-F2 for L1 and L2, and F5 for L3. As can be seen from Table 1, these glasses have high transmittance between 500 nm and 1530 nm. This is the achievable range for the ADC designs presented here.

Table 1. The Transmittance Coefficients for Silica and the Glasses Used in the ADC

λ (nm)	Transmittance for 10 mm thickness			
	Fused Silica	S-PHM52	N-F2	F5
1530	0.999	0.993	0.991	0.995
1060	0.999	0.996	0.998	0.999
700	0.999	0.998	0.997	0.999
660	0.999	0.998	0.996	0.998
620	0.999	0.998	0.996	0.998
580	0.999	0.998	0.997	0.998
546	0.999	0.998	0.997	0.998
500	0.999	0.996	0.994	0.998

To keep the pupil and M4 conjugations unchanged special constraint on the position of the exit pupil in the optimization merit function is used. The exit pupil of the E-ELT is located 590 mm after M4, whereas deformable mirror M4 is conjugated to an atmospheric layer that

#145240 - $15.00 USD Received 1 Apr 2011; revised 7 Jul 2011; accepted 8 Aug 2011; published 17 Aug 2011

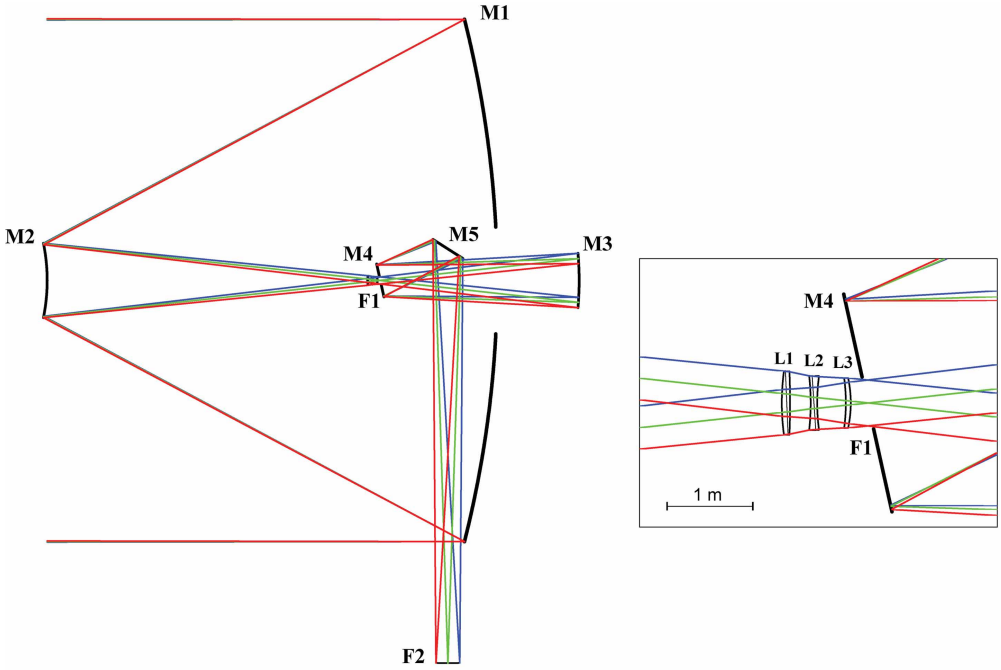

Fig. 5. The optical layout of the E-ELT featuring the new design of the three-lens rotating achromatic ADC.

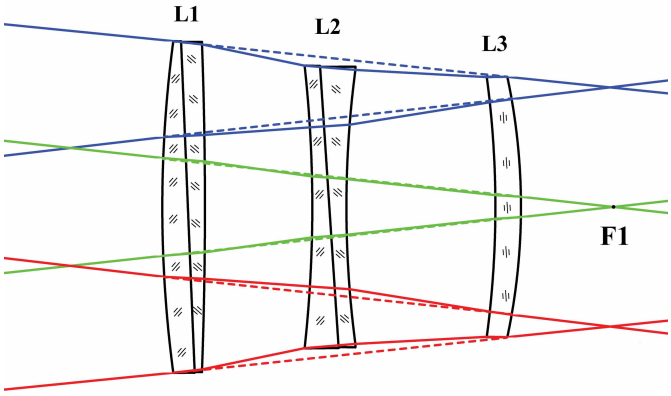

Fig. 6. The three-lens achromatic ADC with the unchanged path of the rays.

is about 200 m above the primary mirror M1. Since the path of the rays is not changed by the ADC (see Fig. 6), the ADC preserves this conjugation in the telescope.

Another constraint in the E-ELT is the image quality of a turbulent layer on M4. This is of high importance for successful operation of the adaptive optics (AO) system. Since the atmospheric correlation length r_0 is smaller in the B (0.391-0.489 μm) and V (0.505-0.595 μm) bands compared to the R band, the performance of the AO system will not be as effective. For this reason, we have designed the ADC for the R, I and J bands. As can be seen in Fig. 1, the atmospheric dispersion correction in the H and K bands is not critical. The main ADC should be removed from the telescope when operating in those bands. For the R band, the E-ELT gives nearly diffraction-limited image of a turbulent layer on M4. Adding the ADC near F1 reduces the quality of the turbulent layer image on M4, but is still acceptable for the AO system. The image size of the atmospheric correlation length $r_0 = 300$ mm on M4 is about 18 mm. The

#145240 - $15.00 USD Received 1 Apr 2011; revised 7 Jul 2011; accepted 8 Aug 2011; published 17 Aug 2011

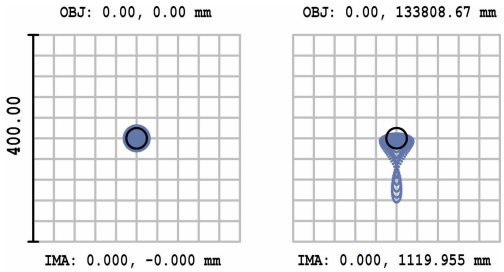

Fig. 7. The image of an LGS situated at 92 km altitude above the E-ELT.

image spot size is smaller than 1.5 mm, which is only 8% of the image size of r_0 on M4. Thus, this gives sufficient resolution for the deformable mirror M4 to correct atmospheric turbulence.

The AO system requires laser guide stars (LGSs) for wavefront sensing at any point in the sky, especially when there is no sufficiently bright natural star available near the science object. LGSs are essential for laser tomography of the atmospheric turbulence [23]. The E-ELT is an LGS-friendly telescope [24, 25], since the LGS spots are comparable to the airy disk (see Fig. 7). Adding the ADC to the telescope affects the image quality of LGSs. To restore the original quality of LGSs, a dedicated monochromatic correctors could be applied in front of the LGS wavefront sensors.

The spot diagrams of the 2-arcmin full field in the R band for three different Zenith angles are presented in Fig. 8, which also shows the corresponding orientations of the counter-rotating lenses L1 and L2.

In the R band, the achromatic ADC does not need any aberration correction by AO system. The RMS of the spots is smaller than the Airy disk at Zenith angles less than 45 deg. Even at 55 degrees from Zenith, the spots are still near diffraction limited over the 2-acrmin full field. As can be seen from the spot positions in Fig. 8, contrarily to the LADC, the proposed ADC design does not introduce any image displacement in the vertical direction. This has been achieved by a proper choice of the glasses for L1 and L2. As discussed in Section 3, the prime wavelength here is the point at which the dispersion curves meet (Fig. 9). As mentioned in Section 3, there are two methods for achieving a zero deviation condition in an ADC. Because of the fast focus and the giant size of the aperture in the E-ELT, it is better to use the second method than introducing a tilt at the external surfaces of the prisms. Tilting powered surfaces to achieve the zero-deviation condition would result in a noticeable amount of residual aberrations in the E-ELT.

The ADC has also a good performance in the I and J bands (Fig. 10).In this case, a small compensation for defocus is needed, which is much less than what is required for an LADC in the original design of the E-ELT.

Figure 11 shows the centroid motion of an NGS (in milli-arcseconds) as a function of wavelength (from 0.6 to 1.6 microns) after correction of atmospheric dispersion with a linear ADC and achromatic ADC operating in the R band. The centroid position is given for an NGS that is located at the edge of the 2 acrmin full field for a representative Zenith angle of 45 deg. It is clear that the residual chromatic effect in the achromatic ADC design is 5 times smaller than that of the linear ADC. To compensate this residual effect one could use a dedicated ADC for the NGS wavefront sensor. This could be achieved with an Amici prism pair placed near the pupil in the NGS wavefront sensor.

#145240 - $15.00 USD Received 1 Apr 2011; revised 7 Jul 2011; accepted 8 Aug 2011; published 17 Aug 2011

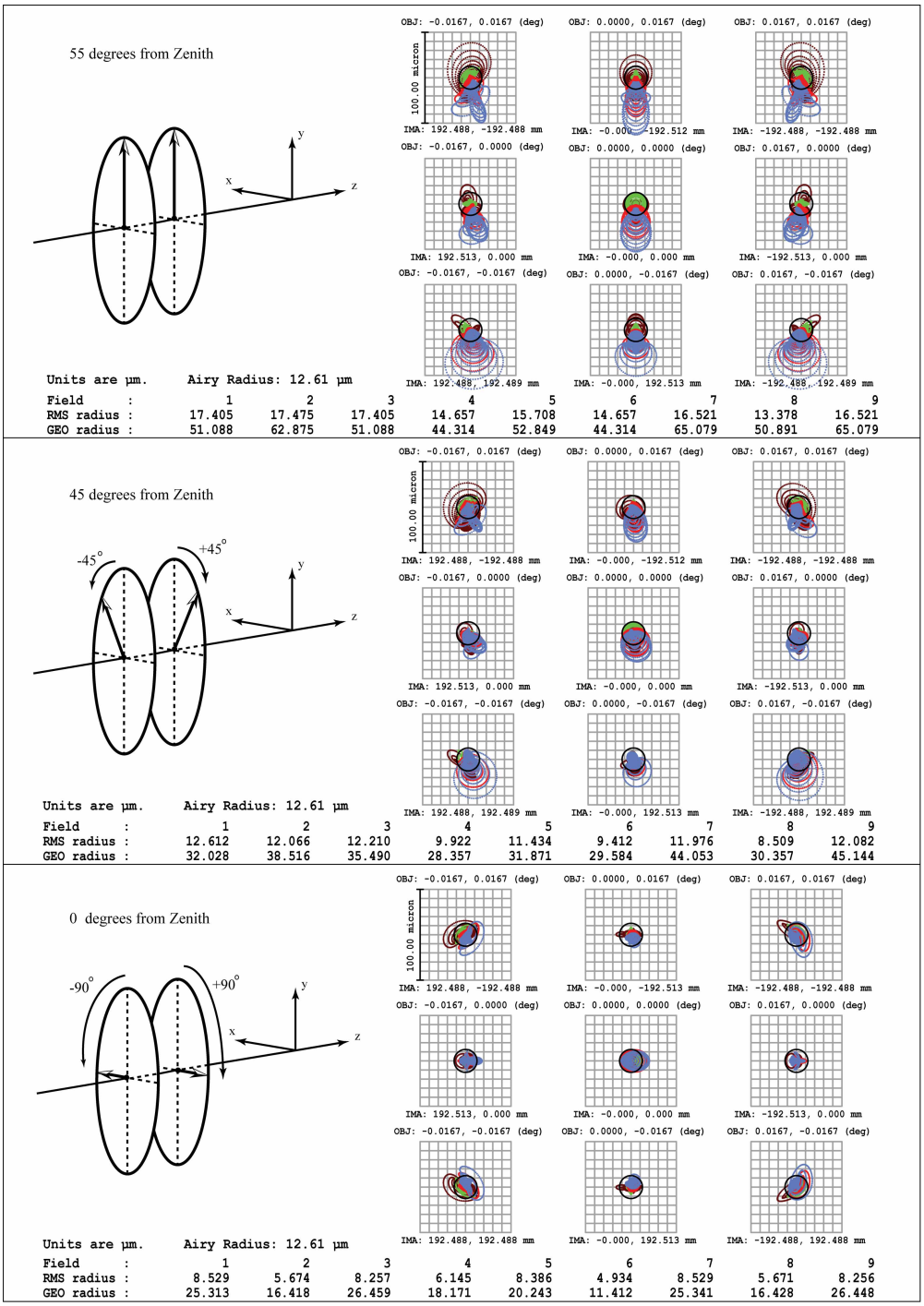

Fig. 8. The orientations of the counter-rotating lenses of the ADC for three different Zenith angles and corresponding spot diagrams over the 2-arcmin full field in the R band.

#145240 - $15.00 USD Received 1 Apr 2011; revised 7 Jul 2011; accepted 8 Aug 2011; published 17 Aug 2011

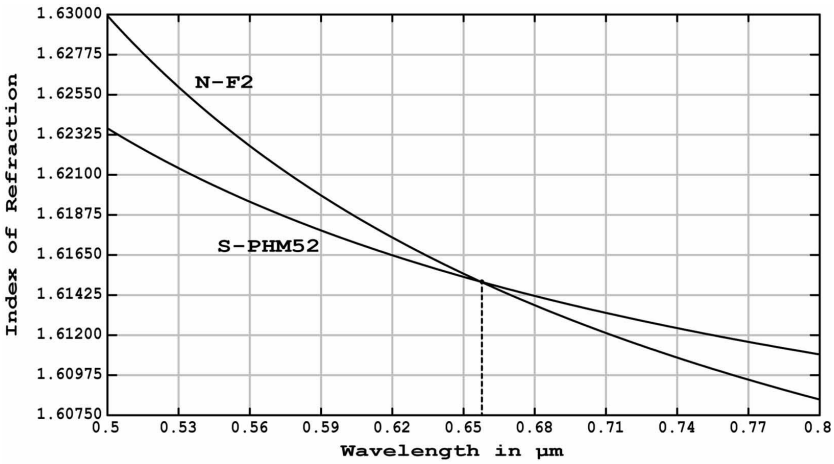

Fig. 9. The dispersion curves of N-F2 and S-PHM52 crossing at the prime wavelength, $\lambda = 0.657 \mu m$.

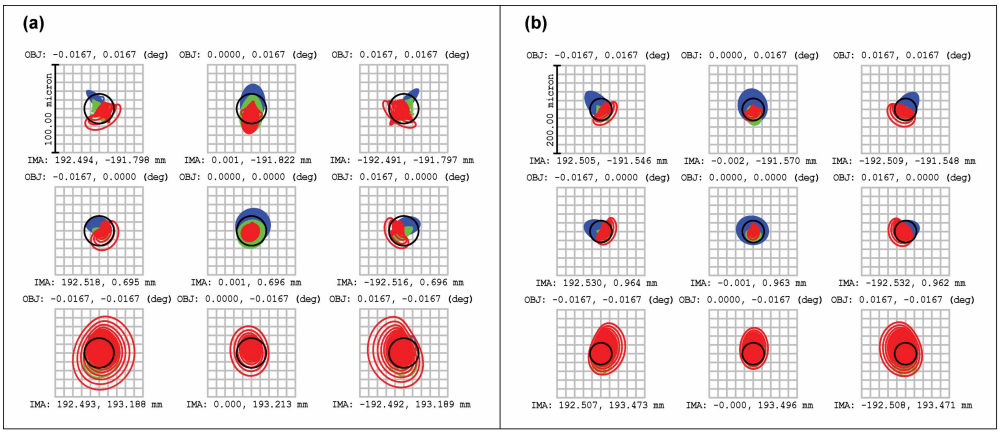

Fig. 10. Spot diagrams for the 2-arcmin full field of view of the E-ELT with the three-lens ADC in the I band (a) and J band (b).

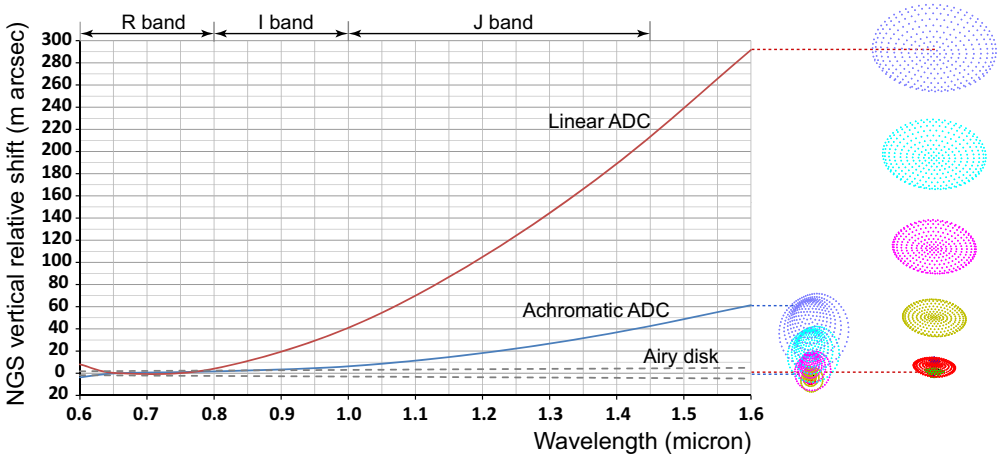

Fig. 11. NGS vertical displacement relative to the primary wavelength (0.657 μm) for the E-ELT operating in the R band at 45 deg off Zenith.

#145240 - $15.00 USD Received 1 Apr 2011; revised 7 Jul 2011; accepted 8 Aug 2011; published 17 Aug 2011

5. The optical design of the achromatic ADC

Table 2 presents the main optical parameters of the achromatic three-lens ADC. The flat surfaces have different angles of tilt. This ensures that the contribution of L1 and L2 to the atmospheric dispersion compensation is the same. That is why the counter-rotating lenses operate with identical angles of rotation (see Fig. 8).

Table 2. The Optical Prescription of the Achromatic Three-Lens ADC

Lens	Surface	Radius (mm)	Thickness (mm)	Glass	Diameter (mm)	Tilt X (deg)
L1	1	2936.233	6.000	S-PHM52	776.816	0
	2	infinity	40.000	N-F2	771.984	-2.35841
	3	-10563.000	251.760		761.624	0
L2	4	-3050.150	40.000	S-PHM52	662.076	0
	5	infinity	40.000	N-F2	655.660	-3.78378
	6	2455.459	349.361		642.116	0
L3	7	-2301.700	60.000	F5	608.329	0
	8	-1467.920			609.804	0

Now we shall analyze the aberration compensation in the original E-ELT system, the E-ELT with the ADC, and the ADC alone. Figure 12(a) shows that the intermediate focus of the telescope is highly aberrated. This is due to the fact that M1 and M2 only partly compensate spherical aberration and coma at F1. The main task of the telescope is to achieve anastigmatic correction at the final focus F2, which is possible with three powered aspheric mirrors. In a perfect focus, re-optimized L1 and L2 could do the job without using L3. However in the aberrated focus F1, the design of the ADC is more complicated and one needs L3 to achieve diffraction-limited correction.

In Fig. 12(b) the ADC takes part in the aberration balancing of the telescope. The ADC shows some positive spherical aberration and negative coma, which affect the outgoing beam. Due to this, M3 produces more negative spherical aberration and less positive coma in comparison to the original aberration balancing in the telescope. As a result, the overall image quality in the telescope is not degraded in the presence of the ADC.

Figure 12(c) specifies the main differences between the LADC and the three-lens ADC. Axial and lateral color introduced by L1 are corrected by L2, and L3 further removes the residual aberrations. Thus, the three-lens ADC corrects simultaneously atmospheric dispersion and its own chromatic aberrations.

6. Optical performance of an achromatic two-lens ADC

As mentioned in Section 5, in a perfect intermediate focus, the additional correction by L3 is not necessary. Figure 12(c) shows that L3 produces significantly less aberrations than L1 and L2. This motivates us to investigate optical performance of an achromatic two-lens ADC in the E-ELT.

After removing L3 and re-optimizing L1 and L2, there will be some noticeable amount of residual monochromatic aberrations in the final focus F2. To reduce the residual aberrations and achieve the comparable image quality as with the three-lens ADC, one could change the conic constants of M1 and M2: from -0.992726 to -0.988459 for M1 and from -2.307544 to -2.244125 for M2. This corresponds to less than 0.3 mm change in the mirror sag at the edge of the mirrors. In addition, one needs to add a small amount of defocus (less than what is required for the LADC).

Figure 13 shows that the two-lens ADC preserves the original image scale in spite of the modified shape of M1 and M2. The two-lens ADC is showing more intrinsic coma (Fig. 14).

#145240 - $15.00 USD Received 1 Apr 2011; revised 7 Jul 2011; accepted 8 Aug 2011; published 17 Aug 2011

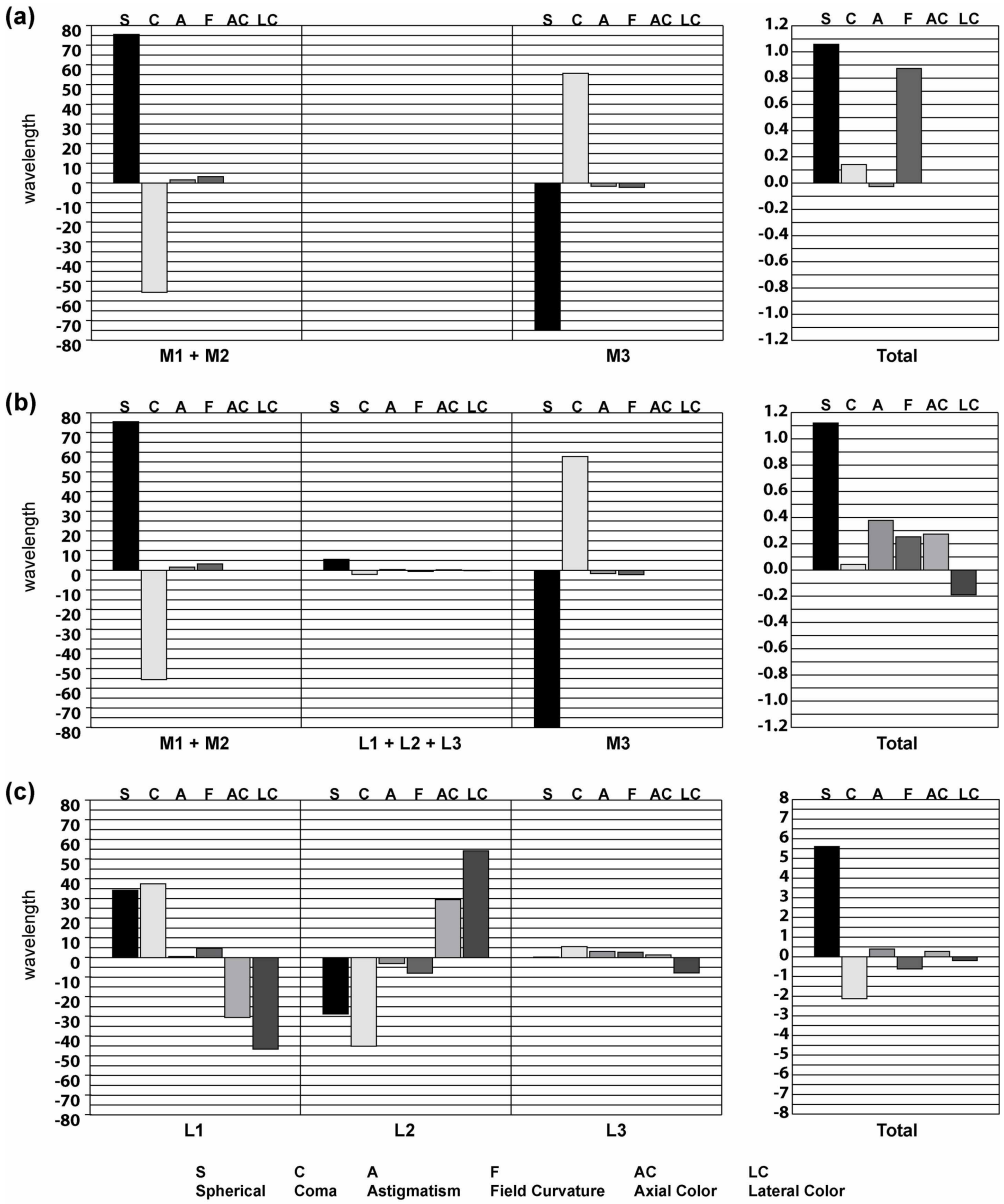

Fig. 12. Aberration diagrams for: (a) the E-ELT without the ADC, (b) E-ELT with the three-lens ADC, and (c) the three-lens ADC alone (The scales in the diagrams describing the total aberrations are different and the tilts of the surfaces are not considered.)

#145240 - $15.00 USD Received 1 Apr 2011; revised 7 Jul 2011; accepted 8 Aug 2011; published 17 Aug 2011

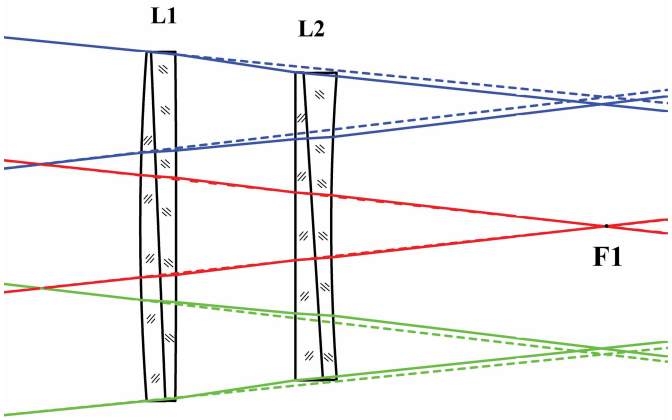

Fig. 13. The two-lens ADC and its effect on the path of the rays at F1. The dashed lines correspond to rays reflected from the modified M1 and M2 without *seeing* the ADC.

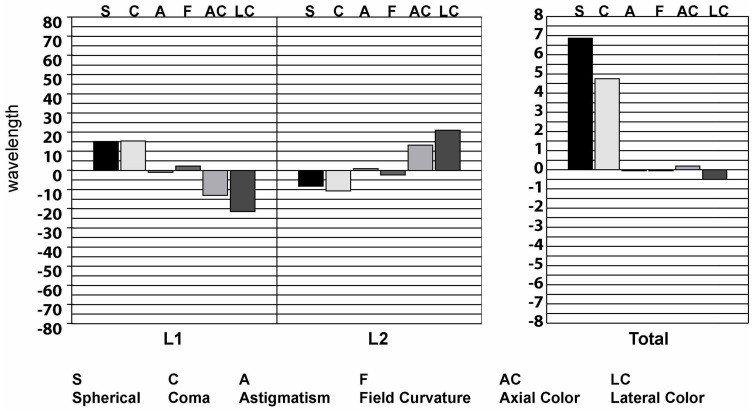

Fig. 14. The aberration diagrams for the two-lens ADC.

However, this coma is compensated by changing the conic constants on M1 and M2. Obviously, removing the ADC from the telescope will require reshaping of M1 and M2 to their original shape using active optics. Table 3 represents the optical prescription of the two-lens ADC; the optical diameters are given for 10-arcmin technical field.

Table 3. The Optical Prescription for the Achromatic Two-Lens ADC

Lens	Surface	Radius (mm)	Thickness (mm)	Glass	Diameter (mm)	Tilt X (deg)
L1	1	5348.556	40.000	S-PHM52	779.950	0
	2	infinity	40.000	N-F2	778.856	-2.35422
	3	-44629.100	266.060		768.432	0
L2	4	infinity	40.000	S-PHM52	687.640	0
	5	infinity	40.000	N-F2	685.574	-3.61044
	6	4665.763			706.472	0

The optical transmittance (OT) of the E-ELT with the achromatic two-lens ADC in the R, I, and J bands is presented in Table 4 for Zenith angle $Z = 0$ deg. For comparison we also give the OT of the E-ELT using a linear ADC in the R band (see Fig. 3). We assumed that each mirror surface has reflectance of 0.946, and we did not consider any special coatings for lens surfaces.

#145240 - $15.00 USD Received 1 Apr 2011; revised 7 Jul 2011; accepted 8 Aug 2011; published 17 Aug 2011

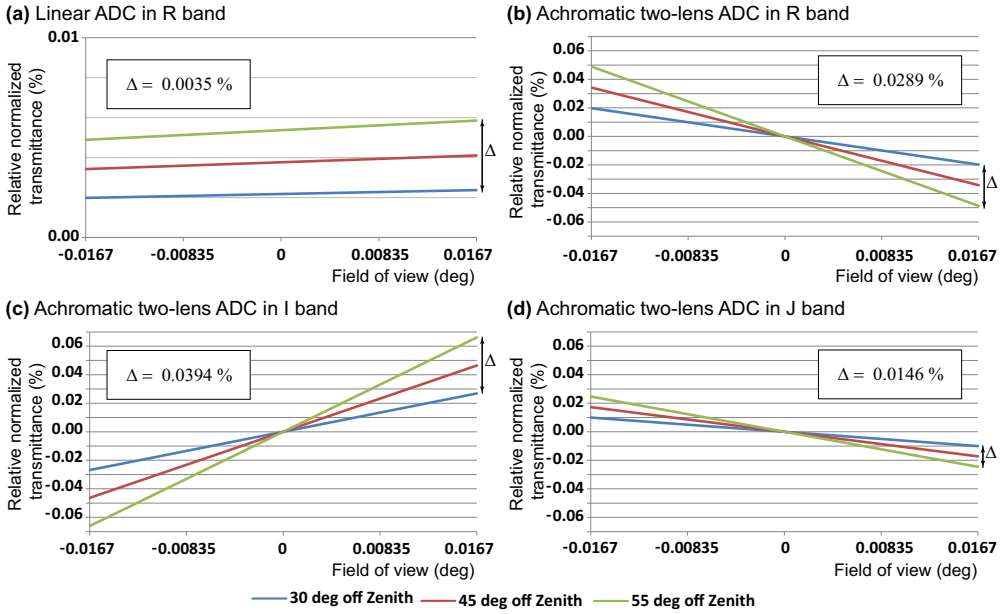

Fig. 15. Optical transmittance of the E-ELT (relative to the telescope transmittance at Zenith) as a function of field angle at different Zenith angles.

Figure 15 shows the relative normalized optical transmittance (OT^*) of the telescope at Zenith angles $Z = 30$, 45 and 55 deg, across the 2 arcmin full field in the vertical meridian. This is considered with respect to the optical transmittance of the telescope at Zenith ($Z = 0$ deg):

$$OT^*(Z) = \frac{OT(Z) - OT(0)}{OT(0)} \times 100\%, \tag{2}$$

As can be seen in Fig. 15, the OT of ADCs varies not only across the field, but also with Zenith

Table 4. Optical Transmittance of the E-ELT with the Linear and Achromatic ADC at Zenith

	-0.0167 (deg)	-0.0083 (deg)	0 (deg)	0.0083 (deg)	0.0167 (deg)
Linear ADC in R band	0.6940	0.6940	0.6940	0.6940	0.6940
Two-lens ADC in R band	0.6101	0.6102	0.6102	0.6102	0.6101
Two-lens ADC in I band	0.6113	0.6113	0.6113	0.6113	0.6113
Two-lens ADC in J band	0.5970	0.5971	0.5971	0.5971	0.5970

angle. For a given zenith angle the variation of the OT across the field can be calibrated during flat fielding. However, the OT variation with Zenith angle will alter the flat field by a small amount in the range of 0.01-0.04 % for a long exposure starting at $Z = 30$ deg and finishing at 55 deg. For shorter exposures this effect should not present any problems.

7. Conclusion

In spite of the simplicity of LADCs, their chromatic performance in fast foci may not be good enough for diffraction-limited imaging. Using other kinds of ADCs in fast foci, for example traditional RADCs, could be difficult. They usually have powered elements with noticeable amount of aberrations. Employing an LADC in the E-ELT shows unacceptable amount of chromatic aberrations, especially axial color, which due to the stringent optical constrains in

#145240 - $15.00 USD Received 1 Apr 2011; revised 7 Jul 2011; accepted 8 Aug 2011; published 17 Aug 2011

the E-ELT is not easily correctable by additional lens correctors. These constrains include the optical conjugation of M4, fixed beam geometry and minimal vignetting.

To resolve the problem of intrinsic chromatic aberrations we have designed an achromatic three-lens ADC for the E-ELT. The new ADC is intended for operation in the R, I, and J band up to 55 deg off Zenith providing near diffraction-limited image quality over 2 arcmin full filed. In addition to its exceptional optical performance, the ADC preserves the beam geometry, which keeps the optical configuration of the E-ELT unchanged. The proposed three-lens ADC has several advantages over an LADC. The main advantage is that the three-lens ADC gives superior optical performance at the R, I and J bands. The intrinsic aberrations of this ADC are so low that there is no need for any AO correction through the range of Zenith angles. It is two times more compact than a typical LADC. The three-lens ADC does not require any translation along the optical axis and also it does not introduce any vertical displacement of the image.

An LADC exceeds the performance of the three-lens ADC only in terms of the optical throughput and image quality of LGSs. To improve these two characteristics we have designed an achromatic two-lens ADC based on the same principle. The LGS image quality in the E-ELT with a two-lens ADC is comparable to that of an LADC case. The image quality for science objects observed at the R, I and J bands are about three times better in the E-ELT equipped with the two-lens ADC. However, such good optical performance is achievable if the conic constant of the primary and secondary mirror are slightly adjusted by active optics.

In the summary we would like to emphasize that the chromatic problems of using an LADC in the E-ELT is solved by replacing an LADC with one of the two ADC designs presented here. They provide diffraction-limited image quality up to 45 deg off Zenith and have several opto-mechanical advantages over an LADC. The achromatic ADC designs can operate in the final focus, yet their superior optical performance is more evident in fast foci.

Acknowledgments

The authors would like to thank Chris Dainty for his valuable comments and Kevin Thompson for helping us with the atmospheric dispersion modeling in the Code V optical design software.

This research was supported by Science Foundation Ireland under grant 07/IN.1/1906.

#145240 - $15.00 USD Received 1 Apr 2011; revised 7 Jul 2011; accepted 8 Aug 2011; published 17 Aug 2011

Paper III

Journal of Biomedical Optics 17(5), 055001 (May 2012)

Geometry-invariant gradient refractive index lens: analytical ray tracing

Mehdi Bahrami and Alexander V. Goncharov
National University of Ireland, Galway, School of Physics, Applied Optics Group, University Road, Galway, Ireland

Abstract. A new class of gradient refractive index (GRIN) lens is introduced and analyzed. The interior iso-indicial contours mimic the external shape of the lens, which leads to an invariant geometry of the GRIN structure. The lens model employs a conventional surface representation using a coincoid of revolution with a higher-order aspheric term. This model has a unique feature, namely, it allows analytical paraxial ray tracing. The height and the angle of an arbitrary incident ray can be found inside the lens in a closed-form expression, which is used to calculate the main optical characteristics of the lens, including the optical power and third-order monochromatic aberration coefficients. Moreover, due to strong coupling of the external surface shape to the GRIN structure, the proposed GRIN lens is well suited for studying accommodation mechanism in the eye. To show the power of the model, several examples are given emphasizing the usefulness of the analytical solution. The presented geometry-invariant GRIN lens can be used for modeling and reconstructing the crystalline lens of the human eye and other types of eyes featuring a GRIN lens. [DOI: 10.1117/1.JBO.17.5.055001]

Keywords: gradient index lens; crystalline lens; exact ray tracing; lens paradox.

Paper 11690 received Nov. 25, 2011; revised manuscript received Mar. 22, 2012; accepted for publication Mar. 22, 2012; published online May 7, 2012.

1 Introduction

Recent advances in new materials facilitate the application of gradient refractive index (GRIN) lenses in a variety of optical devices, especially in the development of bio-inspired lenses[1] and optical systems. Employing optical elements with a spatially variable index of refraction is a powerful way to achieve improved imaging. The best example of such a GRIN lens is the well-known Luneburg lens,[2] which is free from all monochromatic aberrations. The crystalline lens in the human eye is another example of a GRIN lens. In the present paper we explore a new mathematical model describing the crystalline GRIN lens. The gradual variation of the refractive index of the crystalline lens has been known for a long time and several models have been developed to account for the GRIN structure.[3–7] Advances in ocular aberration measurements,[8] magnetic resonance imaging,[9,10] optical tomography,[11] optical coherence tomography imaging,[12] and X-ray Talbot interferometry[13] have enabled researchers to improve existing eye models. Using this new data, several research groups have attempted to construct more realistic models of the GRIN lens. Navarro et al. proposed a GRIN lens model with concentric iso-indical contours mimicking the external conic surfaces of the lens.[14] The GRIN spatial distribution of this model follows the experimental age-dependent formula suggested in earlier work.[15] For the first time, a GRIN lens model features a curved equatorial plane, where anterior and posterior hemispheres meet. Using a different approach, Goncharov and Dainty introduced a wide-field schematic eye model with a GRIN lens, which uses a fourth-order polynomial describing the refractive structure of the lens.[16] Similar to the Navarro model, the external shape of the lens defines its GRIN structure. By estimating a parabolic path for the rays in the human GRIN lens[17] and using Sands' third-order aberrations study in inhomogeneous lenses,[18] this model presents approximated formulas for the power of the lens and its spherical aberration. Another recent model proposed by Díaz et al. uses a combination of polynomials and trigonometric functions for describing the refractive index distribution.[19] The coefficients of the refractive index of the lens are given as a linear function of age. Both models, Goncharov and Dainty and Díaz et al., are complete eye models providing age-dependent equations for the curvatures of the cornea and lens. Following the Navarro et al. model for the GRIN lens *in vitro*,[14] in a recent work by Castro et al., the power law of the GRIN lens profile has been modified to account for a possible toricity of the lens surface.[12] The variety of eye models featuring different GRIN profiles shows the great interest in lens structure and its effect on optical performance. In spite of the apparent progress made in this area, there is no simple GRIN lens model providing exact paraxial equations for the path of the rays inside the GRIN structure. It would be beneficial to have an analytical way to calculate the power and the third-order aberrations for the lens. Analytical solutions can help researchers gain a better understanding of the GRIN structure role in image formation and simplify the optical analysis of the lens. In addition, if such a model could also provide a more realistic (continuous) geometry of the GRIN lens's iso-indicial contours, it would become a valuable tool for reconstructing the human eye and modeling the accommodation mechanism. In the following section we introduce such a GRIN lens model and outline its main geometrical properties.

2 Parametric Model of the GRIN Lens

2.1 *Refractive Index Equation Based on Experimental Data*

There are many experimental studies focusing on the distribution of refractive index in the crystalline lens. In 1969 Nakao

Address all correspondence to: Mehdi Bahrami, National University of Ireland, Galway, School of Physics, Applied Optics Group, University Road, Galway, Ireland. Tel: +353 91 495350; Fax: +353 91 495529; E-mail: m.bahrami1@nuigalway.ie

0091-3286/2012/$25.00 © 2012 SPIE

et al. suggested a parabolic distribution for the refractive index in all directions:[20]

$$n(r) = c_0 + c_1 r^2, \tag{1}$$

where c_0 is the refractive index at the center of the lens, c_1 is the difference between the central index and the surface index, and r is a normalized distance from the lens center defining the geometry of the lens. Following this approach, Smith et al.[6] introduced more terms in Eq. (1) to get a better fit to experimental data.[21] Later, Smith et al.[15] proposed power-law to describe the distribution of refractive index along the optical axis as:

$$n(r) = c_0 + c_1 r^{2p}, \tag{2}$$

where the parameter p in the exponent is used to account for age-related changes in the GRIN lens. Equation (2) was used by Navarro et al. as a starting point for modeling GRIN lenses *in vitro*.[14] For clarity we rewrite Eq. (2) as

$$n(\zeta) = n_c + (n_s - n_c)(\zeta^2)^p, \tag{3}$$

where ζ is the normalized distance from the center of the lens, n_c and n_s are the refractive indices at the center and at the surface of the GRIN lens, respectively. Here, ζ changes between -1 to $+1$ to cover both anterior and posterior hemispheres of the lens; also we avoid introducing complex numbers by using the form $(\zeta^2)^p$.

2.2 *Geometry of Iso-Indicial Contours*

From the optical design point of view, it is convenient to describe the external surfaces of the GRIN lens as a conicoid of revolution:

$$z = \frac{c\rho^2}{1 + \sqrt{1 - (1+k)c^2\rho^2}}, \tag{4}$$

where c and k are respectively the curvature and the conic constant of the surface, and ρ is the distance from the optical z axis. There are other possible mathematical representations for the geometry GRIN lens, for example hyperbolic cosines[22] or Fourier series of cosines.[23] However these alternative representations do not have a straight forward connection with the radius of curvature and conic constant of the lens surface. On the other hand, using Eq. (4) greatly simplifies the parameterization of the surface. Following the idea of constructing the lens with conic surfaces on both sides,[14] one might get discontinuity of iso-indicial contours in equatorial interface joining two hemispheres. To avoid this problem, one could add an additional term on the right side of Eq. (4). Before we derive the continuity condition for iso-indicial contours at the equatorial interface, it is more convenient to rewrite Eq. (4) as a function of surface sag:

$$\rho^2 = 2rz - (1+k)z^2, \tag{5}$$

where r is the radius of curvature of the surface. Now introducing an additional term on the right side will help achieve the continuity condition. The surface equation becomes as:

$$\rho^2 = 2rz - (1+k)z^2 + bz^3, \tag{6}$$

where b is a constant, which is used to satisfy the continuity condition by making the first derivative $d\rho/dz = 0$ at the equatorial interface connecting the posterior and anterior hemispheres. Based on this approach, Eq. (7) represents our new description for the surface of iso-indical contours:

$$\rho_a^2 = 2r_a(t_a + z) - (1 + k_a)(t_a + z)^2 + b_a(t_a + z)^3, \quad -t_a \le z < 0 \tag{7a}$$

$$\rho_p^2 = 2r_p(t_p - z) - (1 + k_p)(t_p - z)^2 + b_p(t_p - z)^3, \quad 0 \le z \le t_p \tag{7b}$$

where subscripts a and p respectively stand for anterior and posterior parts of the lens, and t is the intercept of the iso-indicial contours measured from the origin O along the optical axis. Figure 1 depicts the continuous contours described by Eq. (7). With these recent techniques one could determine the intercept and the radius of curvature of the external surface, T and R, respectively. Iso-indical contours plots obtained by Jones et al. [9] show that the center of curvature of the inner contours gradually shifts toward the center O as a result of their steepening. This effect is more obvious in younger eyes, where central contours are still distinguishable. The simplest way to account for such a gradual change in curvature with depth is to define r as a linear function of the normalized distance from the center, $r = R\zeta$. It is worth noting that for both anterior and posterior hemispheres r, R, t, and T are numerically positive quantities; see Fig. 1.

By using Eq. (3), now we shall derive the continuity condition and find the corresponding refractive index for each iso-indicial contour. To satisfy the continuity condition we have to fulfill two constraints for an iso-indicial contour: zero derivative, $d\rho/dz = 0$, and equal heights, $\rho_a(z_c) = \rho_p(z_c)$, at the joining point z_c, as shown in Fig. 1. Using the first constraint, we determine b_a and b_p. As a result, for both hemispheres of the lens we have:

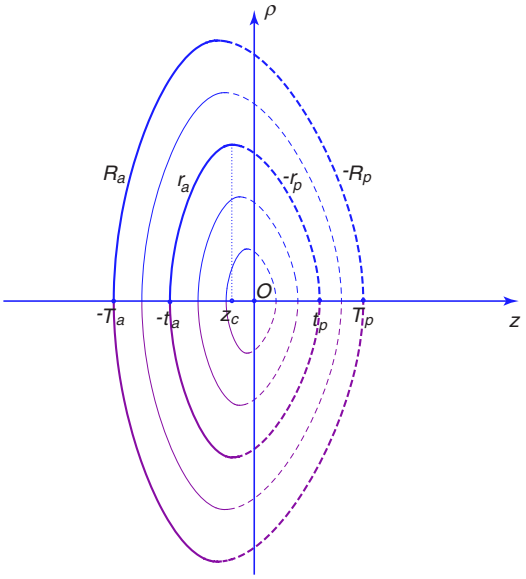

Fig. 1 Iso-indicial shells based on Eq. (7). Solid lines indicate the anterior part of the lens and the dashed lines specify the posterior part.

$$b_a = \frac{2}{3}\frac{(1+k_a)(t_a+z_c)-r_a}{(t_a+z_c)^2}, \tag{8a}$$

$$b_p = \frac{2}{3}\frac{(1+k_p)(t_p-z_c)-r_p}{(t_p-z_c)^2}. \tag{8b}$$

Using the second constraint we find the coordinate of the joining point as a function of the lens parameters r_a, r_p, k_a, k_p, t_a, and t_p:

$$z_c = \frac{2\eta}{-\mu-\sqrt{\mu^2-4\nu\eta}}, \tag{9}$$

where

$$\eta=\frac{1}{3}[-t_a^2(1+k_a)+4t_a r_a+t_p(-6r_p+t_p(1+k_p)(3+2r_p))],$$

$$\mu=\frac{2}{3}[-t_a(1+k_a)+2r_a+3r_p-t_p(1+k_p)(3-t_p(1+k_p)+r_p)],$$

$$\text{and } \nu=\frac{1}{3}[2-k_a+3k_p-2t_p(1+k_p)^2].$$

In the following sections we shall describe the optical properties of this GRIN lens model.

3 Thin Lens Approximation

The optical characteristics of a GRIN lens, such as the optical power and third-order aberrations, are usually not available in analytical form. However, in some cases (e.g., Ref. 24) and for our GRIN lens model it is possible to derive analytical expressions, which are given in Secs. 6 and 7. Although in Sec. 5 we discuss exact paraxial equations, it would be useful to start with a simplified power equation. The optical power of the GRIN lens can be described as the sum of the contributions from three components: the anterior surface of the lens, F_{as}; the GRIN structure of the lens, F_{GRIN}; and the posterior surface of the lens, F_{ps}. The optical power for the anterior and the posterior surfaces are given by a conventional equation[25]

$$F_s = \frac{n_2-n_1}{R}, \tag{10}$$

where n_1 and n_2 are respectively the refractive indices before and after the surface and R is the radius of curvature. To derive the expression for the optical power arising from the GRIN structure of the lens, we consider the GRIN lens structure as an infinite sum of thin homogeneous shells. Now by adding the power of all shells and considering that their thickness is negligibly small, we can obtain an approximate expression for the lens power. To do this, we rewrite Eq. (10) using the definition of derivative in a continuous medium

$$\delta F_{\text{GRIN}} = \frac{n'(\zeta)\delta\zeta}{R}. \tag{11}$$

Using Eq. (3) and taking the integral we find the optical power of the GRIN structure.

$$F_{\text{GRIN}} = \int_{-1}^{0}\frac{2p(n_s-n_c)(\zeta^2)^{p-\frac{1}{2}}}{-R_a\zeta}\mathrm{d}\zeta - \int_{0}^{1}\frac{2p(n_s-n_c)(\zeta^2)^{p-\frac{1}{2}}}{R_p\zeta}\mathrm{d}\zeta. \tag{12}$$

Experimental data suggest that for human eyes p is always larger than 2 (e.g., Ref. 14) and therefore Eq. (12) can be simplified to

$$F_{\text{GRIN}} = \frac{2p}{2p-1}(n_c-n_s)\left(\frac{1}{R_a}+\frac{1}{R_p}\right). \tag{13}$$

Finally, the total power of the lens is

$$F_{\text{thin}} = \frac{n_s-n_{\text{aqu}}}{R_a}+\frac{2p}{2p-1}(n_c-n_s)\left(\frac{1}{R_a}+\frac{1}{R_p}\right)+\frac{n_{\text{vit}}-n_s}{-R_p}, \tag{14}$$

where n_{aqu} and n_{vit} are respectively the refractive indices of the media before and after the lens.

4 Optical Path Length

One other useful characteristic of an optical element is its optical path length (OPL), defined as the product of the geometric length of the light path and the refractive index of the medium.[25] In a GRIN lens the refractive index gradually changes, then the OPL can be calculated as the sum of the small propagations in each infinitely thin iso-indicial shell. Since the paraxial thickness of these thin shells is simply $T_a d\zeta$ and $T_p d\zeta$ for anterior and posterior hemispheres, respectively, using Eq. (3) we can define the paraxial OPL of the presented GRIN model as

$$\text{OPL} = \int_{-1}^{0}(n_c+(n_s-n_c)(\zeta^2)^p)T_a\mathrm{d}\zeta + \int_{0}^{1}(n_c+(n_s-n_c)(\zeta^2)^p)T_p\mathrm{d}\zeta, \tag{15}$$

which results

$$\text{OPL} = (T_a+T_p)\frac{2n_c p+n_s}{2p+1}. \tag{16}$$

It is worth mentioning that the geometry of the iso-indicial contours is not contributing to the paraxial OPL of the lens, so Eq. (16) is applicable for any GRIN lens employing the paraxial refractive index distribution in Eq. (3) (e.g., the GRIN lens model proposed by Navarro et al.[14]).

5 Analytical Paraxial Ray Tracing

It is notoriously difficult to perform exact ray tracing through a GRIN lens, which is done numerically using optical design software. Even exact paraxial ray tracing equations are not available for GRIN lenses. One could also use an approximate method, where the ray path within the GRIN lens is assumed to be parabolic.[17] However, it would be desirable to have an exact method for paraxial ray tracing so that all optical characteristics of the lens can be found in closed form. Due to the linear dependence of the iso-indicial contours radius r on the normalized axial distance, $\zeta = z/T$, we are able to derive a closed-form solution for paraxial ray tracing in the geometry-invariant GRIN lens. Paraxial ray tracing is based on two main equations.[25] According to the first one we have

$$n_2u_2 = n_1u_1 - \frac{y_1}{R_1}(n_2-n_1), \tag{17}$$

where n_1 and n_2 are respectively the refractive indices before and after the interface surface, u_1 and u_2 are the angles of the incident and refracted rays, y_1 is the height of the ray at

the surface, and R_1 is the radius of the surface. For the next surface located at the axial distance d_2 from the first one, the height of the incident ray, y_2, is obtained by

$$y_2 = y_1 + d_2 u_2. \tag{18}$$

Following the same approach used to derive Eq. (11), we rewrite the axial thickness of the infinitely thin shells as $d_2 = \delta z$, then Eq. (18) becomes

$$u(z) = y'(z). \tag{19}$$

Using Eq. (3) and substituting the definition of the derivative from Eq. (19) into Eq. (17) results in

$$n\left(\frac{z+\delta z}{T}\right)\frac{y(z+2\delta z)-y(z+\delta z)}{\delta z} = n\left(\frac{z}{T}\right)\frac{y(z+\delta z)-y(z)}{\delta z}+\frac{y(z)}{R(z/T)}\left[n\left(\frac{z+\delta z}{T}\right)-n\left(\frac{z}{T}\right)\right]. \tag{20}$$

Finally considering u and y as continuous functions of z, we expand Eq. (20) around the origin for δz and keep only the first order terms, which gives us

$$\frac{y(z)n'(z/T)}{Rz}-\frac{n'(z/T)y'(z)}{T}-n(z/T)y''(z)=0. \tag{21}$$

Solving Eq. (21) for the anterior and posterior hemispheres (where T corresponds to T_a and T_p, respectively) leads to a general ray equation:

$$y(z)=\begin{cases} c_1 {}_2F_1\left[\frac{-1+2p-\alpha}{4p},\frac{-1+2p+\alpha}{4p};1-\frac{1}{2p};\frac{n_c-n_s}{n_c}\left(\frac{-z}{T_a}\right)^{2p}\right] \\ \quad + z\frac{c_2}{T_a}{}_2F_1\left[\frac{1+2p-\alpha}{4p},\frac{1+2p+\alpha}{4p};1+\frac{1}{2p};\frac{n_c-n_s}{n_c}\left(\frac{-z}{T_a}\right)^{2p}\right] & -T_a \le z < 0 \\ c_1 {}_2F_1\left[\frac{-1+2p-\beta}{4p},\frac{-1+2p+\beta}{4p};1-\frac{1}{2p};\frac{n_c-n_s}{n_c}\left(\frac{z}{T_p}\right)^{2p}\right] \\ \quad + z\frac{c_2}{T_a}{}_2F_1\left[\frac{1+2p-\beta}{4p},\frac{1+2p+\beta}{4p};1+\frac{1}{2p};\frac{n_c-n_s}{n_c}\left(\frac{z}{T_p}\right)^{2p}\right] & 0 \le z \le T_p, \end{cases} \tag{22}$$

where ${}_2F_1$ is Gaussian (ordinary) hypergeometric function and

$$\alpha = \sqrt{8T_a p/R_a + (1-2p)^2}$$

$$\beta = \sqrt{8T_p p/R_p + (1-2p)^2}$$

$$c_1 = -\frac{\mathcal{F}_2 T_a u_0 + y_0(\mathcal{F}_5 + \mathcal{F}_4\gamma_1)}{\mathcal{F}_2\mathcal{F}_3\gamma_2 - \mathcal{F}_1(\mathcal{F}_5+\mathcal{F}_4\gamma_1)}$$

$$c_2 = -\frac{y_0}{\mathcal{F}_2}+\frac{\mathcal{F}_1}{\mathcal{F}_2}c_1,$$

where u_0 and y_0 are respectively the angle and the height of the incident ray after refraction by the anterior surface of the lens and the expressions for $\mathcal{F}_i$ and γ_j are given in the appendix. Using Eqs. (19) and (22), the angle of the ray can be found as

$$u(z)=\begin{cases} \frac{c_1}{T_a}\gamma_2\left(\frac{-z}{T_a}\right)^{2p-1}{}_2F_1\left[\frac{-1+6p+\alpha}{4p},\frac{-1+6p-\alpha}{4p};2-\frac{1}{2p};\frac{n_c-n_s}{n_c}\left(\frac{-z}{T_a}\right)^{2p}\right] \\ \quad + \frac{c_2}{T_a}\gamma_1\left(\frac{-z}{T_a}\right)^{2p}{}_2F_1\left[\frac{1+6p-\alpha}{4p},\frac{1+6p+\alpha}{4p};2+\frac{1}{2p};\frac{n_c-n_s}{n_c}\left(\frac{-z}{T_a}\right)^{2p}\right] & -T_a \le z < 0 \\ \quad + \frac{c_2}{T_a}{}_2F_1\left[\frac{1+2p-\alpha}{4p},\frac{1+2p+\alpha}{4p};1+\frac{1}{2p};\frac{n_c-n_s}{n_c}\left(\frac{-z}{T_a}\right)^{2p}\right] \\ \frac{c_1}{T_p}\gamma_4\left(\frac{z}{T_p}\right)^{2p-1}{}_2F_1\left[\frac{-1+6p+\beta}{4p},\frac{-1+6p-\beta}{4p};2-\frac{1}{2p};\frac{n_c-n_s}{n_c}\left(\frac{z}{T_p}\right)^{2p}\right] \\ \quad + \frac{c_2}{T_a}\gamma_3\left(\frac{z}{T_p}\right)^{2p}{}_2F_1\left[\frac{1+6p-\beta}{4p},\frac{1+6p+\beta}{4p};2+\frac{1}{2p};\frac{n_c-n_s}{n_c}\left(\frac{z}{T_p}\right)^{2p}\right] & 0 \le z \le T_p. \\ \quad + \frac{c_2}{T_a}{}_2F_1\left[\frac{1+2p-\beta}{4p},\frac{1+2p+\beta}{4p};1+\frac{1}{2p};\frac{n_c-n_s}{n_c}\left(\frac{z}{T_p}\right)^{2p}\right] \end{cases} \tag{23}$$

Both the height $y(z)$ and the angle $u(z)$ of the ray are necessary to describe the optical properties of the GRIN lens, which is the main goal of Secs. 6 and 7.

It is worth mentioning that the tilt or decenter of the lens can be seen as a change in the angle and the height of the incident ray, respectively, and Eqs. (22) and (23) are still applicable.

6 Analytical Expression for Optical Power

In this section we present an analytical expression for the optical power of the GRIN lens derived with the help of Eqs. (22) and (23). First we consider the power of a homogeneous lens:[25]

$$F_L = \frac{(n_2 - n_1)}{R_1} - \frac{(n_2 - n_3)}{R_2} + d\frac{(n_2 - n_3)(n_2 - n_1)}{n_2 R_1 R_2}, \quad (24)$$

where n_1, n_2, and n_3 are respectively the refractive indices of the medium before the lens, within the lens, and the medium after the lens; d is the thickness of the lens, and R_1 and R_2 are respectively the radius of curvatures for the anterior and posterior surfaces. Equation (24) is derived from Eqs. (17) and (18). Using a similar approach, Eqs. (22) and (23) will give the optical power of the GRIN lens

$$F = A_a\frac{(n_s - n_{\text{aqu}})}{R_a} + A_{\text{GRIN}} - A_p\frac{(n_s - n_{\text{vit}})}{-R_p} + A_d\frac{(n_s - n_{\text{vit}})(n_s - n_{\text{aqu}})}{-n_s R_a R_p}, \quad (25)$$

where A_a, A_{GRIN}, A_p, and A_d are constants associated with the GRIN structure of the lens, the expressions of which are given in Appendix. For a simple lens, where $n_s = n_c$, it can be shown that $A_a = 1$, $A_{\text{GRIN}} = 0$, $A_p = 1$, and $A_d = T_a + T_p$, which reduces Eq. (25) to Eq. (24). On the other hand, by assuming t_a and t_p are small enough to be ignored, we get $A_a = 1$, $A_{\text{GRIN}} = F_{\text{GRIN}}$, $A_p = 1$, and $A_d = 0$, which simplifies Eq. (25) to Eq. (14).

Using Eq. (25), we can find the focal length, f, and the back focal length of the lens, f_{back} as

$$f = \frac{n_{\text{vit}}}{F}, \quad (26)$$

and

$$f_{\text{back}} = fB_f, \quad (27)$$

where B_f is defined in the Appendix.

We shall stress that the optical power of the lens is not affected by its tilt or decenter and remains one of the fundamental characteristics of the lens.

7 Third-Order Aberrations

In general, the contribution of a GRIN lens to Seidel aberrations can be divided in two parts. The first part is the surface contribution of the interface between the homogeneous medium and inhomogeneous (GRIN) medium. The second part is the transfer contribution originating inside the GRIN media. For a GRIN lens with iso-indicial contours being coincident with the external surfaces, the surface contribution can be calculated as a conventional contribution from an interface between homogeneous media. Therefore we shall start with a single surface contribution to the primary third-order monochromatic aberrations. The coefficient of third-order spherical aberration is given by[26]

$$S_{\text{I}} = -y\left[\left(\frac{u_2 - u_1}{1/n_2 - 1/n_1}\right)^2\left(\frac{u_2}{n_2} - \frac{u_1}{n_1}\right) + k\frac{(n_2u_2 - n_1u_1)^3}{(n_2 - n_1)^2}\right], \quad (28)$$

where y is the height of the marginal ray at the surface, u_1 and u_2 are respectively the incident and refracted rays angles relative to the optical axis, n_1 and n_2 are respectively the refractive indices before and after the surface, and k is the conic constant of the surface. Similar to our derivation of Eq. (20), from Eq. (28) we find the contribution of an infinitely thin layer within the GRIN structure as

$$\delta S_{\text{I}} = -y(z)\left\{\frac{Tn^2(\frac{z}{T})y''^2(z)[-n'(\frac{z}{T})y'(z) + Tn(\frac{z}{T})y''(z)]}{n'^2(\frac{z}{T})} + k\frac{[n'(\frac{z}{T})y'(z) + Tn(\frac{z}{T})y''(z)]^3}{Tn'^2(\frac{z}{T})}\right\}\delta z, \quad (29)$$

then by considering the contribution of the anterior and posterior surfaces and summing up all thin layer contributions of the GRIN structure we have

$$\sum S_{\text{I}} = -y_0\left[\left(\frac{u_0 - u_a}{1/n_s - 1/n_{\text{aqu}}}\right)^2\left(\frac{u_0}{n_s} - \frac{u_a}{n_{\text{aqu}}}\right) + k_a\frac{(n_su_0 - n_{\text{aqu}}u_a)^3}{(n_s - n_{\text{aqu}})^2}\right] + \int_{-T_a}^{T_p} \text{d}S_{\text{I}} - y(T_p)\left\{\left[\frac{u_p - u(T_p)}{1/n_{\text{vit}} - 1/n_s}\right]^2\left[\frac{u_p}{n_{\text{vit}}} - \frac{u(T_p)}{n_s}\right] + k_p\frac{[n_{\text{vit}}u_p - n_su(T_p)]^3}{(n_{\text{vit}} - n_s)^2}\right\}, \quad (30)$$

where u_a is the marginal ray angle at the anterior surface and $u(T_p)$ and u_p are the angles of the marginal ray immediately before and after the posterior surface, respectively. The latter can be derived using Eq. (17)

$$u_p = \frac{1}{n_{\text{vit}}}\left[n_su(T_p) + \frac{y(T_p)}{R_p}(n_{\text{vit}} - n_s)\right]. \quad (31)$$

In addition to the marginal ray we also need to trace the chief (principal) ray when calculating coefficients for off-axis aberrations. Using the chief and the marginal rays, the contribution of a single conic surface to the aberration coefficient of third-order coma could be written as[26]

$$S_{\text{II}} = -y\left[\left(\frac{u_2 - u_1}{1/n_2 - 1/n_1}\right)^2\left(\frac{u_2}{n_2} - \frac{u_1}{n_1}\right)\left(\frac{u_{c2} - u_{c1}}{u_2 - u_1}\right) + k(n_2u_{c2} - n_1u_{c1})\frac{(n_2u_2 - n_1u_1)^2}{(n_2 - n_1)^2}\right], \quad (32)$$

where u_{c1} and u_{c2} are respectively the angle of the incident and refracted chief ray. Note that the angles u_{c1} and u_{c2} are measured with respect to the optical axis.

Similar to our derivation of Eq. (29), we find the contribution to aberration coma from an infinitely thin layer of the GRIN structure:

$$\delta S_{\mathrm{II}} = -y(z)\left\{ y_c''(z)\frac{Tn(\frac{z}{T})^2 y''(z)[-n'(\frac{z}{T})y'(z)+Tn(\frac{z}{T})y''(z)]}{n'(\frac{z}{T})^2} + k\left[n'\left(\frac{z}{T}\right)y_c'(z)+Tn\left(\frac{z}{T}\right)y_c''(z)\right] \times\frac{[n'(\frac{z}{T})y'(z)+Tn(\frac{z}{T})y''(z)^2]}{Tn'(\frac{z}{T})^2}\right\}\delta z, \tag{33}$$

where y_c is the chief ray height defined by the general ray equation, Eq. (22), for which the input height at the anterior surface is $y_0 = 0$, since in the human eye the aperture stop (iris) approximately coincides with the front surface of the lens, and u_0 is the chief ray angle after the refraction from the anterior surface, $u_0 = u_{c0}$. These initial conditions are reflected in coefficients c_1 and c_2. Now using Eq. (23) we could also find the chief angle u_c within the GRIN lens. Finally by tracing both marginal and chief rays we get the total third-order coma coefficient of the GRIN lens:

$$\sum S_{\mathrm{II}} = -y_0\left[\left(\frac{u_0-u_a}{1/n_s-1/n_{\mathrm{aqu}}}\right)^2\left(\frac{u_0}{n_s}-\frac{u_a}{n_{\mathrm{aqu}}}\right)\left(\frac{u_{c0}-u_{ca}}{u_0-u_a}\right) + k_a(n_s u_{c0}-n_{\mathrm{aqu}}u_{ca})\frac{(n_s u_0-n_{\mathrm{aqu}}u_a)^2}{(n_s-n_{\mathrm{aqu}})^2}\right] + \int_{-T_a}^{T_p}\mathrm{d}S_{\mathrm{II}} - y(T_p)\left\{\left[\frac{u_p-u(T_p)}{1/n_{\mathrm{vit}}-1/n_s}\right]^2 \times\left[\frac{u_p}{n_{\mathrm{vit}}}-\frac{u(T_p)}{n_s}\right]\left[\frac{u_{cp}-u_c(T_p)}{u_a-u_a}\right] + k_p[n_{\mathrm{vit}}u_{cp}-n_s u_c(T_p)]\frac{[n_{\mathrm{vit}}u_p-n_s u(T_p)]^2}{(n_{\mathrm{vit}}-n_s)^2}\right\}, \tag{34}$$

where u_{cp} is the outgoing chief ray angle at the posterior surface, which could be calculated as u_p in Eq. (31), and u_{ca} is the angle of the incident chief ray on the anterior lens surface.

Following the same concept we can calculate aberration coefficients for third-order astigmatism, where the contribution of a single surface has the following form

$$S_{\mathrm{III}} = -y\left[\left(\frac{u_2-u_1}{1/n_2-1/n_1}\right)^2\left(\frac{u_2}{n_2}-\frac{u_1}{n_1}\right)\left(\frac{u_{c2}-u_{c1}}{u_2-u_1}\right)^2 + k(n_2u_{c2}-n_1u_{c1})^2\frac{(n_2u_2-n_1u_1)}{(n_2-n_1)^2}\right] \tag{35}$$

and the contribution of an infinitely thin layer is

$$\delta S_{\mathrm{III}} = -y(z)\left\{ y_c''(z)^2\frac{Tn(\frac{z}{T})^2 y''(z)[-n'(\frac{z}{T})y'(z)+Tn(\frac{z}{T})y''(z)]}{n'(\frac{z}{T})^2} + k[n'\left(\frac{z}{T}\right)y_c'(z)+Tn\left(\frac{z}{T}\right)y_c''(z)]^2 \times\frac{n'(\frac{z}{T})y'(z)+Tn(\frac{z}{T})y''(z)}{Tn'(\frac{z}{T})^2}\right\}\delta z, \tag{36}$$

and the total third-order astigmatism coefficient of the GRIN lens is

$$\sum S_{\mathrm{III}} = -y_0\left[\left(\frac{u_0-u_a}{1/n_s-1/n_{\mathrm{aqu}}}\right)^2\left(\frac{u_0}{n_s}-\frac{u_a}{n_{\mathrm{aqu}}}\right)\left(\frac{u_{c0}-u_{ca}}{u_0-u_a}\right)^2 + k_a(n_s u_{c0}-n_{\mathrm{aqu}}u_{ca})^2\frac{(n_s u_0-n_{\mathrm{aqu}}u_a)}{(n_s-n_{\mathrm{aqu}})^2}\right] + \int_{-T_a}^{T_p}\mathrm{d}S_{\mathrm{III}} - y(T_p)\left\{\left[\frac{u_p-u(T_p)}{1/n_{\mathrm{vit}}-1/n_s}\right]^2\left[\frac{u_p}{n_{\mathrm{vit}}}-\frac{u(T_p)}{n_s}\right] \times\left[\frac{u_{cp}-u_c(T_p)}{u_a-u_a}\right]^2 + k_p[n_{\mathrm{vit}}u_{cp}-n_s u_c(T_p)]^2 \times\frac{[n_{\mathrm{vit}}u_p-n_s u(T_p)]}{(n_{\mathrm{vit}}-n_s)^2}\right\}. \tag{37}$$

In a similar way, the field curvature of a single surface can be achievable as

$$S_{\mathrm{IV}} = -n_1(u_{c1}y-u_1y_c)^2\frac{n_2u_2-n_1u_1}{yn_2}, \tag{38}$$

where y_c is the height of the chief ray at the surface. Then for an infinitely thin layer we have

$$\delta S_{\mathrm{IV}} = -\frac{[-y_c(z)y'(z)+y(z)y_c'(z)]^2[n'(\frac{z}{T})y'(z)+Tn(\frac{z}{T})y''(z)]}{Ty(z)}\delta z, \tag{39}$$

and finally for the GRIN lens we have

$$\sum S_{\mathrm{IV}} = -n_{\mathrm{aqu}}y_0u_{ca}^2\frac{n_su_0-n_{\mathrm{aqu}}u_a}{n_s} + \int_{-T_a}^{T_p}\mathrm{d}S_{\mathrm{IV}} - n_s[u_c(T_p)y(T_p) - u(T_p)y_c(T_p)]^2\frac{n_{\mathrm{vit}}u_p-n_su(T_p)}{y(T_p)n_{\mathrm{vit}}}. \tag{40}$$

Despite the advantages of the Seidel theory, the third-order aberration calculations are limited to centered, rotationally symmetric systems, and do not support tilted or decentered elements, such as the crystalline lens in the eye. However, deriving the Seidel aberration coefficients of the GRIN lens in closed form is useful for understanding the nature of aberration compensation inside the GRIN structure. In addition to this, *in vitro* studies of the crystalline lens and its reconstruction based on the experimentally measured lenticular aberrations can benefit from the Seidel aberration representation.

It is worth mentioning that the capability of the geometry-invariant GRIN lens model is not limited to paraxial ray tracing and third-order aberration theory. In future work numerical ray tracing will be developed to calculate Zernike coefficients of the GRIN model lens, which can take the tilt and decenter of the lens into account.

8 Numerical Examples

We present an example of the eye model with the corneal and lenticular shape corresponding to a 40-year-old eye[16] with GRIN profile exponent $p = 3.13$ found in.[14] Figure 2 shows the main optical characteristics of the GRIN lens including the optical power, focal length, back focal length, as well as Seidel aberration coefficients; the lens geometry and GRIN structure parameters are given on the left side. Figure 2 actually

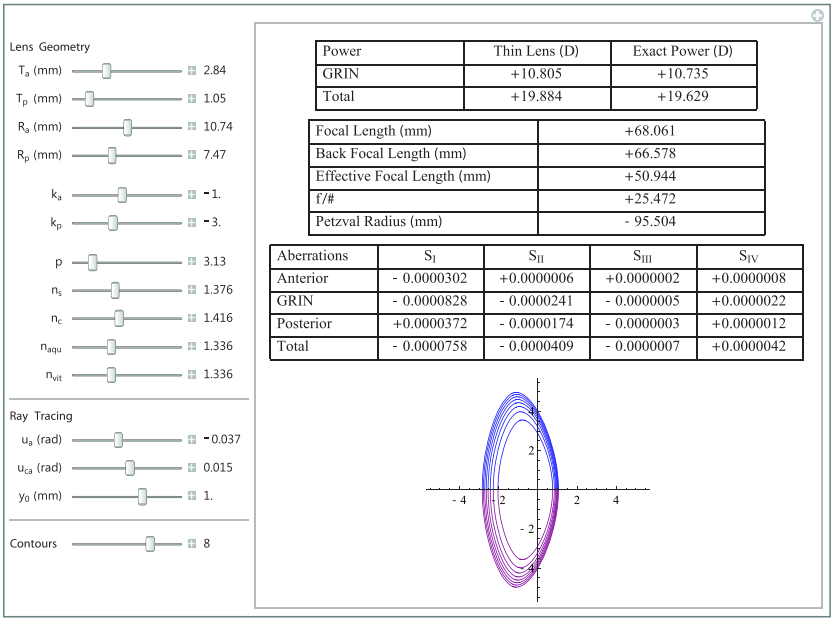

Fig. 2 Optical characteristics of a typical 40-year-old eye (each contour indicates 0.005 change in the refractive index). The image depicts the user interface for the open-source code available from the authors.[27]

depicts the user interface for the open-source code written by the authors, available at.[27] This code incorporates all mathematical expressions presented in this paper.

The optical power of the lens shown in Fig. 2 is based on the thin lens approximation in Eq. (14), and the exact power formula in Eq. (25). It is easy to see that the difference in optical power calculation is less than 1.4%, which indicates that Eq. (14) is useful especially if one wants to determine the exponent p for a given optical power. This can be done by solving Eq. (14) for p, which leads to

$$p = \frac{R_a n_{\text{vit}} + R_p(n_{\text{aqu}} + FR_a) - n_s(R_a + R_p)}{2[R_a n_{\text{vit}} + R_p(n_{\text{aqu}} + FR_a) - n_c(R_a + R_p)]}. \quad (41)$$

Knowing the external shape, measuring the optical power of the lens and the surface refractive index n_s, and assuming n_c is based on extensive experimental data, one could determine the GRIN profile exponent p for lenses *in vitro*. This approach provides a practical way to approximate the GRIN profile, which defines all optical characteristics of the lens.

The optical power of the crystalline lens and its age-related changes have been a controversial topic for decades. Many studies (e.g., Ref. 28) show that for an unaccommodated lens, its external surfaces become more curved and therefore more powerful with age. On the other hand, measurements of the total optical power of the eye suggest that the power does not change much with age.[29] This lens paradox might be explained, at least in part, by adjusting the center and surface refractive indices of the GRIN structure (n_c and n_s), the axial position of the peak in the refractive index profile (T_a or T_p), the lens axial thickness ($T_a + T_p$), and also the exponent p.[16,19,30–32] The latter parameter is the most challenging one to analyze, since calculating the contribution of the GRIN structure to the lens power has not been derived in an easily accessible form.

Pierscionek[32] suggested that a slight change in the slope of refractive index in the cortex might compensate the increase in lens curvature and prevent the eye from becoming myopic with age. Using Eq. (14) we can calculate the optical power change in the lens due to an age-related increase in the exponent p. Following a recent study[14] we select three age groups (20-, 40-, and 60-year-olds) with corresponding empirical value for p, see Table 1. To study the effect of p independently from other variables, such radii and central thickness, all three age groups have identical lens geometry. In Fig. 2 we can see that 1 D change in the optical power can be attributed to GRIN profile steepening alone.

It can be seen from Eq. (25) that one can easily adjust other parameters of the lens affecting the lens paradox and take into account their effect due to aging on the lens power. To adjust these parameters in a meaningful way, more experimental

Table 1 Three age groups (20-, 40-, and 60-year old) with corresponding empirical value for p and corresponding powers.

Age (year)	p	Thin lens power (D)	Exact power (D)
20	2.87	20.074	19.815
40	3.13	19.884	19.629
60	4.28	19.359	19.115

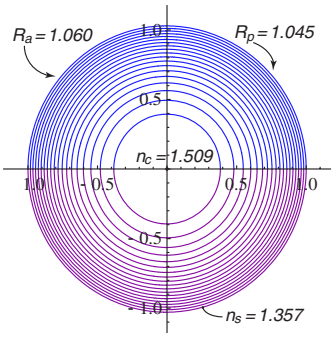

Fig. 3 The octopus eye model (each iso-indicial contour at 0.008 step in the refractive index).

data on the age-related changes in the GRIN structure is required.

The model presented here is not only useful for human eyes, it can also be beneficial for animal eye studies. For example, Fig. 3 shows the octopus eye model based on the experimental data provided by Jagger et al.,[33] where a strictly symmetrical lens was modeled. The original experimental data shows some departure from symmetry, which is taken into account in our model, presented in Fig. 3.

9 Conclusion

The characterization of GRIN lenses by ray-tracing is notoriously difficult and usually requires numerical methods, while only a handful of analytical solutions exist (e.g., Lundberg lens).

In light of this, we introduce and analyze a new class of GRIN lens, which has the following properties. The refractive index distribution is based on the power law defined by the exponent p, which can be adjusted in a continuous manner. The mathematical description of the external surfaces is a standard conicoid of revolution with a higher-order term. Iso-inditial contours feature smooth connection between the anterior and posterior hemispheres. Analytical paraxial ray tracing is possible, which provides expressions for all optical characteristics of the lens and its monochromatic aberrations. The description for aberration coefficients of a thin homogeneous layer is useful for a general GRIN lens description.

A few examples are presented to illustrate the advantage of this GRIN mode with special emphasis given to the thin lens approximation formula. The latter is very accurate, and can be used to analyze the role of exponent p in lens paradox. One could also determine the exponent p for a given optical power measured experimentally *in vitro*.

The interior iso-indicial contours mimic the external shape of the lens, which leads to invariant geometry of the GRIN structure. Due to this strong coupling between the external shape of the lens and its GRIN structure, one could study the changes in aberrations with accommodation. A dispersion model and chromatic aberrations of the lens will be derived in future work.

The new GRIN lens model can be used for other types of eyes, even for such an extreme case as the octopus eye. A user-friendly software incorporating all mathematical expressions is available from the authors.[27]

Appendix: Coefficient Definitions

$$\mathscr{F}_1 = {}_2F_1\left(\frac{-1+2p-\alpha}{4p}, \frac{-1+2p+\alpha}{4p}; 1-\frac{1}{2p}; \frac{n_c-n_s}{n_c}\right)$$

$$\mathscr{F}_2 = {}_2F_1\left(\frac{1+2p-\alpha}{4p}, \frac{1+2p+\alpha}{4p}; 1+\frac{1}{2p}; \frac{n_c-n_s}{n_c}\right)$$

$$\mathscr{F}_3 = {}_2F_1\left(\frac{-1+6p+\alpha}{4p}, \frac{-1+6p-\alpha}{4p}; 2-\frac{1}{2p}; \frac{n_c-n_s}{n_c}\right)$$

$$\mathscr{F}_4 = {}_2F_1\left(\frac{1+6p-\alpha}{4p}, \frac{1+6p+\alpha}{4p}; 2-\frac{1}{2p}; \frac{n_c-n_s}{n_c}\right)$$

$$\mathscr{F}_5 = {}_2F_1\left(\frac{1+2p-\alpha}{4p}, \frac{1+6p-\alpha}{4p}; 1+\frac{1}{2p}; \frac{n_c-n_s}{n_c}\right)$$

$$\mathscr{F}_6 = {}_2F_1\left(\frac{-1+6p+\beta}{4p}, \frac{1+6p-\beta}{4p}; 2-\frac{1}{2p}; \frac{n_c-n_s}{n_c}\right)$$

$$\mathscr{F}_7 = {}_2F_1\left(\frac{1+6p-\beta}{4p}, \frac{1+6p+\beta}{4p}; 2+\frac{1}{2p}; \frac{n_c-n_s}{n_c}\right)$$

$$\mathscr{F}_8 = {}_2F_1\left(\frac{1+2p-\beta}{4p}, \frac{1+2p+\beta}{4p}; 1+\frac{1}{2p}; \frac{n_c-n_s}{n_c}\right)$$

$$\mathscr{F}_9 = {}_2F_1\left(\frac{-1+2p+\beta}{4p}, \frac{-1+2p-\beta}{4p}; 1-\frac{1}{2p}; \frac{n_c-n_s}{n_c}\right)$$

$$\mathscr{F}_{10} = {}_2F_1\left(\frac{-1+2p-\beta}{4p}, \frac{-1+2p+\beta}{4p}; 1-\frac{1}{2p}; \frac{n_c-n_s}{n_c}\right)$$

$$\gamma_1 = \frac{n_c-n_s}{n_c}\frac{(1+2p)^2-\alpha^2}{8p+4}$$

$$\gamma_2 = \frac{n_c-n_s}{n_c}\frac{(1-2p)^2-\alpha^2}{8p-4}$$

$$\gamma_3 = \frac{n_c-n_s}{n_c}\frac{(1+2p)^2-\beta^2}{8p+4}$$

$$\gamma_4 = \frac{n_c-n_s}{n_c}\frac{(1-2p)^2-\beta^2}{8p-4}$$

$$A_{\mathrm{GRIN}} = \frac{n_s[\gamma_4 T_a(\gamma_1\mathscr{F}_4+\mathscr{F}_5)\mathscr{F}_6 + \gamma_2 T_p\mathscr{F}_3(\gamma_3\mathscr{F}_7+\mathscr{F}_8)]}{T_a T_p[\gamma_2\mathscr{F}_2\mathscr{F}_3 - \mathscr{F}_1(\gamma_1\mathscr{F}_4+\mathscr{F}_5)]}$$

$$A_a = \frac{\gamma_4 T_a\mathscr{F}_2\mathscr{F}_6 + T_p\mathscr{F}_1(\gamma_3\mathscr{F}_7+\mathscr{F}_8)}{T_p[\mathscr{F}_1(\gamma_1\mathscr{F}_4+\mathscr{F}_5) - \gamma_2\mathscr{F}_2\mathscr{F}_3]}$$

$$A_p = \frac{\gamma_2 T_p\mathscr{F}_3\mathscr{F}_8 + T_a(\gamma_1\mathscr{F}_4+\mathscr{F}_5)\mathscr{F}_9}{T_a[\mathscr{F}_1(\gamma_1\mathscr{F}_4+\mathscr{F}_5) - \gamma_2\mathscr{F}_2\mathscr{F}_3]}$$

$$A_d = \frac{T_p\mathscr{F}_1\mathscr{F}_8 + T_a\mathscr{F}_2\mathscr{F}_9}{(\mathscr{F}_1\gamma_1\mathscr{F}_4 + \mathscr{F}_5) - \gamma_2\mathscr{F}_2\mathscr{F}_3}$$

$$B_f = -\frac{T_a\mathscr{F}_{10}(\gamma_1\mathscr{F}_4 + \mathscr{F}_5) + \gamma_2 T_p\mathscr{F}_3\mathscr{F}_8}{T_a(\gamma_2\mathscr{F}_2\mathscr{F}_3 - \gamma_1\mathscr{F}_1\mathscr{F}_4 - \mathscr{F}_1\mathscr{F}_5)} + \frac{n_s - n_{\text{aqu}}}{n_s R_a}\frac{T_a\mathscr{F}_{10}\mathscr{F}_2 + T_p\mathscr{F}_1\mathscr{F}_8}{\gamma_2\mathscr{F}_2\mathscr{F}_3 - \gamma_1\mathscr{F}_1\mathscr{F}_4 - \mathscr{F}_1\mathscr{F}_5}$$

Acknowledgments

The authors would like to thank Chris Dainty for his valuable comments. This research was supported by Science Foundation Ireland under grant 07/IN.1/1906.

References

1. G. Beadie et al., "Optical properties of a bio-inspired gradient refractive index polymer lens," *Opt. Express* **16**(6), 11540–11547 (2008).
2. R. K. Luneburg, *Mathematical Theory of Optics* Brown University, Providence, RI (1944).
3. A. Gullstrand, *Hemholtz's Handbuch der Physiologischen Optik*, 3rd ed., English translation edited by J. P. Southall Ed., Optical Society of America, Vol. **1**, Appendix II, pp. 351–352 (1924).
4. J. W. Blaker, "Toward an adaptive model of the human eye," *J. Opt. Soc. Am. A* **70**(2), 220–223 (1980).
5. D. Y. C. Chan et al., "Determination and modeling of the 3-D gradient refractive indices in crystalline lenses," *Appl. Opt.* **27**(5), 926–931 (1988).
6. G. Smith, B. K. Pierscionek, and D. A. Atchison, "The optical modelling of the human lens," *Ophthalmic Physiol. Opt.* **11**(4), 359–369 (1991).
7. H. L. Liou and N. A. Brennan, "Anatomically accurate, finite model eye for optical modeling," *J. Opt. Soc. Am. A* **14**(8), 1684–1695 (1997).
8. J. Liang et al., "Objective measurement of wave aberrations of the human eye with the use of a hartmann-shack wave-front sensor," *J. Opt. Soc. Am. A* **11**(7), 1949–1957 (1994).
9. C. E. Jones et al., "Refractive index distribution and optical properties of the isolated human lens measured using magnetic resonance imaging (MRI)," *Vis. Res.* **45**(18), 2352–2366 (2005).
10. S. Kasthurirangan et al., "In vivo study of changes in refractive index distribution in the human crystalline lens with age and accommodation," *Invest. Ophthalmol. Vis. Sci.* **49**(6), 2531–2540 (2008).
11. D. Vazquez et al., "Tomographic method for measurement of the gradient refractive index of the crystalline lens. II. The rotationally symmetrical lens," *J. Opt. Soc. Am. A* **23**(10), 2551–2565 (2006).
12. A. de Castro et al., "Three-dimensional reconstruction of the crystalline lens gradient index distribution from OCT imaging," *Opt. Express* **18**(21), 21905–21917 (2010).
13. M. Hoshino et al., "Optical properties of in situ eye lenses measured with x-ray talbot interferometry: a novel measure of growth processes," *PLoS One* **6**(9), e25140 (2011).
14. R. Navarro, F. Palos, and L. González, "Adaptive model of the gradient index of the human lens. I. formulation and model of aging ex vivo lenses," *J. Opt. Soc. Am. A* **24**(8), 2175–2185 (2007).
15. G. Smith, D. A. Atchison, and B. K. Pierscionek, "Modeling the power of the aging human eye," *J. Opt. Soc. Am. A* **9**(12), 2111–2117 (1992).
16. A. V. Goncharov and C. Dainty, "Wide-field schematic eye models with gradient-index lens," *J. Opt. Soc. Am. A* **24**(8), 2157–2174 (2007).
17. G. Smith and D. Atchison, "Equivalent power of the crystalline lens of the human eye: comparison of methods of calculation," *J. Opt. Soc. Am. A* **14**(10), 2537–2546 (1997).
18. P. J. Sands, "Third-order aberrations of inhomogeneous lens," *J. Opt. Soc. Am. A* **60**(11), 1436–1443 (1970).
19. J. A. Díaz, C. Pizarro, and J. Arasa, "Single dispersive gradient-index profile for the aging human lens," *J. Opt. Soc. Am. A* **25**(1), 250–261 (2008).
20. S. Nakao et al., "Model of refractive indices in the human crystalline lens," *Jpn. J. Clin. Ophthalmol.* **23**, 903–906 (1969).
21. B. K. Pierscionek and D. Y. C. Chan, "Refractive index gradient of human lenses," *Optom. Vis. Sci.* **66**(12), 822–829 (1989).
22. H. T. Kasprzak, "New approximation for the whole profile of the human crystalline lens," *Ophthalmic Physiol.* **20**(1), 31–43 (2000).
23. R. Urs et al., "Age-dependent Fourier model of the shape of the isolated ex vivo human crystalline lens," *Vis. Res.* **50**(11), 1041–1047 (2010).
24. S. Dorić and N. Renaud, "Analytical expressions for the paraxial parameters of a single lens with a spherical distribution of refractive index," *Appl. Opt.* **31**(25), 5197–5200 (1992).
25. W. J. Smith, *Modern Optical Engineering* McGraw-Hill, New York (2000).
26. B. N. Begunov et al., *Optical Instrumentation: Theory and Design*. Mir, Moscow (1988).
27. The geometry-Invariant lens computational code. This is a computable document format (CDF) for the equations presented in the paper. Our source CDF code can be accessed via Mathematica, the computational software developed by Wolfram Research (Oct. 2011), http://optics.nuigalway.ie/people/mehdiB/CDF.html
28. N. Brown, "The change in lens curvature with age," *Exp. Eye Res.* **19**(2), 175–183 (1974).
29. H. Saunders, "A longitudinal study of the age-dependence of human ocular refraction I. Age-dependent changes in the equivalent sphere," *Ophthalmic Physiol. Opt.* **6**(1), 39–46 (1986).
30. R. P. Hemenger, L. F. Garner, and C. S. Ooi, "Changes with age of the refractive index gradient of the human ocular lens," *Invest. Ophthalmol. Vis. Sci.* **36**(3), 703–707 (1995).
31. G. Smith and B. K. Pierscionek, "The optical structure of the lens and its contribution to the refractive status of the eye," *Ophthalmic Physiol. Opt.* **18**(1), 21–29 (1998).
32. B. K. Pierscionek, "Presbyopia—effect of refractive index," *Clin. Exp. Optom.* **73**(1), 23–30 (1990).
33. W. S. Jagger and P. J. Standsl, "A wide-angle gradient index optical model of the crystalline lens and eye of the octopus," *Vis. Res.* **39**(17), 2841–2852 (1999).

Paper IV

Geometry-invariant GRIN lens: iso-dispersive contours

Mehdi Bahrami* **and Alexander V. Goncharov**
Applied Optics Group, National University of Ireland, Galway
Galway, Ireland
*m.bahrami1@nuigalway.ie

Abstract: A dispersive model of a gradient refractive index (GRIN) lens is introduced based on the idea of iso-dispersive contours. These contours have constant Abbe number and their shape is related to iso-indicial contours of the monochromatic geometry-invariant GRIN lens (GIGL) model. The chromatic GIGL model predicts the dispersion throughout the GRIN structure by using the dispersion curves of the surface and the center of the lens. The analytical approach for paraxial ray tracing and the monochromatic aberration calculations used in the GIGL model is employed here to derive closed-form expressions for the axial and lateral color coefficients of the lens. Expressions for equivalent refractive index and the equivalent Abbe number of the homogeneous equivalent lens are also presented and new aspects of the chromatic aberration change due to aging are discussed. The key derivations and explanations of the GRIN lens optical properties are accompanied with numerical examples for the human and animal eye GRIN lenses.

OCIS codes: (110.2760) Gradient-index lenses; (330.7326) Visual optics, modeling; (080.1005) Aberration expansions; (220.1000) Aberration compensation.

References and links

1. H. L. Liou and N. A. Brennan, "Anatomically accurate, finite model eye for optical modeling," J. Opt. Soc. Am. A **14,** 1684–1695 (1997).
2. J. A. Díaz, C. Pizarro, and J. Arasa, "Single dispersive gradient-index profile for the aging human lens," J. Opt. Soc. Am. A **25,** 250–261 (2008).
3. M. Bahrami and A. V. Goncharov, "Geometry-invariant GRIN lens: analytical ray tracing" J. Biomed. Opt. **17,** 055001 (2012).
4. B. K. Pierscionek, "Presbyopia - effect of refractive index," Clin. Exp. Optom. **73,** 23–30 (1990).
5. G. Smith, D. A. Atchison, and B. K. Pierscionek, "Modeling the power of the aging human eye," J. Opt. Soc. Am. A **9,** 2111–2117 (1992).
6. G. Smith and B. K. Pierscionek, "The optical structure of the lens and its contribution to the refractive status of the eye," Ophthalmic Physiol. Opt. **18,** 21–29 (1998).
7. C. E. Jones, D. A. Atchison, R. Meder, and J. M. Pope, "Refractive index distribution and optical properties of the isolated human lens measured using magnetic resonance imaging (MRI)," Vision Res. **45,** 2352–2366 (2005).
8. R. Navarro, F. Palos, and L. González, "Adaptive model of the gradient index of the human lens. I. formulation and model of aging ex vivo lenses," J. Opt. Soc. Am. A **24,** 2175–2185 (2007).
9. S. Kasthurirangan, E. L. Markwell, D. A. Atchison, and J. M. Pope, "In vivo study of changes in refractive index distribution in the human crystalline lens with age and accommodation," Invest. Ophthalmol. Vis. Sci. **49,** 2531–2540 (2008).
10. D. A. Palmer and J. Sivak, "Crystalline lens dispersion," J. Opt. Soc. Am. A **71,** 780–782 (1981).
11. J. G. Sivak and T. Mandelman, "Chromatic dispersion of the ocular media," Vision Res. **22,** 997–1003 (1982).
12. D. A. Atchison and G. Smith, "Chromatic dispersions of the ocular media of human eyes," J. Opt. Soc. Am. A **22,** 29–37 (2005).

#168414 - $15.00 USD Received 10 May 2012; revised 13 Jun 2012; accepted 13 Jun 2012; published 22 Jun 2012

13. The geometry-Invariant lens computational code. This is a computable document format (CDF) for the equations presented in Ref. [3]. Our source CDF code can be accessed via Mathematica, the computational software developed by Wolfram Research (Oct. 2011), *http://optics.nuigalway.ie/people/mehdiB/CDF.html*.
14. M. J. Kidger, *Fundamental Optical Design* (SPIE Press, 2002).
15. B. Gilmartin and R. E. Hogan, "The magnitude of longitudinal chromatic aberration of the human eye between 458 and 633 nm," Vision Res. **25,** 1747–1755 (1985).
16. R. I. Barraquer, R. Michael, R. Abreu, J. Lamarca, and F. Tresserra, "Human lens capsule thickness as a function of age and location along the sagittal lens perimeter," Invest. Ophthalmol. Vis. Sci. **47,** 2053–2060 (2006).
17. Y. Le Grand, *Form and Space Vision*, rev. ed., translated by M. Millodot and G. Heath (Indiana University Press, 1967).
18. R. Navarro, J. Santamaría, and J. Bescós, "Accommodation dependent model of the human eye with aspherics," J. Opt. Soc. Am. A **2,** 1273–1281 (1985).
19. S. R. Uhlhorn, D. Borja, F. Manns, and J. M. Parel, "Refractive index measurement of the isolated crystalline lens using optical coherence tomography," Vision Res. **48,** 2732–2738 (2008).
20. C. Ware, "Human axial chromatic aberration found not to decline with age," A. Graefes Arch. Klin. Exp. Ophthalmol. **218,** 39–41 (1982).
21. P. A. Howarth, X. X. Zhang, D. L. Still, and L. N. Thibos, "Does the chromatic aberration of the eye vary with age?," J. Opt. Soc. Am. A **5,** 2087–2096 (1988).
22. M. Millodot, "The influence of age on the chromatic aberration of the eye," A. Graefes Arch. Klin. Exp. Ophthalmol. **198,** 235–243 (1976).
23. J. A. Mordi and W. K. Adrian, "Influence of age on chromatic aberration of the human eye," A. Graefes Arch. Klin. Exp. Ophthalmol. **198,** 235–243 (1976).
24. N. Brown, "The change in lens curvature with age," Exp. Eye Res. **19,** 175–183 (1974).
25. A. V. Goncharov and C. Dainty, "Wide-field schematic eye models with gradient-index lens," J. Opt. Soc. Am. A **24,** 2157–2174 (2007).
26. R. H. H. Kröger and M. C. W. Campbell, "Dispersion and longitudinal chromatic aberration of the crystalline lens of the African cichlid fish Haplochromis burtoni," J. Opt. Soc. Am. A **13,** 2341–2347 (1996).
27. W. S. Jagger and P. J. Standsl, "A wide-angle gradient index optical model of the crystalline lens and eye of the octopus," Vision Res. **39,** 2841–2852 (1999).

1. Introduction

The experimental studies have shown a spatial change in chromatic dispersion of the gradient index (GRIN) eye lens. In spite of a noticeable variety in human GRIN lens models, modeling the dispersion of the GRIN lens has been considered only in two studies, [1] and [2]. However, the existing chromatic models of the GRIN lens do not have enough flexibility to be consistent with the experimental data that shows different amount of dispersion at the surface and the center of the GRIN lens. To understand the origin of chromatic effects in the GRIN lens and the corresponding aberrations arising from the spatial change of dispersion within the lens, one should consider the chromatic contribution of different layers in the GRIN structure. For doing this, we need at least to develop a paraxial ray tracing method (preferably analytical) for predicting the ray path within GRIN structure at different wavelengths. The paraxial ray-tracing will be the basis for calculating chromatic aberration of the GRIN structure, provided that the dispersion model for the surface and the center of the GRIN lens is given by experimental measurements.

In this paper we employ the geometry-invariant GRIN lens (GIGL) monochromatic model [3] and introduce wavelength dependence of the refractive index. This allows us to obtain a chromatic model matching experimental data on dispersion of the GRIN lens as well as to retain all properties of the GIGL mode including the analytical description for paraxial ray-tracing. Figure 1 depicts the GIGL geometry and its interior geometry-invariant iso-indicial contours, where R is the external radius of curvature and k is the external conic constant of the lens surfaces and subscripts 'a' and 'p' designate the anterior and the posterior surfaces, respectively, so that T_a and T_p are the axial thicknesses of the anterior and the posterior hemispheres, respectively. The sign convention used here is such that the radii and thicknesses are considered to be always positive as in our previous work [3]; however to be consistent with the

#168414 - $15.00 USD Received 10 May 2012; revised 13 Jun 2012; accepted 13 Jun 2012; published 22 Jun 2012

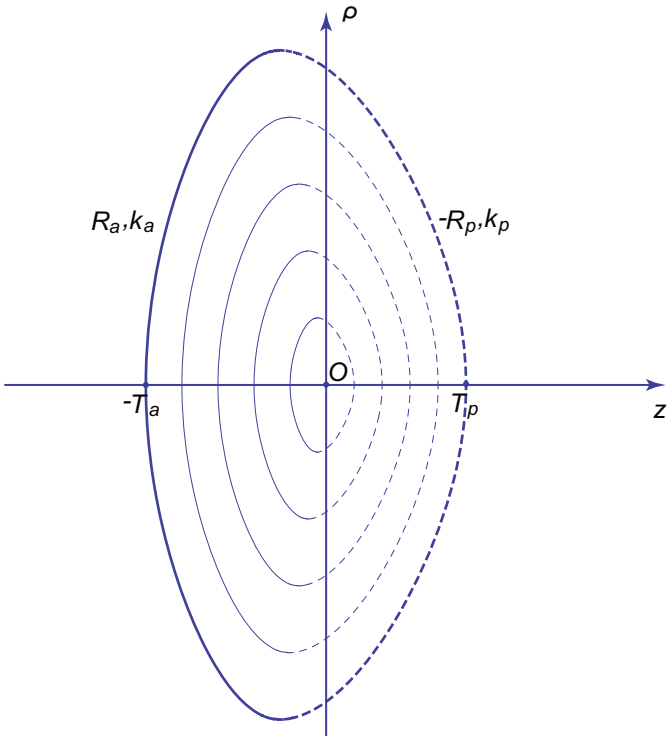

Fig. 1. The invariant-geometry GRIN lens and its interior iso-indicial contours [3].

optical design sign convention, we introduce '$-$' in front of T_a and R_p.

2. Dispersion model

2.1. Characteristics of dispersive GRIN lens

In the geometry-invariant GRIN lens model, the refractive index distribution is based on the power law profile, which was originally proposed by Pierscionek [4] and later supported by several studies [5–9]. In the GIGL model [3], this GRIN profile is presented as:

$$n(\zeta) = n_c + (n_s - n_c)(\zeta^2)^p; \tag{1}$$

where the parameter p in the exponent is employed to account for age-related dependence of the GRIN lens, ζ is the normalized distance from the center of the lens, and n_c and n_s are the refractive indices at the center and at the surface of the GRIN lens, respectively. Here, ζ varies between -1 to $+1$ to cover both anterior and posterior hemispheres of the lens. Note that the exponent p is not limited to integer numbers, so to avoid complex numbers we use the form $(\zeta^2)^p$. In monochromatic aberration studies, n_c and n_s are measured at a certain wavelength (typically at $\lambda_m = 555$ nm) for which the eye shows its highest sensitivity. It is well known that the GRIN lens is a dispersive medium with different dispersion characteristics at the center and at the surface [10, 11]. In other words, the GRIN refractive index profile is different at different wavelengths along the Z axis. We assume that these axial GRIN distribution profiles follow the power law with their own wavelength specific $n_c(\lambda)$, $n_s(\lambda)$ and $p(\lambda)$. In view of the well-known concept of iso-indicial contours in the GRIN lens, we propose the idea of iso-dispersive contours. We consider the lens structure consisting of very thin shells whit a constant chromatic dispersion (constant Abbe number). An iso-dispersive contour is the interface between the two adjacent shells.

#168414 - $15.00 USD Received 10 May 2012; revised 13 Jun 2012; accepted 13 Jun 2012; published 22 Jun 2012

There are several papers on suggesting theoretically sound equations for chromatic dispersion. Atchison *et al.* [12] have studied and reviewed experimental and theoretical data on ocular media dispersion and found the Cauchy's equation as the best fit:

$$n(\lambda) = A + \frac{B}{\lambda^2} + \frac{C}{\lambda^4} + \frac{D}{\lambda^6} + \ldots. \tag{2}$$

We use a modified representation of the Cauchy's equation as

$$n(\lambda) = n_m + n_{\lambda 2}\left(\frac{1}{\lambda^2} - \frac{1}{\lambda_m^2}\right) + n_{\lambda 4}\left(\frac{1}{\lambda^4} - \frac{1}{\lambda_m^4}\right), \tag{3}$$

where λ_m is the main wavelength and n_m is the refractive index at λ_m. n_m, $n_{\lambda 2}$ and $n_{\lambda 4}$ could be found by fitting Eq. (3) to a given dispersion data. Considering the experimental error in one of the dispersion measurements (Ref. [10]) used in the present paper, having only three terms in Eq. (3) provides an acceptable fit. In our experience, employing higher terms of Cauchy's equation gives the fitted curve a freedom to follow the noise in the data and even to develop a minimum, which does not correspond to a theoretically valid dispersion function.

Equation (1) can be rewritten to describe a dispersive GRIN medium as

$$n(\zeta, \lambda) = n_{center}(\lambda) + \left(n_{surface}(\lambda) - n_{center}(\lambda)\right)(\zeta^2)^{p(\lambda)}, \tag{4}$$

where

$$n_{center}(\lambda) = n_c + n_{c\lambda 2}\left(\frac{1}{\lambda^2} - \frac{1}{\lambda_m^2}\right) + n_{c\lambda 4}\left(\frac{1}{\lambda^4} - \frac{1}{\lambda_m^4}\right), \tag{5}$$

and

$$n_{surface}(\lambda) = n_s + n_{s\lambda 2}\left(\frac{1}{\lambda^2} - \frac{1}{\lambda_m^2}\right) + n_{s\lambda 4}\left(\frac{1}{\lambda^4} - \frac{1}{\lambda_m^4}\right). \tag{6}$$

n_c and n_s are respectively the refractive indices at the center and at the surface of the GRIN lens at the main wavelength λ_m, since Eq. (4) would be reduced to Eq. (1) where $\lambda = \lambda_m$. Therefore any characteristic of the lens (*e.g.* the optical power equations and the third-order aberration representations) defined for the monochromatic GIGL model [3, 13] will remain unchanged when using this representation.

To our knowledge this is the first attempt to represent the dispersive nature of the GRIN lens structure in terms of wavelength-dependent $n_{center}(\lambda)$, $n_{surface}(\lambda)$, and $p(\lambda)$. In the following section we show two numerical examples that emphasize the advantage of using this model when experimental dispersion data for the center and the surface of the lens is available.

2.2. Numerical examples

Equation (4) describes the gradual change in dispersion from the surface to the center of the lens. There are not so many published experimental data on the spatial change in dispersion of the GRIN lens in the human. These available data are limited to the dispersion curves at the center and the surface of the lens. This does not provide enough information to determine the rate of change in GRIN profile at any specific wavelength, which corresponds to the exponent $p(\lambda)$. Due to the lack of experimental data on wavelength dependence of the exponent $p(\lambda)$, for now, we limit our examples to the case of constant p. However the presented model is capable of taking into account the wavelength dependence of $p(\lambda)$ when more complete data become available. In the following, two sets of data are used to determine all the coefficients in the dispersive GRIN structure given by Eq. (4).

Palmer and Sivak [10] have done a series of measurements on a 70 year old eye for the wavelength range from 410 nm to 680 nm. It is worth mentioning that Palmer and Sivak have

#168414 - $15.00 USD Received 10 May 2012; revised 13 Jun 2012; accepted 13 Jun 2012; published 22 Jun 2012

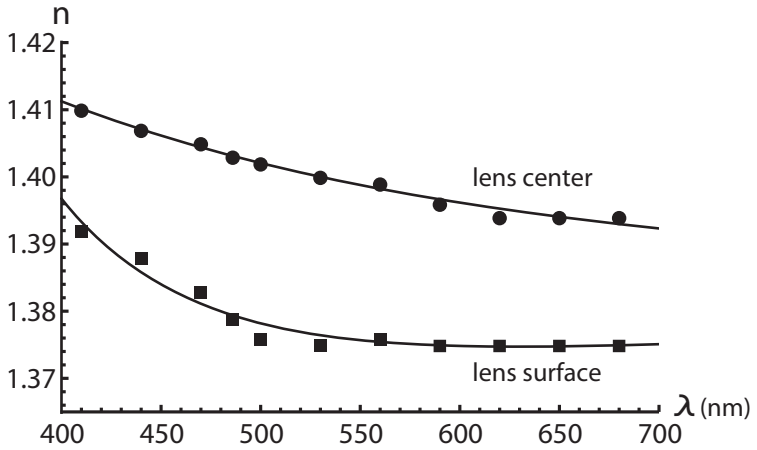

Fig. 2. The fit of the dispersion curves at the center and the surface of the lens to the dispersion data from Palmer and Sivak for a 70 year old eye [10].

stated that the material of the lens has not been altogether homogeneous and there have been inclusions of lower refractive index. Due to this, their data may not be as reliable as other data from human lenses. Figure 2 depicts their data and the least square fit using Eqs. (5) and (6). The fitting equations are

$$n_{center}(\lambda) = 1.39879 + 6241.59\left(\frac{1}{\lambda^2} - \frac{1}{555^2}\right) - 2.10368 \times 10^8\left(\frac{1}{\lambda^4} - \frac{1}{555^4}\right), \quad (7)$$

and

$$n_{surface}(\lambda) = 1.37555 - 7994.17\left(\frac{1}{\lambda^2} - \frac{1}{555^2}\right) + 1.58549 \times 10^9\left(\frac{1}{\lambda^4} - \frac{1}{555^4}\right). \quad (8)$$

In another work, Sivak and Mandelman [11] measured the GRIN lens dispersion of several subjects from 16-year old to 78-year old. They have provided averaged data for the dispersion curves of the center and the surface of the lens. Figure 3 shows the dispersion curves from the least square fit using Eqs. (5) and (6) to Sivak and Mandelman's data averaged over 6 to 9 separate eyes given by

$$n_{center}(\lambda) = 1.40395 + 7256.06\left(\frac{1}{\lambda^2} - \frac{1}{555^2}\right) - 1.54846 \times 10^8\left(\frac{1}{\lambda^4} - \frac{1}{555^4}\right), \quad (9)$$

and

$$n_{surface}(\lambda) = 1.37763 + 9260.03\left(\frac{1}{\lambda^2} - \frac{1}{555^2}\right) - 3.12554 \times 10^8\left(\frac{1}{\lambda^4} - \frac{1}{555^4}\right). \quad (10)$$

In addition to this, Fig. 4 demonstrates the dispersion curves across the lens provided by Eq. (4) for p equal to 2.0 and 5.0. This range is chosen in relation to the fitting results by Navarro *et al.* [8], where the case $p = 2.0$ could be considered as an extreme minimum for the refractive index profile of a very young healthy eye, whereas $p = 5.0$ corresponds to an aged eye. The intermediate curves between the lens center and surface show internal dispersion of the lens material predicted by Eq. (4) for ζ equal to 0.1, 0.2, ..., 0.9. The spacing between these curves indicates the power profile of the GRIN structure (characterized by exponent p).

Another way of distinguishing two cases ($p = 2.0$ and $p = 5.0$) is examining the refractive index profiles along the lens optical axis; these profiles are shown in Fig. 5. Figure 5 illustrates an age-related alteration originally suggested by Pierscionek [4] in the *lens paradox* explanation.

#168414 - $15.00 USD Received 10 May 2012; revised 13 Jun 2012; accepted 13 Jun 2012; published 22 Jun 2012

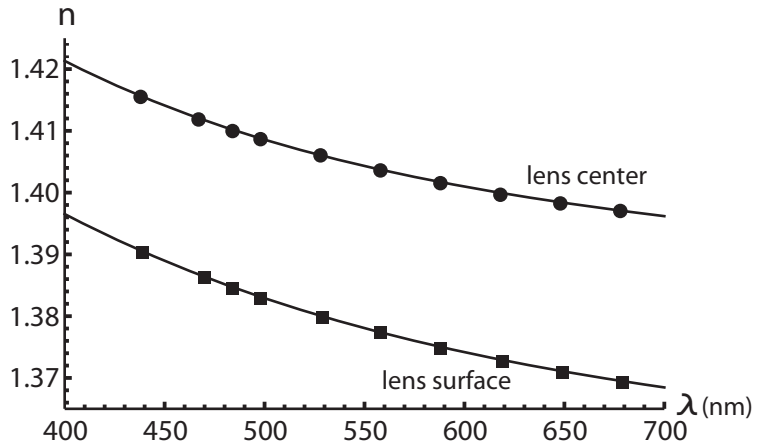

Fig. 3. The fit of the dispersion curves at the center and the surface of the lens to the dispersion data from Sivak and Mandelman [11].

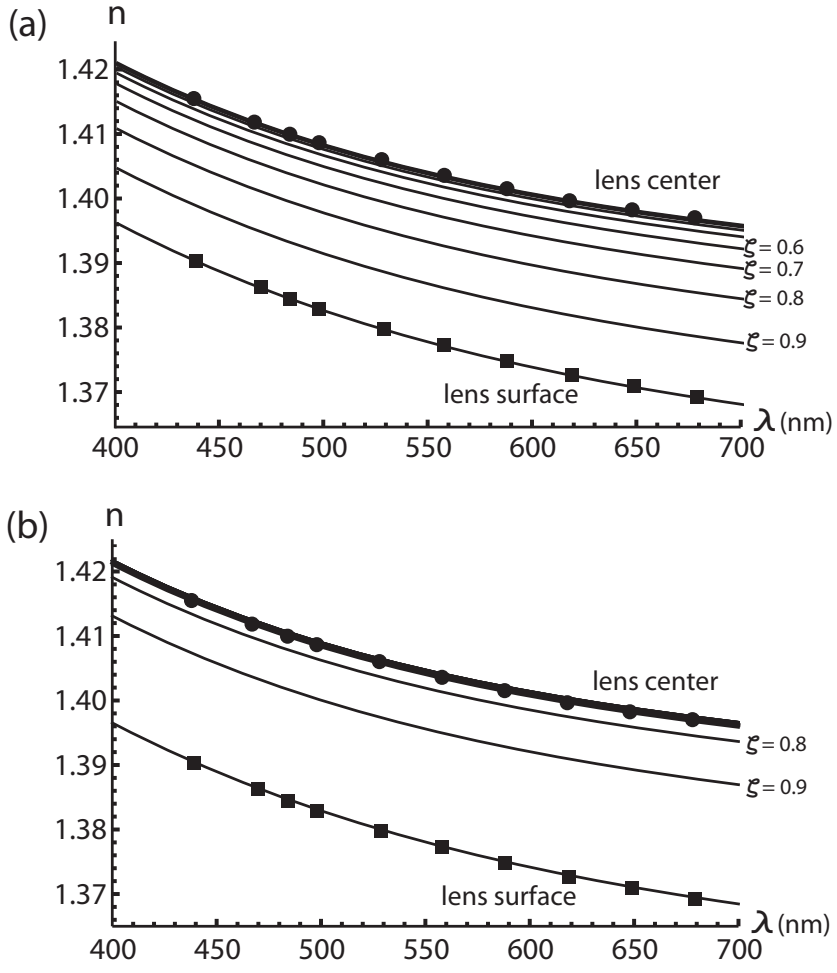

Fig. 4. The fit of the dispersion curves at the center and the surface of the lens to the dispersion data from Sivak and Mandelman [11], and our calculated dispersion curves across the lens employing Eq. (4) for (a) $p = 2.0$ and (b) $p = 5.0$.

#168414 - $15.00 USD Received 10 May 2012; revised 13 Jun 2012; accepted 13 Jun 2012; published 22 Jun 2012

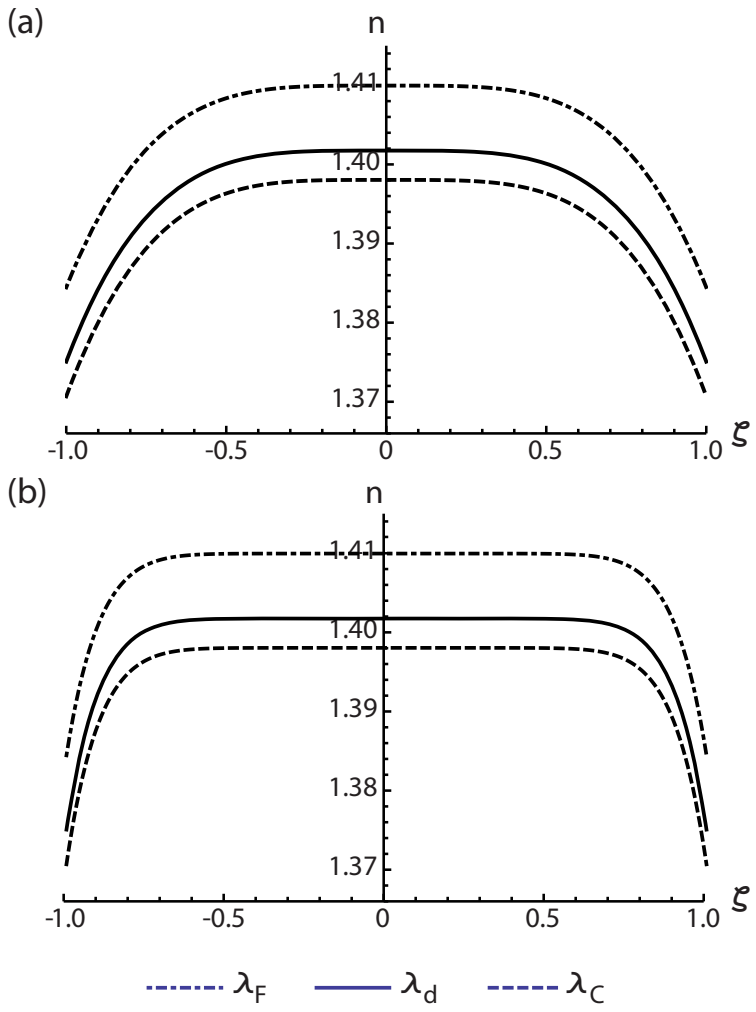

Fig. 5. The refractive index profiles across the lens for $\lambda_F = 486.1$ nm, $\lambda_d = 587.6$ nm, and $\lambda_C = 656.3$ nm using Eq. (4) for (a) $p = 2.0$ and (b) $p = 5.0$ fit to the dispersion data from Sivak and Mandelman [11].

3. Chromatic aberration

3.1. Chromatic coefficients

Using the idea of thin, iso-dispersive shells, we shall describe the chromatic effects occurring within the bulk of the lens. For this we need to revisit the definition of the axial and transverse chromatic aberrations in terms of paraxial optics.

The axial color coefficient for a single refractive surface C_L [14] is given by

$$C_L = n_d y \left(\frac{y}{r} + u\right) \left(\frac{n_d - 1}{n_d V_d} - \frac{n'_d - 1}{n'_d V'_d}\right), \tag{11}$$

where n_d is the refractive index of the medium at the spectral line d ($\lambda_d = 587.6$ nm) before the surface, y and u are the height and the angle of the incident ray at the surface, respectively, r is the surface radius of curvature, and V_d and V'_d are the Abbe numbers of the media respectively before and after the surface. The Abbe number is defined as

$$V_d = \frac{n_d - 1}{n_F - n_c}, \tag{12}$$

#168414 - $15.00 USD Received 10 May 2012; revised 13 Jun 2012; accepted 13 Jun 2012; published 22 Jun 2012

where n_F and n_c are the refractive indices of the medium at the spectral line F ($\lambda_F = 486.1$ nm) and the spectral line C ($\lambda_C = 656.3$ nm), respectively.

By adding the C_L coefficients of all surfaces in an optical system the total axial color coefficient is obtained. Using this coefficient, the axial distance between the image position at F and C wavelengths can be calculated as longitudinal axial chromatic aberration δ_{AX},

$$\delta_{AX} = \frac{1}{n_{di}u_i^2} C_L, \tag{13}$$

where n_{di} is the refractive index at d line in the last medium and u_i is the refracted ray angle at the image plane.

In a similar way, the lateral color coefficient C_T is given by

$$C_T = n_d y \left(\frac{y_c}{r} + u_c\right)\left(\frac{n_d - 1}{n_d V_d} - \frac{n'_d - 1}{n'_d V'_d}\right), \tag{14}$$

where y_c and u_c are the height and the angle of the incident chief (principal) ray at a refractive surface, respectively. The total coefficient C_T can be used in calculating the transverse lateral chromatic aberration δ_{TLC}, which corresponds to the vertical distance between the images at F and C wavelengths:

$$\delta_{TLC} = \frac{1}{n_{di}u_i} C_T. \tag{15}$$

The total axial and lateral color coefficients of a GRIN lens are the key to understanding its chromatic behavior in the eye. Using the paraxial ray tracing as in our derivation of the monochromatic aberrations in the GIGL model [3], the total chromatic coefficients can be obtained for the dispersive GRIN structure. Following the analytical ray tracing through the GIGL model, we shall derive the expressions for the axial and lateral color coefficients. First we define the Abbe number of the iso-dispersive shells Using Eq. (4)

$$V_d(\zeta) = \frac{n(\zeta, \lambda_d) - 1}{n(\zeta, \lambda_F) - n(\zeta, \lambda_C)}, \tag{16}$$

In general ζ corresponds to the normalized distance from the lens center to any point in the lens. The distance ζ along the optical axis is simply z/T_a and z/T_p for the anterior and posterior hemispheres, respectively. For a constant Abbe number V_d Eq. (16) defines the corresponding constant ζ of the iso-dispersive contour.

Equation (16) can be described in terms of axial distance z for paraxial ray tracing. Employing Eqs. (11), (4), and (16) we find the contribution of a thin layer with the thickness of δz within the GRIN structure in the total axial color coefficient of the lens as

$$\delta C_L = n\left(\frac{z}{T}, \lambda_d\right) y(z)\left(\frac{y(z)}{-Rz} + \frac{y'(z)}{T}\right)\left[\frac{\partial n}{\partial z}\left(\frac{z}{T}, \lambda_d\right)\left(n\left(\frac{z}{T}, \lambda_F\right) - n\left(\frac{z}{T}, \lambda_C\right)\right) - \right.$$
$$\left. - n\left(\frac{z}{T}, \lambda_d\right)\left(\frac{\partial n}{\partial z}\left(\frac{z}{T}, \lambda_F\right) - \frac{\partial n}{\partial z}\left(\frac{z}{T}, \lambda_C\right)\right)\right] / n^2\left(\frac{z}{T}, \lambda_d\right) \delta z, \tag{17}$$

where $y(z)$ is the height of the ray inside the GRIN lens and R is the radius of curvature of the surface; the analytical expression for $y(z)$ in the GIGL model is derived in Ref. [3]. By summing up the contributions from all infinitely thin layers in the GRIN structure (where R equals to R_a and R_p in the anterior and posterior hemispheres, respectively) and including the contributions from the external surfaces of the lens we find the total axial color coefficient of

#168414 - $15.00 USD Received 10 May 2012; revised 13 Jun 2012; accepted 13 Jun 2012; published 22 Jun 2012

the lens,

$$\sum C_L = n_{aqu} y_0 \left(\frac{y_0}{R_a} + u_a\right)\left(\frac{n_{aqu}-1}{n_{aqu}V_{aqu}} - \frac{n(-1,\lambda_d)-1}{n(-1,\lambda_d)V_d(-1)}\right) + \\ + \int_{-T_a}^{T_p} \mathrm{d}C_L + n(1,\lambda_d) y(T_p)\left(\frac{y(T_p)}{-R_p} + u(T_p)\right)\left(\frac{n(1,\lambda_d)-1}{n(1,\lambda_d)V_d(1)} - \frac{n_{vit}-1}{n_{vit}V_{vit}}\right), \quad (18)$$

where y_0 and u_a are respectively the height and angle of the marginal ray at the anterior surface, $y(T_p)$ and $u(T_p)$ are respectively the height and the angle of the marginal ray just before the posterior surface, n_{aqu} and V_{aqu} are respectively the refractive index and the Abbe number of the medium before the lens at the d line, and n_{vit} and V_{vit} correspond to the medium after the lens. It is worth noticing that the ray tracing for these calculations should be done at the d line.

Similarly the coefficients for the lateral color of the lens is given by

$$\delta C_T = n\left(\frac{z}{T},\lambda_d\right) y(z)\left(\frac{y_c(z)}{-Rz} + \frac{y_c'(z)}{T}\right)\left[\frac{\partial n}{\partial z}\left(\frac{z}{T},\lambda_d\right)\left(n\left(\frac{z}{T},\lambda_F\right) - n\left(\frac{z}{T},\lambda_C\right)\right) - \right. \\ \left. - n\left(\frac{z}{T},\lambda_d\right)\left(\frac{\partial n}{\partial z}\left(\frac{z}{T},\lambda_F\right) - \frac{\partial n}{\partial z}\left(\frac{z}{T},\lambda_C\right)\right)\right] / n^2\left(\frac{z}{T},\lambda_d\right)\delta z, \quad (19)$$

where $y_c(z)$ is the chief ray height inside the lens. Assuming the aperture stop is located at the anterior surface of the lens we obtain the total lateral color coefficient of the lens

$$\sum C_T = n_{aqu} y_0 u_{ca}\left(\frac{n_{aqu}-1}{n_{aqu}V_{aqu}} - \frac{n(-1,\lambda_d)-1}{n(-1,\lambda_d)V_d(-1)}\right) + \\ + \int_{-T_a}^{T_p} \mathrm{d}C_T + n(1,\lambda_d) y(T_p)\left(\frac{y_c(T_p)}{-R_p} + u_c(T_p)\right)\left(\frac{n(1,\lambda_d)-1}{n(1,\lambda_d)V_d(1)} - \frac{n_{vit}-1}{n_{vit}V_{vit}}\right), \quad (20)$$

where u_{ca} is the angle of the chief ray at the anterior surface, and $y_c(T_p)$ and $u_c(T_p)$ are respectively the height and the angle of the chief ray just before the posterior surface of the lens.

At this stage we have all equations ready for analysis of chromatic effects in the GRIN lens.

3.2. Numerical example

Using Eqs. (18) and (20) we can calculate the chromatic effects arising from a typical GRIN lens. To use these two equations, one needs the dispersion data for the GRIN lens as well as the dispersion data for the medium surrounding the lens. For the media before and after the lens, the aqueous and vitreous, respectively, we have used combined data provided by Atchison and Smith in terms of coefficients for Cauchy equation presented in Table 5 in Ref. [12].

3.2.1. Sivak and Mandelman's experimental data

As an example, Table 1 presents a typical GRIN lens geometry and its surrounding media with dispersive characteristics. Since the eye GRIN lens receives a converging beam we shall take into account its convergence by assuming a typical corneal shape with the anterior and posterior radii of curvature of 7.8 mm and 6.7 mm, respectively, the corneal thickness of 0.5 mm, and the 3.5 mm axial distance to the GRIN lens. This corresponds to the marginal ray angle $u_a = -0.036352$ rad at the pupil such that $y_0 = 1$ mm. The aperture stop (iris) is located just before the anterior surface of the lens, so the height of the chief ray at the anterior surface of the lens is zero. For the object located at infinity and the full field of view of 2 deg the chief ray angle at the anterior surface of the lens is $u_{ca} = 0.015000$ rad.

Table 2 presents the chromatic coefficients of this typical GRIN lens for each part of the lens using the dispersion data from Sivak and Mandelman [11] in Eqs. (9) and (10). Here to describe

#168414 - $15.00 USD Received 10 May 2012; revised 13 Jun 2012; accepted 13 Jun 2012; published 22 Jun 2012

the dispersive GRIN medium in accordance with Eq. (11) we assumed $p = 4.0$, which impacts the magnitude of the coefficients C_L and C_T for the GRIN structure.

Axial color coefficients in Table 2 show an interesting compensation effect in axial chromatic aberration of the lens. The negative C_L arising from the peripheral surfaces is to some extent corrected by the positive C_L originating from the GRIN structure of the lens. To understand the origin of the sign in coefficient C_L we revisit Eq. (11). Assuming $u \ll y/r$ and noting that $0 < y$, it is clear that the radius of curvature r and the variation of the quantity $(n_d - 1)/(n_d V_d)$ play the main role in establishing the sign of the axial color coefficient.

Figure 6 illustrates the variation of the quantity $(n_d - 1)/(n_d V_d)$ inside the lens is positive for the anterior hemisphere and negative for the posterior hemisphere. On the other hand, the radius of curvature r for the iso-indicial contours in the GRIN structure is also positive in the anterior and negative in the posterior hemispheres, thus the overall sign of the axial color coefficient of the GRIN structure is positive in both hemispheres.

In contrast, the quantity $(n_d - 1)/(n_d V_d)$ in the medium before and after the lens (0.004979 and 0.004888 respectively) is less than that of the surface of the lens (0.010015). This leads to the negative axial color coefficients at both anterior and posterior lens surfaces, see Table 2. A similar approach could be used to understand the change of sign in lateral color coefficients of the lens, although for the posterior surface we have an additional contribution to the coefficient from the non-zero height of the chief ray.

Table 1. A typical GRIN lens geometry and the dispersive characteristics of the surrounding media at the d line. (*using Table 5 in Ref. [12].)

Lens geometry (mm)		Surrounding medium*	
T_a	2.10	n_{aqu}	1.3347
T_p	1.40	V_{aqu}	50.37
R_a	11.00	n_{vit}	1.3347
R_p	7.50	V_{vit}	51.30

Table 2. The chromatic coefficients of a typical GRIN lens defined in Table 1 with the dispersion data from Sivak and Mandelman [11] described by Eqs. (9) and (10).

Axial color coefficients	
C_L from the anterior surface	-0.000367
C_L from the GRIN structure	+0.000450
C_L from the posterior surface	-0.000958
$\sum C_L$	-0.000875
Lateral color coefficients	
C_T from the anterior surface	-0.000101
C_T from the GRIN structure	+0.000018
C_T from the posterior surface	+0.000047
$\sum C_T$	-0.000036

To get a feeling about the magnitude of calculated axial color coefficient, we also calculate the axial chromatic aberration δ_{AX} in the whole eye using this typical lens. We assume that the lens in the eye is not tilted and then the total axial color coefficient of the eye is the sum of the axial color coefficients of the cornea and the GRIN lens. We assume that the optical power of an average eye is 60 D and the corneal refractive index and Abbe number are $n_d = 1.3677$ and $V_d = 55.48$ [12], which corresponds to the axial color coefficient of -0.000843 for the cornea.

#168414 - $15.00 USD Received 10 May 2012; revised 13 Jun 2012; accepted 13 Jun 2012; published 22 Jun 2012

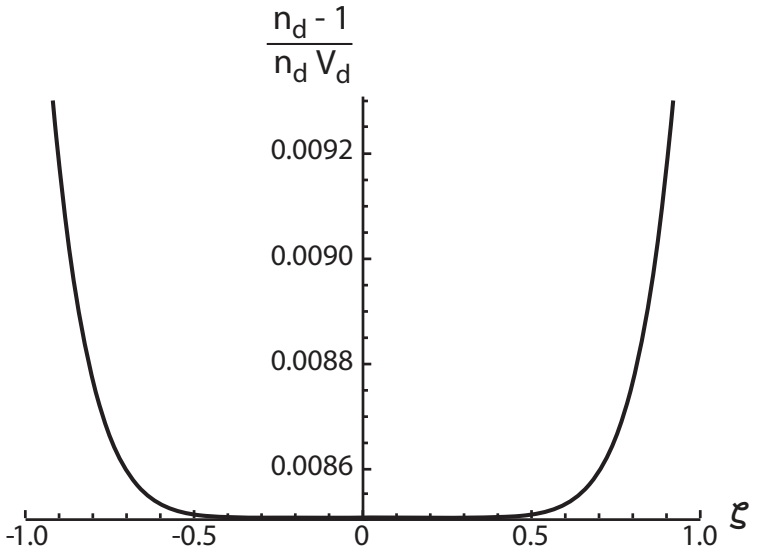

Fig. 6. The quantity $(n_d - 1)/(n_d V_d)$ as a function of ζ (the normalized distance from the lens center) using the dispersion data from Sivak and Mandelman [11] for $p = 4.0$.

The sum of the axial coefficients of the cornea and the lens is -0.001718, and from Eq. (13) we find that the axial chromatic aberration of this eye is 2.09 D. This amount of chromatic aberration is within the expected range of 1.87 ± 0.26 D found in the study by Gilmartin and Hogan [15], which used a similar spectral range of 488 nm and 633 nm.

In addition to the lens dispersion data, Sivak and Mandelman have also provided the dispersion of the capsule of the lens. To study the effect of the lens capsule dispersion on the lens axial color coefficient we have performed a numerical fit to Sivak and Mandelmans measurements using Eq. (3) for the capsule

$$n_{capsule}(\lambda) = 1.37108 + 2617.71\left(\frac{1}{\lambda^2} - \frac{1}{555^2}\right) + 2.5783 \times 10^8 \left(\frac{1}{\lambda^4} - \frac{1}{555^4}\right). \qquad (21)$$

Table 3 provides the lens axial color coefficients using Eq. (21) and (11), which takes into account the chromatic effect of the lens capsule. For the anterior and the posterior layers of the lens capsule we have assumed a typical axial thickness of 0.015 mm and 0.002 mm, respectively [16]. A comparison of Tables 2 and 3 shows that the effect of the capsule is only

Table 3. The chromatic coefficients of a typical GRIN lens defined in Table 1 with the dispersion data from Sivak and Mandelman [11] on the eye lens capsule described by Eq. (21).

Axial color coefficients	
C_L from the anterior surface of the capsule	-0.000075
C_L from the anterior surface of the lens	-0.000292
C_L from the GRIN structure	+0.000450
C_L from the posterior surface of the lens	-0.000749
C_L from the posterior surface of the capsule	-0.000208
$\sum C_L$	-0.000874

0.1 percent of the total axial color coefficient and thus can be ignored. A closer look at Tables 2 and 3 reveals that the lens capsule does not change the magnitude of the chromatic effect

#168414 - $15.00 USD Received 10 May 2012; revised 13 Jun 2012; accepted 13 Jun 2012; published 22 Jun 2012

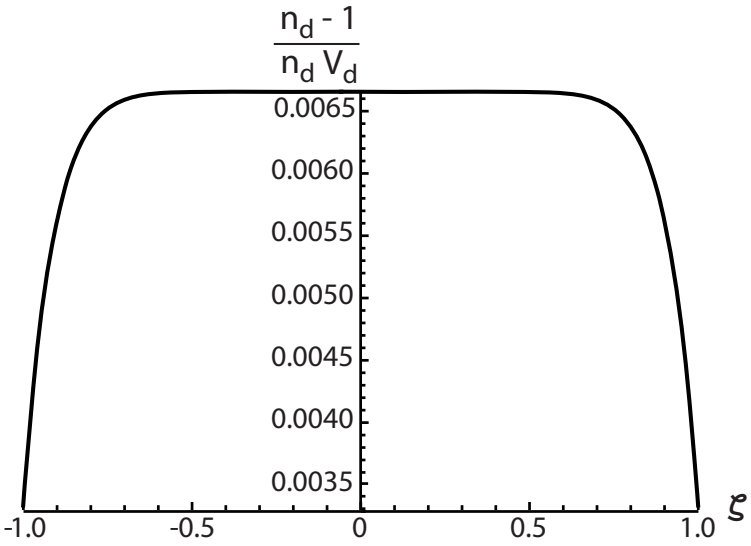

Fig. 7. The quantity $(n_d - 1)/(n_d V_d)$ as a function of ζ (the normalized distance from the lens center) using the dispersion data from Palmer and Sivak [10] for $p = 5.5$.

at the anterior and posterior surfaces of the lens. This is due to a very small thickness of the capsule, which means the radii of curvature of the capsule is very close to those of the lens, leading to a cancellation effect of the capsule contribution to the axial color coefficients.

3.2.2. Palmer and Sivak's experimental data

Employing the same lens geometry and the same dispersive characteristics of the surrounding media, we shall calculate the axial color coefficients of the lens using the dispersion data from the study by Palmer and Sivak of a 70 year old eye [10]. In this study the age of the eye is well defined, so we consider the exponent $p = 5.5$ based on the equation suggested by Navarro *et al.* [8] for connecting the exponent p to the age of the eye. Table 4 presents the color coefficients of the lens and Fig. 7 depicts the quantity $(n_d - 1)/(n_d V_d)$ as a function of the normalized distance ζ from the lens center.

Table 4. The chromatic coefficients of a typical GRIN lens defined in Table 1 with the dispersion data from Palmer and Sivak [10] described by Eqs. (7) and (8).

Axial color coefficients	
C_L from the anterior surface	+0.000120
C_L from the GRIN structure	-0.000948
C_L from the posterior surface	+0.000290
$\sum C_L$	-0.000537
Lateral color coefficients	
C_T from the anterior surface	+0.000033
C_T from the GRIN structure	-0.000038
C_T from the posterior surface	-0.000014
$\sum C_T$	-0.000019

In this example we can also see the compensation of chromatic aberrations in the lens, however in comparison to Table 2 the compensation happens in a different way. Table 4 indicates

#168414 - $15.00 USD Received 10 May 2012; revised 13 Jun 2012; accepted 13 Jun 2012; published 22 Jun 2012

that the GRIN structure of the lens produces a negative axial color coefficient, while the axial color coefficients of the external surfaces are positive. This is due to the different rate of growth of the quantity $(n_d-1)/(n_dV_d)$ presented in Fig. 7, and also due to the different amount of the quantity $(n_d-1)/(n_dV_d)$ at the lens surface, 0.003328, which is less than the surrounding media. As a result, the total axial color coefficient of the lens is still negative (-0.000537) in comparison with Table 2, but its absolute value is reduced by 20%. Using the same characteristics for the cornea, as in Section 3.2.1, the chromatic aberration of the whole eye becomes 1.68 D. This amount of chromatic aberration is within the expected range of 1.87 ± 0.26 D found in the study by Gilmartin and Hogan [15] using a similar spectral range.

3.2.3. Theoretical equations

In addition to the experimental data used in our two examples, it is worth revisiting the lens dispersion equations suggested by Atchison and Smith (Table 5 in Ref. [12]), which is based on the combined theoretical data from Le Grand [17] and Navarro *et al.* [18]. One can notice that the two equations describing the center and the surface dispersion can be reduced to the simple expression $n_{center}(\lambda) \simeq n_{surface}(\lambda) \times 1.014430$. For such a simple connection between the center and the surface dispersion curves, the quantity $(n_d-1)/(n_dV_d)$ becomes independent of ζ terms and remains constant (0.006127) inside the GRIN lens. This becomes clear when we rewrite the quantity $(n_d-1)/(n_dV_d)$ as $(n_F-n_c)/n_d$. The significance of the constancy of the quantity $(n_d-1)/(n_dV_d)$ is that the GRIN structure is free from both chromatic effects (axial and lateral color) and only the external surfaces of the lens contribute to the chromatic aberrations. Table 5 shows this fact numerically under the same conditions considered in Table 1.

We would like to emphasize that for a non-dispersive GRIN structure as well as for a homogeneous refractive index lens (featuring in Le Grand [17] and Navarro *et al.* [18] models) one has only to worry about the dispersion description of the external surfaces of the lens. However the experimental data [10, 11] suggest that the chromatic contribution of the GRIN structure is comparable to that of the external surfaces, and furthermore plays an important role in the chromatic aberration compensation of the whole eye.

Table 5. The chromatic coefficients of a typical GRIN lens defined by Table 1 using the dispersion data from Atchison and Smith (Table 5 in Ref. [12]).

Axial color coefficients	
C_L from the anterior surface	-0.000084
C_L from the GRIN structure	+0.000000
C_L from the posterior surface	-0.000232
$\sum C_L$	-0.000315
Lateral color coefficients	
C_T from the anterior surface	-0.000023
C_T from the GRIN structure	+0.000000
C_T from the posterior surface	+0.000011
$\sum C_T$	-0.000012

It is worth mentioning that for achieving an achromatic lens (*i.e.* $\sum C_L = 0$), the axial color of the external surfaces is to be compensated by that from the GRIN structure, so the latter should not be zero. As an example of such aberration balancing, the lens in Section 3.2 can be made achromatic simply by adjusting one of the center dispersion coefficients, $n_{c\lambda 2}$, in Eq. (9) from 7256.06 to 5098.80. This corresponds to the change in the Abbe number of the lens center from 33.71 to 51.51, using Eq. (4). The example illustrates that the proposed dispersion model can

#168414 - $15.00 USD Received 10 May 2012; revised 13 Jun 2012; accepted 13 Jun 2012; published 22 Jun 2012

also help in developing bio-inspired lens designs, where the achromatic correction in individual components is needed.

4. Equivalent Abbe number approximation

It is a common practice, in the reduced eye models, to replace the GRIN lens by a simple lens providing spatially constant refractive index and Abbe number. Typically the characteristics of the eye lens in the reduced eye models are defined based on the optical power and axial chromatic aberration of the whole eye. In this section a different approach is proposed to calculate the equivalent Abbe number of the lens just using the experimental dispersion curves of the surface layer (cortex) and the center (core) of the GRIN lens. This approach may help in improving the reconstruction methods of a subject-specific GRIN lens.

The GIGL model provides a convenient equation for the optical power of the lens derived from a thin lens approximation as

$$F_{thin} = \frac{n_s - n_{aqu}}{R_a} + \frac{2p}{2p-1}(n_c - n_s)\left(\frac{1}{R_a} + \frac{1}{R_p}\right) + \frac{n_{vit} - n_s}{-R_p}. \tag{22}$$

For the crystalline lens Eq. (22) gives less than 1.4% error compared with the exact power calculations, and then can be a useful tool in the ocular calculations. The equivalent optical power of the lens defined as

$$F_{eqv} = \frac{n_{eqv} - n_{aqu}}{R_a} + \frac{n_{vit} - n_{eqv}}{-R_p}, \tag{23}$$

where the equivalent refractive index n_{eqv} provides the equivalent optical power for the lens. Equating the right hand sides of Eqs. (22) and (23) and solving for n_{eqv} result

$$n_{eqv} = \frac{2\,p\,n_c - n_s}{2\,p-1}. \tag{24}$$

The definition of n_{eqv} by Eq. (24) is not limited to the main wavelength and can be expanded to the equivalent powers of other wavelengths as

$$n_{eqv}(\lambda) = \frac{2\,p(\lambda)\,n_{center}(\lambda) - n_{surface}(\lambda)}{2\,p(\lambda)-1}. \tag{25}$$

Substituting Eq. (24) in Eq. (12) leads to the equivalent Abbe number of the equivalent lens. If the change in p with wavelength λ is negligible the equivalent Abbe number can be rewritten as

$$V_{eqv}(\lambda) = \frac{V_{dc}\,V_{ds}\,[n_s - 1 - 2\,p\,(n_c - 1)]}{V_{dc}\,(n_s - 1) - 2\,p\,V_{ds}\,(n_c - 1)}, \tag{26}$$

where V_{dc} and V_{ds} are the Abbe numbers of the center and the surface of the GRIN lens, respectively. As an example, Table 1 presents the calculated lens equivalent refractive index n_{eqv} and the equivalent Abbe number V_{eqv} using the dispersion data from Sivak and Mandelman [11], and Palmer and Sivak [10] for $p = 3.0$ (representing a 34-year old eye according to the study by Navarro *et al.* [8]).

Employing the equivalent refractive indices and Abbe numbers listed in Table 6, one can calculate the axial and lateral color coefficients of the equivalent lens. These coefficients are approximate, while the exact color coefficients derived in Eqs. (18) and (20). The comparison between the axial and lateral color of a typical GRIN lens and its equivalent refractive index lens is presented in Table 7. Here, the angles and the height of the incident rays, and the geometry

#168414 - $15.00 USD Received 10 May 2012; revised 13 Jun 2012; accepted 13 Jun 2012; published 22 Jun 2012

Table 6. The calculated quantities n_{eqv} and V_{eqv} using the dispersion data from Sivak and Mandelman [11], and Palmer and Sivak [10] for a typical $p = 3.0$.

Data set	n_c	n_s	n_{eqv}	V_{dc}	V_{ds}	V_{eqv}
Sivak and Mandelman	1.4018	1.3751	1.4071	33.71	27.23	35.25
Palmer and Sivak	1.3968	1.3750	1.4011	42.73	81.95	39.22

Table 7. A comparison between the exact and equivalent color coefficients calculated respectively for a typical GRIN lens and its equivalent refractive index lens.

Data set	Equivalent $\sum C_L$	Exact $\sum C_L$	Equivalent $\sum C_T$	Exact $\sum C_T$
Sivak and Mandelman	-0.000856	-0.000852	-0.000034	-0.000035
Palmer and Sivak	-0.000618	-0.000626	-0.000024	-0.000022

of the lens and its surrounding media are the same as in the previous numerical examples (See Section 3.2.1), except for the exponent p, here $p = 3.0$.

Table 7 demonstrate a good agreement between the exact and equivalent color coefficients, which indicates practical advantages of this approach in finding the exact equivalent optical characteristics. However, replacing a complicated GRIN structure with a homogeneous material will not transfer all optical characteristics of the lens simultaneously. Here, the equivalent refractive index calculation aims at preserving the optical power of the lens, yet other optical characteristics of the lens need their own equivalent refractive index. As an example, we consider the optical path length (OPL) in the GRIN lens. The axial OPL in GIGL [3] is derived as

$$OPL = (T_a + T_p)\,\frac{2n_c p + n_s}{2p+1}, \tag{27}$$

which defines the quantity $(2n_c p + n_s)/(2p+1)$ as the equivalent refractive index in the OPL calculation of the lens. This OPL equivalent refractive index known as the average refractive index [19] is different from the one calculated in Eq. (24).

5. Axial Chromatic aberration and aging

There are two independent studies, which found no significant changes in the magnitude of chromatic aberration with age [20, 21], but some earlier studies claim that the magnitude of chromatic aberration decreases with age [22, 23]. Considering the growth of the GRIN lens, it is well known that for an unaccommodated lens, the external surfaces become more curved with aging [24]. The lens considered in Section 3.2.2 shows positive axial color coefficients at its surfaces (Table 4). Aging lens increases the optical power of its surfaces, thus this lens surfaces will show larger positive axial color coefficients, see Eq. (11). In addition to this, the chromatic effect arising from the GRIN structure should be taken into account. To examine the role of the GRIN structure in the age-related chromatic effect individually, we keep the geometry of the lens in Section 3.2.2 unchanged, only adjust the age-related exponent p to three different age groups. Following the study by Navarro *et al.* [8] we selected three age groups (20, 40, and 60 year old) with corresponding value for p and calculated the resultant axial color coefficients for each group in Table 8.

Table 8 indicates that the magnitude of the axial color coefficient originated from the GRIN structure of the lens decreases due to an increase in the exponent p. Looking at the sign of the coefficients of the lens surfaces, it is evident that the total axial color coefficient of the lens goes toward zero or even positive amounts. As mentioned in Section 3.2.1, a typical cornea

#168414 - $15.00 USD Received 10 May 2012; revised 13 Jun 2012; accepted 13 Jun 2012; published 22 Jun 2012

Table 8. The axial color coefficients from the GRIN structure for three age groups (20, 40, and 60 year old) using the dispersion data provided by Palmer and Sivak [10].

Age (year)	p	C_L from the GRIN structure
20	2.87	-0.001046
40	3.13	-0.001028
60	4.28	-0.000977

shows a negative axial color coefficient. Due to aging, the surfaces of the cornea get slightly more curved [25], which increases the magnitude of this negative corneal axial color coefficient. Considering these two effects for the GRIN lens and the cornea, one could argue that the eye, as a whole, might show a constant or a better chromatic performance with aging.

It is worth mentioning that employing the Sivak and Mandelman's data in the same approach provides an increase in the total axial color coefficient, which does not support the argument above. Since the dispersion data from Sivak and Mandelman is averaged over 6 to 9 subjects with different ages, some valuable information of each individual lens might be missing. This highlights the need of more chromatic measurements on the GRIN lens and its surrounding media for a more confident conclusion.

6. Discussion and conclusion

In this study the potential of the existing GIGL monochromatic model [3] has been realized and demonstrated by introducing a flexible chromatic GRIN lens model. The model is examined with different data fittings to gain better understanding of the GRIN lens chromatic aberration behavior of the lens. The advantages of the provided equations are not limited to this data fitting only, since the model can also be used to help explaining other chromatic characteristics of the eye for example spherochromatism. The latter can be calculated using the spherical aberration coefficients for different color wavelength.

We would like to emphasize that the provided model should be regarded as a tool, which can be employed in experimental data fitting and further analysis for better understanding of the chromatic nature of the eye. The scope of the chromatic model is not limited to the human eye and can be applied to animal GRIN lenses, where unusual chromatic behavior might happen (*e.g.* [26, 27]). Table 9 provides the axial color coefficients of a semi-spherical octopus eye lens calculated based on the measurements from Jagger and Sands [27].

Table 9. The chromatic coefficients of a typical octopus GRIN lens using the dispersion data from Jagger and Sands [27].

Axial color coefficients	
C_L from the anterior surface	-0.000779
C_L from the GRIN structure	-0.003499
C_L from the posterior surface	-0.000629
$\sum C_L$	-0.004909

The proposed dispersive GIGL model completes the description of the monochromatic GIGL model. The concept of iso-dispersive contours introduced in this paper is a unique feature of the dispersive GIGL model. The optically-friendly geometry of the GIGL model featuring iso-dispersive contours (constant Abbe number V_d) supports the calculations for the contribution of the individual layers to the total chromatic effects of the lens. Thus the model gives a new insight in the derivation of the equivalent Abbe number based on experimental dispersion curves

#168414 - $15.00 USD Received 10 May 2012; revised 13 Jun 2012; accepted 13 Jun 2012; published 22 Jun 2012

for the center and the surface of the lens. The proposed model offers easy analysis of equivalent refractive index and OPL equivalent index. One could use the model to investigate chromatic aberration evolution in the aging human eye, in particular the effect of the power constant p on the color coefficients. The model also predicts the amount of induced defocus (change in optical power with wavelength) when using different wavelengths, *e.g.* adaptive optic system with wavefront sensor operating at one wavelength and the retinal imaging at another wavelength, although retinal absorption effects still have to be included in this case.

Acknowledgments

The authors would like to thank Prof. Chris Dainty for his valuable comments. This research was supported by Science Foundation Ireland under grant 07/IN.1/1906.

#168414 - $15.00 USD Received 10 May 2012; revised 13 Jun 2012; accepted 13 Jun 2012; published 22 Jun 2012